Detection of biomass tar
using an SOFC

by

Martin Hauth

A dissertation submitted to the graduate faculty

in partial fulfillment of the requirements for the degree of

DOCTOR OF MECHANICAL ENGINEERING

Major: Energy and Environmental Engineering

Program of Study Committee

Univ.-Prof. Dr.-Ing. Jürgen Karl, Major Professor

Assoc. Prof. Dipl-Ing. Dr. Viktor Hacker

Insitute of Thermal Engineering

Graz University of Technology

Graz, Austria, August 2011

Affidavit

I declare that I have written this thesis independently and on my own. I have clearly marked any language or ideas borrowed from other sources as not my own and documented their sources. This thesis has not been submitted to any other examination authoriy in its current or an altered form, and it has not been published.

Graz, August 2011

Martin Hauth

Vorwort / Preface

Diese Dissertation entstand während meiner Tätigkeit als wissenschaftlicher Universitätsassistent am Institut für Wärmetechnik der Technischen Universität Graz im Zeitraum von Mai 2008 bis August 2011. Die Motivation zu dieser Arbeit lag rückblickend gesehen in der einmaligen Gelegenheit, sich mit seinen im Studium erlernten Kenntnissen auszutoben und diese weitgehend frei und selbständig zur Lösung technischer Problemstellungen einzusetzen.

Für die Bereitstellung dieser Spielwiese gilt mein ganz persönlicher Dank meinem Doktorvater Univ.-Prof. Dr.-Ing. Jürgen Karl, der schlussendlich die Grundidee zu dieser Arbeit hatte. Nicht zuletzt sein Optimismus und sein Talent andere für eine Idee zu begeistern, haben so manches Motivationstief erst gar nicht entstehen lassen und haben dadurch wesentlich zum Gelingen dieser Arbeit beigetragen.

Für das Interesse an meiner Arbeit und die Übernahme der Zweitbegutachtung danke ich Assoc. Prof. Dipl.-Ing. Dr.techn. Viktor Hacker.

Besonders freue ich mich, dass diese Arbeit immer von einem kollegialen und hilfsbereiten Arbeitsklima begleitet war. Dafür bedanke ich mich zu aller erst bei meinem Arbeitskollegen Lorenz Griendl mit dem ich die letzten Jahre das Vergnügen hatte das Büro zu teilen (Selamat tengah hari!). Thomas Kienberger sei an dieser Stelle gedankt für die Geduld und Nachsicht bei Auskünften über elektrotechnische Belange. Meinen restlichen ArbeitsgruppenkollegInnen - Andrea Janics, Bernhard Gatternig, Christoph Baumhakl und Davide Roveda - danke ich für den ständigen Erfahrungsaustausch und unzählige kleine Tipps, die mir die tägliche Arbeit oft sehr erleichtert haben.

Für die Unterstützung und gute Zusammenarbeit beim Aufbau, sowie bei der Inbetriebnahme des Prüfstands und bei der Durchführung zahlreicher Messkampagnen möchte ich meinen Diplomanden Stefan Wahl, Werner Lerch und Karlheinz König einen großen Dank aussprechen. Die Entstehung eines funktionierenden Prüfstands, der für diese Arbeit von essentieller Bedeutung war, wäre ohne den konstruktiven und praktischen Beiträgen meiner Kollegen aus der Werkstatt - Herbert Hartner, Gernot Hollegger, Markus Sackl und Heinz Strauß - nicht möglich gewesen. In diesem Zusammenhang möchte ich auch den Beitrag der Bachelor-Studenten Christian Zuber, Harald Hiebler und Johann Hopfgartner bzw. der Studienassistenten David Hannl, David Landerl und Artur Grengg, die mir mit ihrem stets großem Engagement eine große Hilfe waren, besonders hervorheben.

Für unzählige Kniffe beim Umgang mit LaTex, ohne die diese Arbeit in der Form

nie zu Papier gebracht worden wäre, und für die daraus resultierenden interessanten Gespräche über die Typographie im Allgemeinen bedanke ich mich bei Stefan Gruber.

Die Energietechnik bietet ein breites, umfangreiches und vor allem aufregendes Betätigungsfeld. Der steigende Energiehunger unserer Gesellschaft dürfte wohl dazu beitragen, dass sich diese Situation nicht so schnell ändert. Deshalb bin ich glücklich eine Ausbildung genossen zu haben, die es mir ermöglicht, in dieser spannenden Entwicklung, in der sich unsere Gesellschaft befindet, mitzuwirken. Dieses Glück verdanke ich in erster Linie meinen Eltern.

Das Verfassen dieser Arbeit hat so manches Wochenende verschlungen. Für das Verständnis, mit dem du dem Ganzen geduldig begegnet bist und für die immerwährenden, liebevollen Aufmunterungen zwischendurch danke ich dir, Stephanie.

Kurzfassung

Die Detektion von höheren Kohlenwasserstoffen ist insbesondere in Anwendungen in denen Reformat- bzw. Synthesegase zum Einsatz kommen ein wichtiges Kriterium. Bereits geringe Konzentrationen von höheren Kohlenwasserstoffen können zu erheblichen Problemen führen. Kondensation oder die Bildung von Hydraten in Verbindung mit Wasser können besonders bei niedrigen Temperaturen zur Fehlfunktion von Ventilen oder Verstopfen von Gasleitungen führen. Darüber hinaus werden einige höhere Kohlenwasserstoffe als gesundheitsschädlich eingestuft und erfordern daher eine entsprechende Gasreinigung des Synthesegases. Für diese Anwendungsfälle sind zumeist Grenzwerte einzuhalten, die somit die Relevanz einer Überwachung von kritischen Kohlenwasserstoffen aufzeigen.

Synthesegas aus der Biomassevergasung kann unterschiedliche höhere Kohlenwasserstoffe, die unter dem generischen Sammelbegriff "Teer" zusammengefasst werden, enthalten. Abhängig von der jeweiligen Vergasertechnologie kann das Synthesegas Teerfrachten bis zu $100\,\text{g/Nm}^3$ aufweisen. Für die Nutzung des Synthesegases in nachfolgenden Prozessen, wie beispielsweise in einem Gasmotor, müssen diese Teerfrachten vorab reduziert werden. Im Falle einer Kaltgasreinigung werden die Teerkomponenten ausgewaschen. Dies führt folglich auch zu einer unerwünschten Verringerung des Heizwertes des Synthesegases.

Die Teerkonzentration hängt nicht nur von der Vergasertechnologie, sondern auch von den Prozessparametern ab. Daher gilt es, die optimalen Betriebsbedingungen zu finden, unter denen die Teerentstehung minimal ist. Derzeit ist kein passender Teersensor am Markt erhältlich, der eine kontinuierliche Messung der Teerkonzentration am Ausgang des Vergasers ermöglicht, um diese Optimierung durchzuführen. Typische Nachteile derzeitiger Messsysteme, wie z.B. Flammenionisationsdetektor, Gaschromatographie, Teer Protokoll oder Solid Phase Adsorption sind eine hohe Komplexität der Gasanalyse oder das Fehlen einer Möglichkeit zur Unterscheidung zwischen unterschiedlichen Teerkomponenten.

Diese Arbeit untersucht eine neuartige Methode der Teermessung mittels Festoxid Brennstoffzelle (Solid Oxide Fuel Cell). SOFCs sind im Stande methanhaltiges Synthesegas umzusetzen. Des Weiteren wurde die Umsetzung von unterschiedlichen Kohlenwasserstoffen in der Vergangenheit sehr stark untersucht. Im Besonderen wurde der Einfluss von Kohlenwasserstoffen die bei der Vorreformierung von Brennstoffen wie Erdgas, Diesel, Methanol, oder Kerosin entstehen, getestet. In dieser Arbeit wird speziell auf das Umsetzungsverhalten der Biomasseteerkomponenten Naphthalin, To-

luol und Xylol in einer SOFC eingegangen. Die Umsetzung trägt beträchtlich zum Zellpotential bei. Aus diesem Grunde gilt die Untersuchung in erster Linie der Korrelation zwischen der Teerkonzentration und dem Beitrag zum Zellpotential. In diesem Zusammenhang ist die gegenseitige Beeinflussung zwischen den Kohlenwasserstoffen hinsichtlich der Umsetzung ein wichtiger Aspekt für die Untersuchung des Zellpotentials.

Der Sensor ermöglicht eine kontinuierliche in-situ Messung. Die hohe Betriebstemperatur des Sensors wirkt sich dahingehend vorteilhaft aus, dass keine Kühlung des zu messenden Gases erforderlich ist.

Abschließend wird ein "2-Zellen-Reformer" Konzept präsentiert, das sowohl die Detektion der Teerkonzentration als auch eine Differenzierung der Teerkomponenten ermöglicht.

Abstract

The detection of hydrocarbons is an important issue in many applications where reformate gas or synthesis gas is utilised. Even low concentrations of hydrocarbons may cause difficulties due to different reasons. Blocking of gas pipes because of condensation of higher hydrocarbons or formation of hydrates in combination with water at very low temperatures are just two of them. Moreover, some of the hydrocarbons are harmful to health and require gas cleaning for safety reasons. In all cases certain concentration limits have to be met which necessitates hydrocarbon monitoring.

Synthesis gas from biomass gasification may contain a variety of higher hydrocarbons, so called tar. Depending on the gasifier technology very high concentrations up to $100\,\mathrm{g/Nm^3}$ are transported in the wood gas. For the utilisation of synthesis gas in downstream applications such as a gas motor tar has to be removed to a certain extend first. In the case of wet gas cleaning this eventually means a reduction of the heating value due to the loss of hydrocarbons.

The level of tar depends not only on the gasifier technology but also on the process parameters. Therefore, it is obvious that an ideal operating point exists where the gasifier produces least amounts of tar. So far there is no suitable tar sensor on the market that allows the continuous monitoring of the tar concentration in the gasifier outlet gas stream. Typical drawbacks of the current measuring systems such as flame ionisation detector, gas chromatography, tar protocol or solid phase adsorption are either a discontinuous gas measurement, a high complexity of the gas analysis or the inability to differentiate between different hydrocarbon species.

This work investigates a new approach of measuring tar based on a solid oxide fuel cell. SOFCs are capable of converting synthesis gas containing methane. The conversion of several hydrocarbons has been thoroughly investigated in the past. In particular the influence on the SOFC of hydrocarbons coming from the pre-reforming step of fuels such as natural gas, diesel, methanol or kerosene is multiply tested. This work concentrates on the conversion behaviour of biomass tar, in particular toluene, xylene and naphthalene, on a SOFC anode. The conversion significantly contributes to the cell potential. Therefore a correlation between the contribution to the cell potential and the tar concentration is developed. In this context the mutual interference of the conversion of the different tested tar species is an important aspect to evaluate the cell potential.

The sensor enables continuous measurement including in-situ analysis. The operating

temperature of the sensor is very high, therefore the wood gas coming from the gasifier does not need to be cooled before entering the measuring cell.

Finally a "2-cell-reformer" concept is presented that allows a determination of the tar concentration as well as a distinction between certain tar species.

Contents

List of Figures

List of Tables

Abbreviations

General Abbreviations

AFC	Alkaline fuel cell
COD	Chemical oxygen demand
CPOX	Catalytic partial oxidation
DIR	Direct internal reforming
FG	Forming gas
FID	Flame ionisation detector
GA	Gas analyser
GC	Gaschromatograph
GHSV	Gas hourly space velocity
GIL	Gilibrator®, volume flow meter
GIR	Gradual internal reforming
HC	Hydrocarbon
HT-PEMFC	High temperature polymer electrolyte fuel cell
IR	Infra red
MCFC	Molten carbonate fuel cell
MFC	Mass flow controller
MS	Mass spectrometer
NDIR	Non dispersive infra red
OCV	Open circuit voltage
OSR	Oxidative steam reforming

PAFC	Phosphoric acid fuel cell
PSA	Perfluorocarbon-sulfonic acid
PSEPVE	Perfluoro-sulfonylfluoride ethyl-propyl-vinyl ether
SNG	Substitute natural gas
SOFC	Solid oxide fuel cell
SPA	Solid phase adsorption
SR	Steam reforming
TCD	Thermal conductivity detector
TOC	Total organic carbon
TOS	Time on stream
TPB	Triple phase boundary
TPO	Temperature programmed oxidation
TRT	Transient response time
UV	Ultra violet

SOFC Materials

CGO	Gadolinium doped ceria
GCO	Gadolinium doped ceria
GDC	Gadolinium doped ceria
LSCF	Lanthanum strontium cobalt ferrite
LSM	Lanthanum strontium manganate
YSZ	Yttria stabilised zirconia

Elements

Al	Aluminum
Au	Gold

Ce	Cerium
Co	Cobalt
Cu	Copper
Fe	Iron
Gd	Gadolinium
La	Lanthanum
Mn	Manganese
Ni	Nickel
Pt	Platinum
Sr	Strontium
Y	Yttrium
Zr	Zirconium

Variables

a_i	Activity	$[-]$
$a_i,\ b_i,\ c_i,\ d_i$	Fit curve parameters	$[-]$
$A,\ B,\ C$	Antoine parameter	$[-]$
$A^*,\ B^*,\ C^*$	Adsorbed molecule	$[-]$
$A_g,\ B_g,\ C_g$	Gaseous molecule	$[-]$
c_A	Concentration of adsorbed molecule	$[\,\text{vol.\%, ppm}\,]$
C_i	Number of carbon atoms	$[-]$
CR	Conversion rate	$[\,\%\,]$
CR_{CH_4}	Conversion rate of methane	$[\,\%\,]$
dp	Particle diameter	$[\,\text{mm}\,]$
f_i	FID conversion factor	$[-]$
$E_{i,equivalent}$	Equivalent concentration	$[\,\text{ppm}\,]$

F	Farraday constant	$\left[\,\mathrm{C}/\mathrm{mol}\,\right]$
i	Current density	$\left[\,\mathrm{mA}/\mathrm{cm^2}\,\right]$
I	Current	$\left[\,\mathrm{A}\,\right]$
k	Reaction coefficient	$\left[\,\mathrm{mol^{1-n}}/\mathrm{m^{3-3n}\cdot s}\,\right]$
$k_{C_xH_y}$	Slope of equilibrium voltage increase	$\left[\,\mathrm{g}/(\mathrm{Nm^3\cdot mV})\,\right]$
$k_{C_xH_yO_z}$	Slope of equilibrium voltage increase	$\left[\,\mathrm{g}/(\mathrm{Nm^3\cdot mV})\,\right]$
k_{tar}	Slope of equilibrium voltage increase	$\left[\,(\mathrm{Nm^3\cdot mV})/\mathrm{g}\,\right]$
K_i	Equilibrium constant	$\left[\,-\,\right]$
p_0	Total pressure	$\left[\,\mathrm{bar}\,\right]$
p_i	Partial pressure	$\left[\,\mathrm{bar}\,\right]$
Q	Reaction quotient	$\left[\,-\,\right]$
r_{eff}	Reaction rate	$\left[\,\mathrm{mol}/\mathrm{m^2\cdot s},\ \mathrm{mol}/\mathrm{g\cdot s}\,\right]$
v_i	Fit curve parameter	$\left[\,-\,\right]$
V	Voltage	$\left[\,\mathrm{mV}\,\right]$
V_N	Nernst voltage	$\left[\,\mathrm{mV}\,\right]$
V_{OCV}	Open circuit voltage	$\left[\,\mathrm{mV}\,\right]$
$\dot{V}_{cath}$	Volume flow through SOFC cathode	$\left[\,\mathrm{Nml}/\mathrm{min}\,\right]$
$\dot{V}_{cell}$	Volume flow through SOFC anode	$\left[\,\mathrm{Nml}/\mathrm{min}\,\right]$
$\dot{V}_{fuel}$	Volume flow of gas mixing unit	$\left[\,\mathrm{Nml}/\mathrm{min}\,\right]$
$\dot{V}_{GA}$	Volume flow of gas analyser	$\left[\,\mathrm{Nml}/\mathrm{min}\,\right]$
$\dot{V}_{MA}$	Volume flow of mixing air	$\left[\,\mathrm{Nml}/\mathrm{min}\,\right]$
n	Order of reaction	$\left[\,-\,\right]$
$\dot{n}_{el}$	Molar flow of electrons	$\left[\,\mathrm{mol}/\mathrm{s}\,\right]$
$\dot{n}_{fuel}$	Molar flow of fuel	$\left[\,\mathrm{mol}/\mathrm{s}\,\right]$
n^{el}	Electron ratio	$\left[\,-\,\right]$
R	Ideal gas constant	$\left[\,\mathrm{J}/\mathrm{mol\cdot K}\,\right]$

t	Temperature	$[\,°\mathrm{C}\,]$
T	Temperature	$[\,\mathrm{K}\,]$
$u_{V_{Nernst}}$	Uncertainty of Nernst voltage	$[\,\mathrm{mV}\,]$
w_0	Fit curve parameter	$[\,-\,]$
w_i	Tar load	$[\,\mathrm{g/Nm^3}\,]$
$X,\,Y$	Empiric constant	$[\,\mathrm{ppm}\,]$
Z	Empiric constant	$[\,\mathrm{vol.\%}\,]$
$\Delta_R H$	Reaction enthalpy	$[\,\mathrm{J/mol}\,]$
$\Delta_R S$	Reaction entropy	$[\,\mathrm{J/mol \cdot K}\,]$
$\Delta_R G$	Reaction Gibbs enthalpy	$[\,\mathrm{J/mol}\,]$
ΔOCV	Increase of open circuit voltage	$[\,\mathrm{mV}\,]$
ΔV_N	Increase of Nernst voltage	$[\,\mathrm{mV}\,]$
λ	Air/fuel ratio	$[\,-\,]$
ν_i	Stoichiometric coefficient	$[\,-\,]$
μ_i	Chemical potential	$[\,\mathrm{J/mol}\,]$
σ	Steam value	$[\,-\,]$
$\tau_{transient}$	Transient response time	$[\,\mathrm{sec,min}\,]$
Θ_i	Surface coverage	$[\,-\,]$
x_i	Volumetric concentration	$[\,\mathrm{vol.\%,\ ppm}\,]$
ζ	Extend of reaction	$[\,-\,]$

Voltages used for tar measuring principle

$V_{equ,C_xH_y,0}$	Nernst voltage considering tar species	$[\,\mathrm{mV}\,]$
V_{equ,C_xH_y}	Nernst voltage considering tar species and ΔV_{Offset}	$[\,\mathrm{mV}\,]$
$V_{equ,0}$	Nernst voltage without tar species	$[\,\mathrm{mV}\,]$

V_{Base}	Base voltage . . . . [mV]
$V_{cell:1}$	Measured OCV of cell:1 . . . . [mV]
$V_{cell:2}$	Measured OCV of cell:2 . . . . [mV]
$V_{cell:1,naph}$	Measured OCV of cell:1 for the operation with naphthalene . . . . [mV]
$V_{cell:2,naph}$	Measured OCV of cell:2 for the operation with naphthalene . . . . [mV]
$V_{cell:1,naph+tol+xyl}$	Measured OCV of cell:1 for the operation with with naphthalene, toluene and xylene . . . . . [mV]
$V_{cell:2,naph+tol+xyl}$	Measured OCV of cell:2 for the operation with with naphthalene, toluene and xylene . . . . . [mV]
$\Delta V_{cell:1 \mapsto 2,equ}$	Difference of Nernst voltage between cell:1 and cell:2 . . . . [mV]
ΔV_{equ}	Difference of Nernst voltage between tar loaded and tar free operation for cell:2 . . . . [mV]
ΔV_{tar}	Difference of measured OCV between tar loaded and tar free operation for cell:2 . . . . [mV]
$\Delta V_{cell:1,tol+xyl}$	Difference of measured OCV between operation with and without toluene/xylene for cell:1 . . . . [mV]
$\Delta V_{cell:2,tol+xyl}$	Difference of measured OCV between operation with and without toluene/xylene for cell:2 . . . . [mV]
$\Delta V_{cell:1 \mapsto 2,naph}$	Difference of measured OCV between cell:1 and cell:2 for the operation with naphthalene [mV]
$\Delta V_{cell:1 \mapsto 2,naph+tol+xyl}$	Difference of measured OCV between cell:1

and cell:2 for the operation with naphthalene,

toluene and xylene . . . . [mV]

ΔV_{Offset} Offset voltage between measured OCV

and Nernst voltage for tar free operation . . . [mV]

Definitions

Hydrocarbon, higher hydrocarbon, tar: The term hydrocarbon is used to include the whole spectrum of hydrocarbons. By contrast, the term "higher hydrocarbons" is used when a differentiation to "lower hydrocarbons" such as methane, ethane, propane, etc. is intended. However, a clear distinction between these two terms does not exist.

Different definitions of tar exist in literature. In this work those hydrocarbons produced during the gasification process of biomass larger than benzene are considered as tar. Eventually these are the species which are intended to be detected.

Synthesis gas: Hydrogen containing gas mixtures used for synthesis chemistry are commonly called synthesis gas. There is a wide range of the production of synthesis gas. It can be produced through steam reforming of natural gas or through gasification of coal and biomass. In this work the wood gas produced from biomass gasification is named synthesis gas as well. In particular the synthetic gas mixture from bottled gas used in the experiments in this work is called synthesis gas in order to distinguish from real wood gas. Therefore the synthesis gas may contain higher hydrocarbons or tar.

Permanent gas components: The main gas components such as H_2, CO, CO_2, CH_4, N_2 and H_2O are called permanent gas components if the synthesis gas without higher hydrocarbons or tar is addressed.

Wood gas: Wood gas is the name for gas produced in gasifiers from woody biomass and may include contaminants such as alkali, chlorine, sulphur compounds and tar.

Product gas, producer gas: Producer gas is a generic term referring to wood gas, town gas or synthesis gas [7].

Reformate gas: Reformate gas is produced by reforming hydrocarbon fuels such as methane, natural gas, diesel, methanol, kerosene, etc. The oxidant of the reforming process can be oxygen or steam.

Chapter 1

Introduction

Numerous applications exist where the information about the hydrocarbon content in a gaseous, liquid or solid phase is a significant value concerning its utilisation in downstream processes. For instance the hydrocarbon content in natural gas significantly determines the gas quality as well as the dew point. The dew point is an important parameter for the secure transport of natural gas in pipelines [24]. Condensation of hydrocarbons has to be avoided in all stages of transport.

When it comes to the energetic utilisation of natural gas, particularly the amount of non-methane hydrocarbons such as propane or butane are of major interest due to their impact on the heating value of natural gas. The design and operation of gas burners severely depends on the heating value and density of the gas mixture that is burned. The Wobbe-index for example puts those two properties in relation so as to compare different fuels concerning their operational capability in gas burners.

While natural gas is usually a very constant fuel regarding its composition as long as it comes from the same well, the gas composition of synthesis gas coming from gasification processes is rather fluctuating. This fact is a great challenge for a proper and secure utilisation of such a fuel in gas turbines or gas motors. Whereas fluctuation of the main gas components (H_2, CO, CO_2, CH_4, N_2 and H_2O) mainly affect the power output and efficiency of a gas turbine/motor the varying amounts of higher hydrocarbons can even destroy the machine when certain limits are exceeded.

In the field of tracing pollutants in liquid or solid wastes the hydrocarbon index is introduced to provide information about the concentration of hydrocarbons between C_{10} and C_{40}. Especially groundwater is assessed this way. The probe is extracted with n-hexane and measured with a gas chromatograph. The area under the peak line together with an internal standard is used to determine the hydrocarbon concentration represented through the hydrocarbon index.

Depending on the application different requirements for the measuring system can be derived. Monitoring the feed stream of a wood gas-driven gas motor or turbine requires the ability of a continuous measurement to be able to react quickly to changing gas qualities. An exact determination is of secondary importance compared to the general order of magnitude of the hydrocarbon content.

Moreover, these systems need robust and easy-to-use solutions for longterm operation. Feeding in Substitute Natural Gas (SNG) to the natural gas grid coming from the methanation of wood gas is constraining on gas quality standards. Due to the limited lifetime of the catalyst, as used for methanation, a continuous monitoring of the hydrocarbon content is desirable. Furthermore, low system costs of the application do not allow the installation of expensive sensors. In contrast, demands on the accuracy of groundwater quality checks are substantially higher. The probes are analysed externally in designated laboratories.

While gas chromatography is a very accurate method, its drawback certainly is the need for specifically skilled personnel and high investment costs. A flame ionisation detector (without GC) may be less expensive and easier to operate but provides less information about the individual concentration if more hydrocarbons are measured. For the detection of higher hydrocarbons, specifically coming from biomass gasification, the tar protocol [3] became a standard method that allows the gravimetric measurement of hydrocarbons higher than benzene through condensation in impinger bottles. Even though it is the only standardised method in this field it appears to be an inconvenient procedure due to the many steps involved and the potential sources of failures. Furthermore, it is not suitable for continuous monitoring and can only provide an average value because of the long sampling duration. Another commonly used technology is solid phase adsorption. Samples of gas are adsorbed on a solid phase and analysed in a second step in a gas chromatograph after desorption. From the operating point of view SPA is certainly one of the simplest methods. Since sampling and gas analysis are temporally separated, an implementation into a system control management is not possible.

Another challenge to the measuring device is the large diversity of hydrocarbons starting with methane, as the simplest structure, up to large molecules such as C_{40} and higher. High temperatures to avoid condensation of large molecules within the measuring device is one issue to be considered. The molecular structure is also a restriction to measurement principles based on adsorption. SPA, for example, does not work for hydrocarbons smaller than xylene. For a similar reason problems occur when using the tar protocol where benzene is not dissolved completely in the solvent used in the impinger bottles. This makes it even more complicated for applications where the monitoring of smaller and higher hydrocarbons is required simultaneously.

1.1 Identified problem: the challenge of continuous online tar measurement

One application where the monitoring of the hydrocarbon content in a gas mixture is a desired option, is the production of wood gas through biomass gasification. The wood gas coming from the gasifier contains high loads of higher hydrocarbons, so called tar, depending on the type of gasifier. For instance updraft gasifiers produce up to

$\approx 100\,\mathrm{g/Nm^3}$ tar [71]. To be able to utilise the gas in downstream processes such as a gas motor, a gas cleaning unit is installed after the gasifier. Contaminants such as sulphur, alkali, chlorine, particles and higher hydrocarbons are reduced according to the operation limits of the downstream machine. Since the higher hydrocarbons are removed over a reforming catalyst or a scrubber, degradation of either the catalyst or the scrubber liquid can lead to unwanted high tar loads after the gas cleaning unit. To avoid a fuel with a critical tar content reaching the machine, a sensor for continuous measurement appears to be a necessary and significant device to monitor the gas quality and further on initiate control strategies. However, state of the art measuring principles used in commercial sensors and detectors are not suitable to be implemented in a system due to cost and complexity reasons. Flame ionisation detectors have the major disadvantage that they only provide information about the concentration of the sum of all hydrocarbons which makes individual hydrocarbon detection difficult especially in the low concentration range when having methane as a major gas component. Using an FID equipped gas chromatograph enables very accurate measurements but is too cost-intensive and requires specifically skilled personnel. So far there is no commercial sensor on the market that fulfills the needs and requirements to economically and simply monitor the tar content of gas mixtures.

1.2 Conceptual formulation: development of a tar measuring principle

A measuring principle which has not been focused at yet for hydrocarbon measurements is the electrochemical principle. While it is a very successful and accurate technique applied in commercial CO sensors it is rather unexplored for the detection of hydrocarbons. A solid oxide fuel cell (SOFC) - a certain type of fuel cell - is able to convert not only H_2 but also CO [88]. Hydrocarbons such as CH_4 can be utilised through reforming with the combination of steam and Ni-containing anodes. In the past research concentrated on the utilisation of many different hydrocarbons such as methane, propane, ethanol or methanol. Recent results from Frank [38], Mermelstein [69, 70] and Hauth et al. [50] show that an SOFC can even utilise benzene and higher hydrocarbons to a certain extend. It was observed that the hydrocarbons present in the gas mixture contribute to the achieved cell voltage [50] when they become reformed on the SOFC anode. A clear correlation between the cell voltage and the hydrocarbon concentration provides the basis for generating a practical signal for hydrocarbon detection.

Therefore the aim of this work is to establish a measuring principle for the detection of tar similar to those obtained from biomass gasification based on the principle of an SOFC. Since the kinetics of the conversion mechanism, among others, depends significantly on the catalyst material, temperature, pressure, residence time, types of hydrocarbon and gas composition the conversion rate is coupled with these parameters

as well. The cell voltage being a result of the gas composition present at the anode eventually correlates to the conversion rate as well. This means that the cell voltage is significantly affected by the amount of hydrocarbons that are converted on the anode.

The assignment of this work, in order to establish a measuring principle, can be summarised into three main points:

- Finding out whether the reaction mechanism of synthesis gas taking place on an SOFC anode can be utilised to develop a measuring principle suitable for tar measurements.

- Investigate whether the cell voltage can be taken as a measuring signal that enables the determination of the hydrocarbon content.

- Develop a correlation model using the cell voltage as an input parameter in order to determine the hydrocarbon content.

The work requires an extensive experimental test program to gain knowledge about the characteristics of the conversion of hydrocarbons on an SOFC anode. Model tar species are picked for the experiments in order to represent the large number of tar species present in real wood gas. Therefore a single cell test rig needs to be built to carry out fundamental cell tests. The test rig should also feature prototype testing of the tar sensor. The experimental data is then used in the correlation model in order to develop the measuring principle.

1.3 Approach: from theory to practice

The intention is to develop a method that enables the determination of the hydrocarbon content using the cell voltage. Following tasks are formulated to stepwise investigate the requirements of a tar sensor as well as the correlation between the hydrocarbons present in synthesis gas and the cell voltage:

Commercial measuring principles (literature research)

Currently available measuring principles and sensors are compared (s. Chapter 2). Significant requirements for a new sensor will be determined.

Type of SOFC (literature research)

Material tests are not focused on in this work. The main issues when operating an SOFC with hydrocarbons is the ability of the cell to support the conversion of hydrocarbons and the avoidance of carbon deposition on the anode surface. Especially carbon deposition is a well investigated topic in the field of SOFC research. Conversion

of hydrocarbons on the other hand is extensively dealt with in heterogeneous catalysis research. From the combination of those two issues an appropriate anode material suitable for the use of hydrocarbons is expected to be found (s. Chapter 3).

Design and construction of SOFC test rig (constructive)

A single cell test rig for SOFCs has to be built to enable the test of synthesis gas (s. Chapter 5). Furthermore a precise addition of different hydrocarbons to the synthesis gas is an important feature of the test rig. Besides the usual voltage and current measurements the test rig should allow gas analysis at the in- and outlet of the SOFC anode.

Ideal temperature regime (experimental)

The kinetics of the reforming mechanism is dominated by the operation temperature. Usually higher temperatures affect the kinetics positively. However, temperature limitations are given due to the material of the sensor housing. Diluted hydrogen ($H_2/H_2O/N_2$ gas mixture) containing various hydrocarbons is tested on a single cell to illustrate the individual conversion behaviour. The expected result is to gain the ideal operating temperature. Furthermore, the suitability of the temperature as a control parameter for the following conceptual study is examined (s. Chapter 6).

Interaction between hydrocarbons (experimental)

Differences in the reactivity of the hydrocarbons regarding the reforming step might lead to interfering reaction mechanisms between the hydrocarbons if more than one hydrocarbon is present in the gas mixture. A general understanding about the reforming order has to be found. This is seen to be the most difficult issue since synthesis gas from biomass gasification contains a vast number of hydrocarbons which cannot realistically all be tested due to the enormous test duration necessary. Therefore model tar species need to be picked that are representative for the real tar mix present (s. Chapter 6).

Correlation model (simulative)

A correlation model to determine the hydrocarbon content using the cell voltage as an input parameter has to be established. Data about the conversion rate from the experiments are taken to build a model based on equilibrium calculations. This way it is possible to predict the open circuit voltage by calculating the Nernst voltage. By implication it is then possible to predict the conversion rate and thus the tar content respectively for a specific open circuit voltage (s. Chapter 7).

Chapter 2

Hydrocarbon measuring technologies

The detection of hydrocarbons is an important task in many fields and applications. At first this chapter intends to give an overview about several applications where hydrocarbon measurement plays an important role. This way different requirements coming from the specific application shall be pointed out. Secondly, commercial and lab-proven measurement devices and principles respectively will be explained to identify significant characteristics and properties of such instruments. A comparison of different technologies allows the assessment of the investigated hydrocarbon sensor concept regarding its suitability in the field of hydrocarbon measurement in wood gas from biomass gasification.

2.1 Selected applications for hydrocarbon measurement

The sensors and principles described in Section 2.2 mostly originate from specific applications. Some of these applications are explained hereafter in order to show where the characteristics for certain sensors and principles come from. Further, it allows the detection of similarities to the regarded task of measuring hydrocarbons in wood gas.

2.1.1 Hydrocarbon detection in water

From the ecological point of view the detection of the hydrocarbon content plays a role in contaminated groundwater, soil and waste. The chemical oxygen demand (COD) indirectly determines the amount of organic compounds in water. In [1] the COD is defined as the volumetric amount of oxygen equivalent to the mass of potassium chromate that reacts with those components of the sample which can be oxidised. In practice, cuvettes which contain the samples are used [37]. The samples including the oxidant, mostly potassium dichromate are heated for 2 h at 148 °C. Afterwards the cooled cuvette is analysed photometrically.

Another commonly used method is the hydrocarbon index. The hydrocarbon index covers the components of mineral oil between decane $(C_{10}H_{22})$ and tetracontane

($C_{40}H_{82}$) with a boiling point of 175 to 525 °C and which are not adsorbed on florisil [2]. This method focuses on mineral oil products such as kerosene, heating oil, diesel or gas oil [14]. The water probe is extracted with n-hexane and the purged extract is analysed in a gas chromatograph using a flame ionisation detector [64]. Detection limits are given by Bachema AG with 5 μg/l for total hydrocarbons and 0.5 μg/l for individual hydrocarbon components. Besides the quantitative determination a qualitative identification of the hydrocarbons is additionally achieved. This may be a significant information to locate the perpetrator of water pollution. However, pollutions concerning petrol can solely be detected qualitatively [13].

Whereas the hydrocarbon index is rather an administrative procedure to check whether pollution of water or soil has already occurred other instruments are applied to actively monitor drain water in industrial processes that is used for cooling purposes. For instance leakages in cooling systems can cause serious pollution of river water. Frech [39] classifies the possible pollutants in cooling water according Figure 2.1.
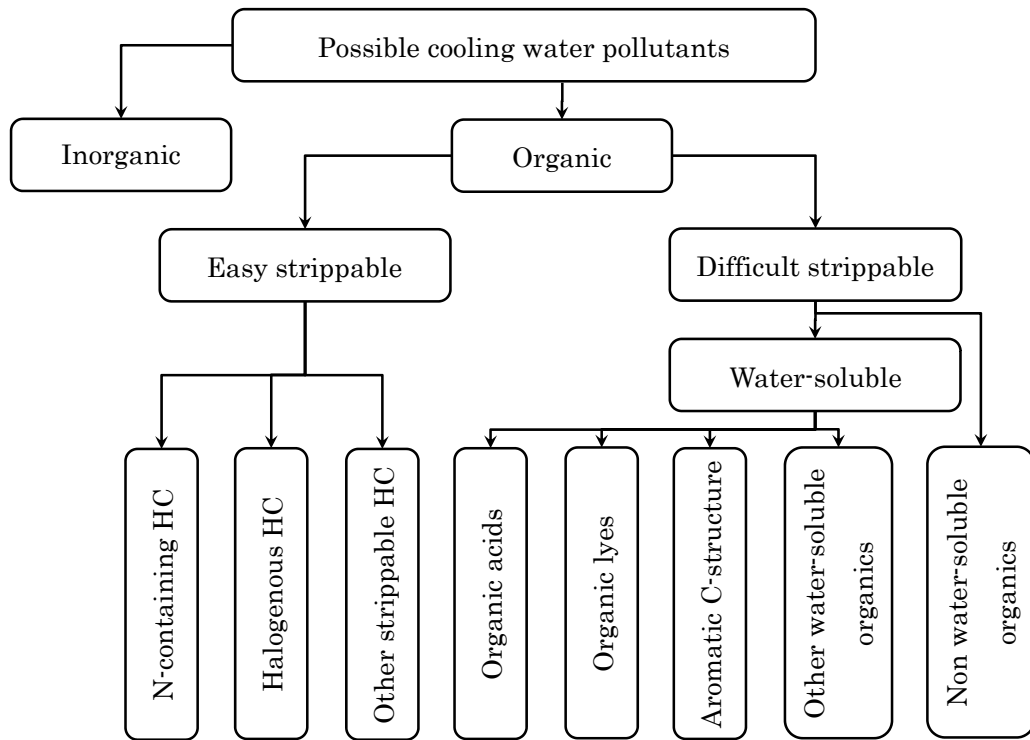
Figure 2.1: Possible cooling water pollutants (compare [39]).

This figure illustrates the diversity of hydrocarbons that are of interest. The set of respected measuring devices is globally divided in direct methods where the substance itself is detected and indirect methods where the conversion of the regarded substance

is measured. A further breakdown distinguishes between measuring the substance in a liquid or gaseous phase. Particular instruments capable to be used for monitoring, using the gas phase of the sample, are ADOS-hydrocarbon analyser, flame ionisation detector and galvanoflux. Another instrument converting the liquid sample measures the total carbon and is known under TOC (Total organic carbon) instrument.

2.1.2 Gas quality for natural gas transported in pipelines

Natural gas consists of a multiplicity of light, gaseous hydrocarbons as well as of a few higher liquid hydrocarbons. The composition strongly depends on the well of the natural gas [16, 32]. This is why the dew point of natural gas is anything but a constant value. Specifically the higher hydrocarbons have a great influence on the dew point which is defined for natural gas as the *"temperature above which no condensation of hydrocarbons occurs at a specified pressure"* [5]. Natural gas additionally contains fractions of water whose dew point is usually lower than that of the hydrocarbon mix. A combination of both water and hydrocarbons can cause the formation of hydrates in high pressure pipelines [4, 16]. These hydrates are critical due to blockages of valves and pipes. Furthermore, compressors run the risk of becoming damaged [19].

Apart from safety reasons the dew point has a great influence on production costs and on the economic value of natural gas [4]. Hydrocarbons usually become separated from the crude natural gas coming from the well in chiller plants where expansion and cooling takes place (see Figure 2.2). The more hydrocarbons have to be separated the lower the temperature and pressure has to fall. This has a direct impact to the operating costs in terms of running the turbine compressors to recompress the gas to transmission pressures. Moreover, the heating value and thus the economic value of the natural gas decreases with decreasing hydrocarbon content. For these reasons the producers are interested in sticking closely to the standards given by the supply contract [19].

Another critical aspect is the operation of natural gas-fueled turbines that require the fuel being at least $50\,°F$ above the dew point. *"If this is not achieved then the cooling effect of the expansion of large flows of fuel gas can cause liquid to be formed, resulting in possible flashback of the flame from the ignition nozzle into the mixing chamber"* [19].

The above mentioned fields of application therefore demonstrate the need for a measuring device that is capable to continuously monitor the dew point of natural gas. A widely spread system that is commercially available is described in Section 2.2.3.
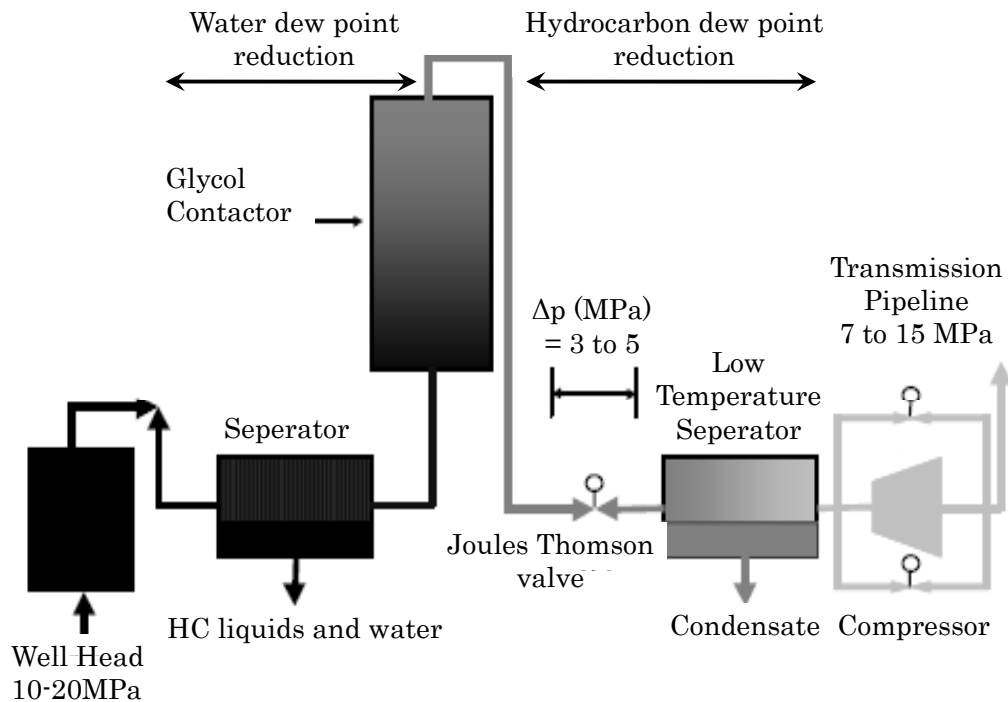
Figure 2.2: Natural gas processing method (Source: [19]).

2.1.3 Gas quality of wood gas fed applications and optimisation of the gasification process

Gasification of biomass produces a synthesis gas consisting of H_2, CO, CO_2, CH_4, H_2O and N_2. Synthesis gas can be used in several downstream processes such as a gas motor or for heating systems. Another option is the conversion of synthesis gas to synthetic methane which is called "Substitute Natural Gas". SNG can be fed into the existing natural gas pipelines. However, all of these downstream processes have strong requirements regarding the gas quality. Since synthesis gas from biomass gasification contains contaminants such as particles, alkali metals, chlorines, sulphur compounds and higher hydrocarbons a gas cleaning to a certain extend is mostly necessary to remove or minimise these contaminants. In the case of higher hydrocarbons the concentration mainly depends on the gasification technology used. Typical concentrations can be found in Table 4.2. The large difference occurs due to the different direction of the pyrolysis gas in the gasifier (see Figure 2.3). If the pyrolysis gas passes the hot reduction zone the concentration can be kept much lower.

Furthermore, the gasification process itself can be optimised in order to minimise the
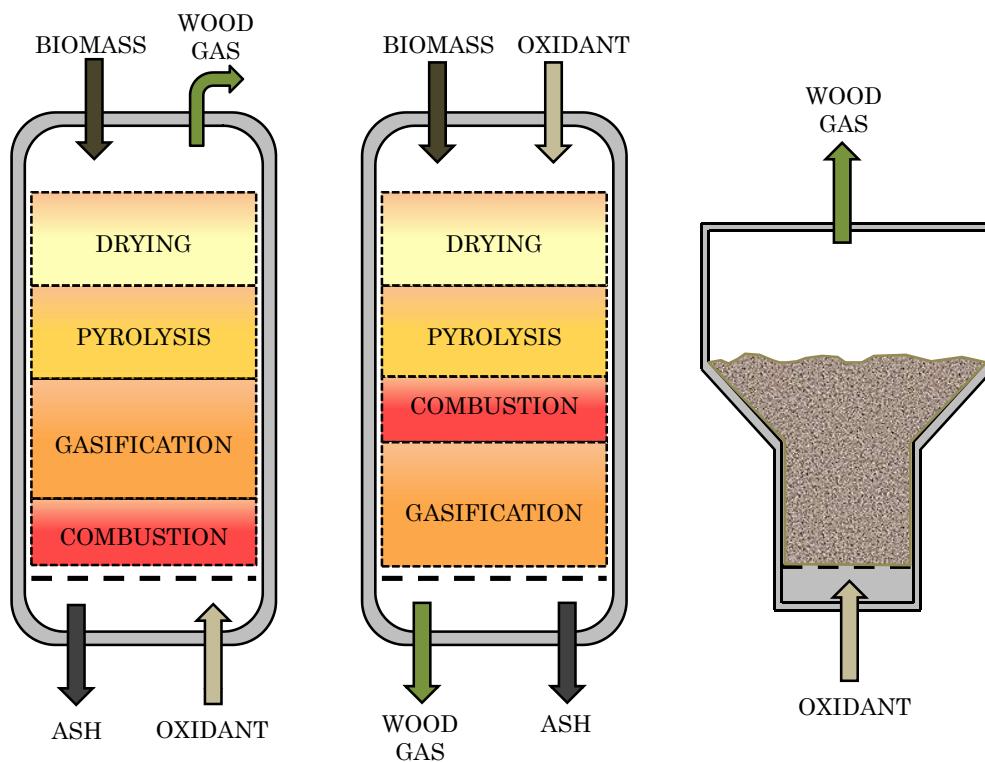
Figure 2.3: Types of gasifiers: updraft (left), downdraft (middle), fluidised bed (right).

concentration in the final synthesis gas. In fact, the concentration of higher hydrocarbons depends on many process parameters such as temperature, oxidant, residence time of the gas in the reactor, catalyst used in the gasification process (for fluidised beds) and the biomass used. The formation of higher hydrocarbons during gasification is a very complex topic which is intensively investigated. Milne et al. [71] determined different steps during the gasification process where higher hydrocarbons are generated and categorised them into primary, secondary and tertiary tar. In this context tar is a collective term for higher hydrocarbons from biomass gasification. The difficulty in understanding tar formation is based entirely on the fact that measuring tar in-line is as yet very complicated. Usually certain process steps are simplified and simulated in lab-scale test rigs. In Section 4.1 the formation of tar is described in more detail. Furthermore, representative tar species, as well as corresponding tar concentrations, are given.

An operator of a gasifier is usually interested in a simple and economic solution for tar measurement. Thus, it would be useful to have a device to continuously monitor the outlet synthesis gas quality concerning tar. The tar protocol or solid phase adsorption, which are common measuring technologies do not immediately provide

information due to the measuring procedure (s. Section 2.2.1 and 2.2.2). Figure 2.4 shows exemplarily the dependency of the tar load on the steam value σ and the gasifier temperature respectively of an allothermal bubbling fluidised bed gasifier using steam as a gasification agent. *"The excess steam ratio σ is the proportion of the fed steam relative to the stoichiometric steam demand"* [59]. These measurements are based on the tar protocol and usually take several days including the analysis of the samples. In the case of the tar protocol it is required to run the gasifier in a constant operating mode during the tar measurement which may take a couple hours. If reproducible measurements are desired, similar operating conditions have to be ensured. The analysis of the tar protocol or SPA, after the measurement, may take from several hours to a couple of weeks, depending on the fact whether the analysis is done in house or external. Hence, there is no possibility to suitably optimise the gasifier by changing process parameters and immediately looking at the resulting gas quality.
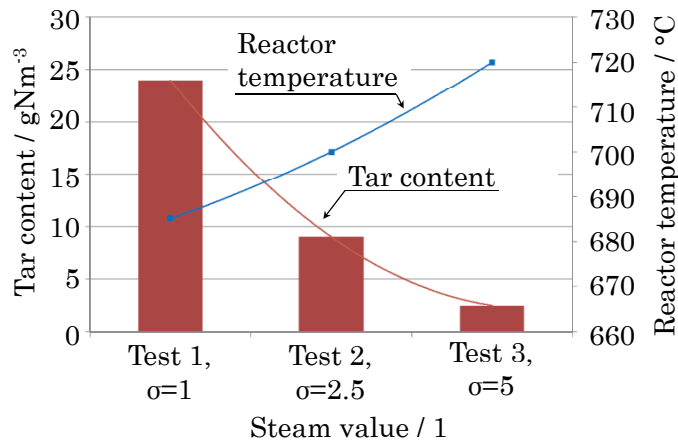
Figure 2.4: Tar content depending on steam value σ (=ratio between real amount of steam to stoichiometric amount of steam needed for gasification) (Source: [59]).

The application of biomass-derived fuel in gas motors and micro gas turbines is investigated frequently [25, 46]. In particular the changing operating characteristic of gas turbines with low calorific fuels such as wood gas is a big issue in the first place [79]. Moreover, the gas quality of producer gas coming from the gasifier has to meet stringent requirements concerning contaminants such as tar. The maximum allowable tar content for gas motors required by the manufactures for example must not exceed $50\,\mathrm{mg/Nm^3}$ because tar condensation can be a problem for certain valves. Crystallisation of gaseous tar at cold spots may cause a malfunction of such valves. Gas turbines encounter similar problems at the cold compressor inlet in case that atmospheric gasification requires compression of the syngas.

Table 2.1 shows the concentration of hydrocarbons in producer gas that is tested in

Table 2.1: Hydrocarbons in synthesis gas after gas cleaning for utilisation in a micro
gas turbine (compare [79])

Component	Average [vol.%]	Minimum [vol.%]	Maximum [vol.%]
CH_4	4.2	3.7	4.5
C_2H_2	0.23	0.17	0.34
C_2H_4	1.7	1.4	1.9
C_2H_6	0.09	0.05	0.13
C_6H_6	0.23	0.21	0.26
C_7H_8	0.017	0.013	0.022
tar	-	-	0.002

a $30kW_{el}$ micro gas turbine from Capstone [79]. The gas is produced in a $500kW_{th}$ circulating fluidised bed. Gas cleaning comprises dust, tar, water and NH_3 removal. It is not exactly mentioned which species are seen as tar but it is indicated that the main component responsible for 40% of the total tar content of $90\,\text{mg/Nm}^3$ after the gas cleaning is naphthalene. If benzene (C_6H_6) and toluene (C_7H_8) in Table 2.1 were counted to the total tar the tar load would exceed the $90\,\text{mg/Nm}^3$ by far. However, no problems occurring from the tar content in the utilised gas have been reported.

Certainly the combination of an atmospheric biomass gasifier and a micro gas turbine or a gas motor require low concentrations of higher hydrocarbons. Thus it becomes obvious that monitoring the gas composition either at the gasifier outlet or at some point between the gas cleaning and the gas motor/gas turbine is essential to prevent the machine from malfunctioning.

2.2 Commercially available measuring devices and systems

After explaining the needs and requirements of notable applications where hydrocarbons have to be measured, eventually commercial sensors or measuring systems used are shown in more detail in the following subsections.

2.2.1 Tar protocol

The tar protocol is a development specifically for the determination of organic tar coming from biomass gasification. In this context, hydrocarbons higher than benzene C_6H_6 are considered as tar. The tar protocol allows to find:

- Concentration of gravimetric tar in mg/Nm^3. The range is typically from 50 to $300\,\text{mg/Nm}^3$ at relevant sampling point conditions (0 - 900 °C, 0.6 - 60 bar).

- Sum of the concentrations of GC-detectable tar in mg/Nm^3.

The discontinuous sampling of a gas stream containing organic tar and particles under isokinetic conditions is carried out in two steps; sampling and analysis. Figure 2.5 demonstrates the sampling test set-up for the tar protocol. A constant gas stream from the gasifier is sucked through the impinger bottles. The solvent used in the impinger bottles is isopropanol. Both condensation and absorption of tar occurs in the impinger bottles. After sampling, the solvent is given to a Soxhlet extractor to remove the isopropanol from tar. The residue can then be weighed and considered as the gravimetrical tar. In combination with the volume flow which is adjusted during sampling, the concentration of tar in the producer gas stream can then be calculated [3].

Another option is to inject a probe of the residue to a gas chromatograph in order to detect the individual tar concentration [3]. However, this is a very complex measurement since the calibration of the gas chromatograph requires GC-specific knowledge such as the retention time of the tar species. The retention time is one reason why the gas chromatograph needs to be calibrated individually for each tar species.
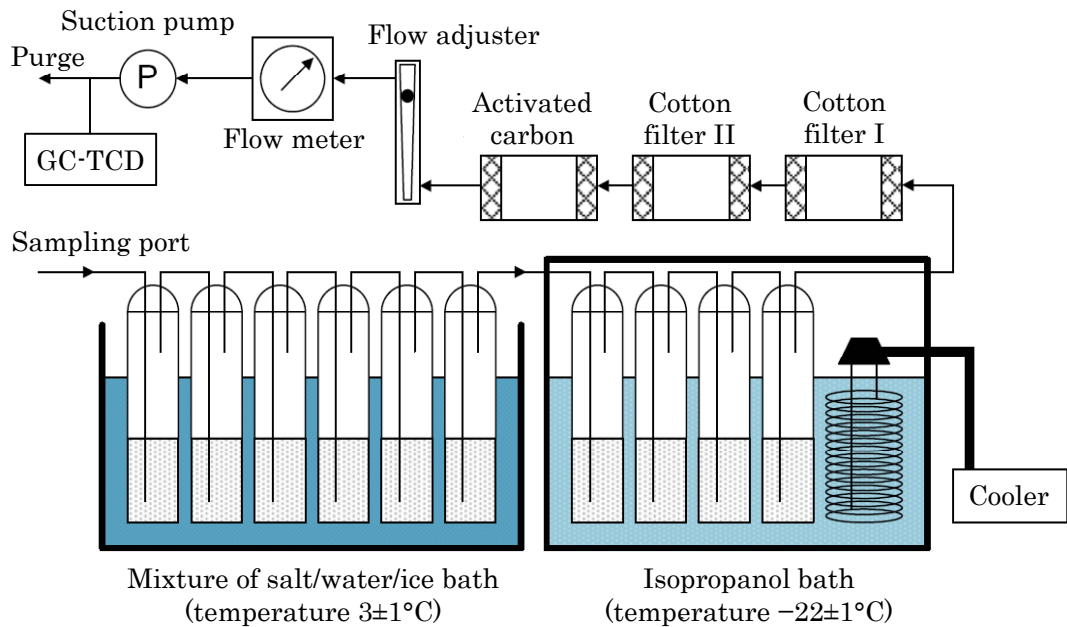
Figure 2.5: Test set-up of tar protocol (Source: [78]).

Generally the gravimetrical method is a relatively easy approach to determine trends considering the tar load for different operating modes of the gasifier. However, the tar protocol is less satisfying when the optimisation of the gasifier is focused on. The long sampling duration $\approx$ 30-60 min and the even longer analysis does not allow continuous measurement. Furthermore, it has to be noticed that the result is a mean value due

to the long sampling duration. Peaks or variations of the gas quality based on the discontinuous gasification process cannot be detected.

2.2.2 Solid phase adsorption (SPA)

SPA is a method to measure higher hydrocarbons transported in the gas phase. The gas mixture passes a specific adsorbent where the higher hydrocarbons become adsorbed. Then the adsorbent is kept in a gas-tight container and further analysed in a gas chromatograph. There the adsorbent becomes eluted with e.g. helium. The adsorbed hydrocarbons will be desorbed and conducted to the gas chromatograph. This is a convenient method since the sampling with the SPA column and the analysis with the gas chromatograph can be separated in two steps. The method is suitable to detect hydrocarbons with a molecular weight between benzene ($78.11\,\mathrm{g/mol}$) and coronene ($300.36\,\mathrm{g/mol}$). More information on SPA can be found in [22, 23, 30].

2.2.3 Hydrocarbon dew point measurement

Direct and indirect methods for the determination of the hydrocarbon dew point in natural gas are applied in practice. Direct methods for example use chilled mirrors where the formation of a film of liquid condensate is optically detected. This optical detection can be carried out either manually or automatically. For the indirect method a gas chromatograph measures the individual concentration of the hydrocarbon species. These amounts are then taken to calculate the dew point through a thermodynamic equation of state. However, higher hydrocarbons ($>C_{11}$) may be present in very low quantities that are below the detection limit of the instrument [24]. This can lead to divergences between the theoretical and the real dew point since the higher hydrocarbons significantly affect the dew point. Therefore a detection limit of $0.1\,\mathrm{ppm}$ is suggested. A comparison [19] shows the difference of the theoretical dew point being $\approx 57\,\mathrm{K}$ apart when only taking into account all hydrocarbon species up to either C_{14} or C_6. The advantage of the indirect method is that the whole dew point curve over a wide pressure and temperature range as in Figure 2.6 can be calculated.

Figure 2.7 shows the cross section of a commercial hydrocarbon dew point analyser. The light beam emitted from the LED is directed towards the glass at an angle that enables full reflection within the glass matrix. A small area in the middle of the surface is prepared to decouple the light beam C as long as condensation does not occur. Light beam A illustrates the part of the light arriving at the photo diode if no condensation takes place. Once condensation starts a liquid film is formed on the surface. The boundary layer between condensate and gas on the prepared surface reflects all of the light back into the glass matrix. This way an offset of the light beam B arriving at the photo diode is created which allows the detection of the beginning of condensation. In order to cool the mirror accurately a Peltier cooling element is positioned right under the mirror. The temperature is measured with a Pt-1000 that
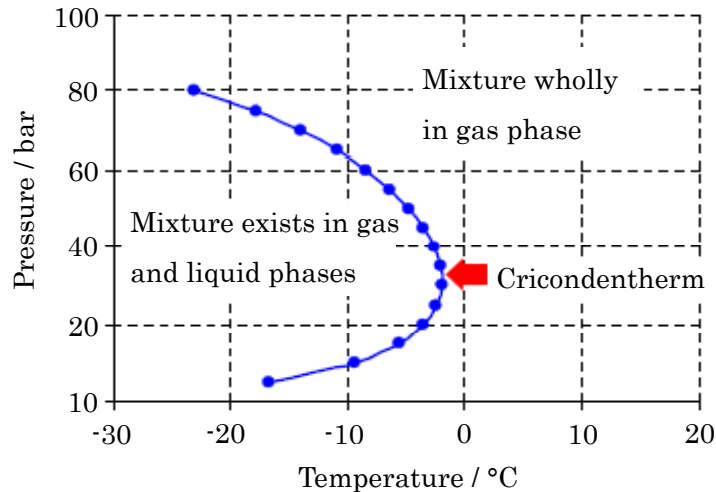
Figure 2.6: Typical hydrocarbon dew point curve of natural gas. The cricondentherm (indicated by the arrow) is defined as the maximum temperature (at any pressure) at which condensation can occur (Source: [24]).

is vapor-deposited around the condensation area. This system has the advantage that the light is not conducted through the gas phase [16].

2.2.4 Flame ionisation detector (FID)

A very common and robust instrument is the flame ionisation detector shown in Figure 2.8. The gas that has to be analysed enters the FID where it is heated up in an electric oven. Hydrogen and oxygen are used to produce a combustible gas mixture. The mixture of sample gas and hydrogen travels up to a nozzle where it is burned with oxygen. This way the hydrocarbons are ionised resulting in reduced carbon ions created by the flame. A voltage difference between the electrode in the flame and the collector plate outside the flame repels the ions towards the collector plate and produces an electrical current which can be measured and used as a measuring signal. The FID works well for hydrocarbons due to the high amount of carbon atoms. Carbon which is already partly oxidised produces a weaker signal as molecules containing carbon and hydrogen only [7]. The FID is only able to measure the sum of the concentration of all hydrocarbons entering the detector. Therefore it is impossible to distinguish between the hydrocarbons. This seems to be a problem for a synthesis gas containing methane. If the methane concentration is high it is difficult to determine low concentrations of other hydrocarbons present in the gas mixture.

① Gas
② Light beam
③ LED
④ Peltier element
⑤ Glas substrate
⑥ Photo diode
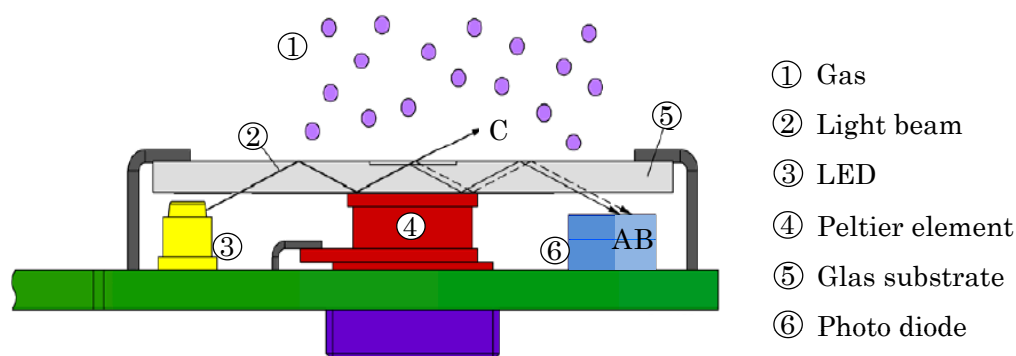
Figure 2.7: Cross section of a commercial dew point meter (Source: [16]).

Gas chromatography with FID detector

FID are often used as detectors in gas chromatographs. The gas chromatograph splits the individual components of the sample gas while it is conducted through a capillary column. The capillary column can be filled with a certain substrate which interacts with the gas molecules from the sample gas. The interaction forces vary in strength for the individual sample gas molecules and cause them to pass the column at different rates. In the case of hydrocarbons this rate is mainly influenced by the boiling point of the molecules which enables the separation of the molecules in the column. This way it is possible to detect single species because the molecules arrive at the detector one after the other.

2.2.5 Mass spectrometer (MS)

Another detector that is commonly used in a gas chromatograph is the mass spectrometer. The MS measures the mass-to-charge ratio of charged molecules. Typically the sample is ionised with an electron beam to generate the charged molecules (ions). The ions are separated by an electromagnetic field that deflects the ions depending on their mass and charge. A commonly used type is the quadrupole mass spectrometer (see Figure 2.9). Only ions with a specific mass-to-charge ratio are able to pass the electromagnetic quadrupole field between the four rods and consequently enter the detector.

The mass spectrometer can be used for a large variety of molecules. Furthermore, the MS allows the characterisation of molecule structures or isotopes. It is a very powerful instrument for analytical chemistry. The analysis of the mass spectra requires
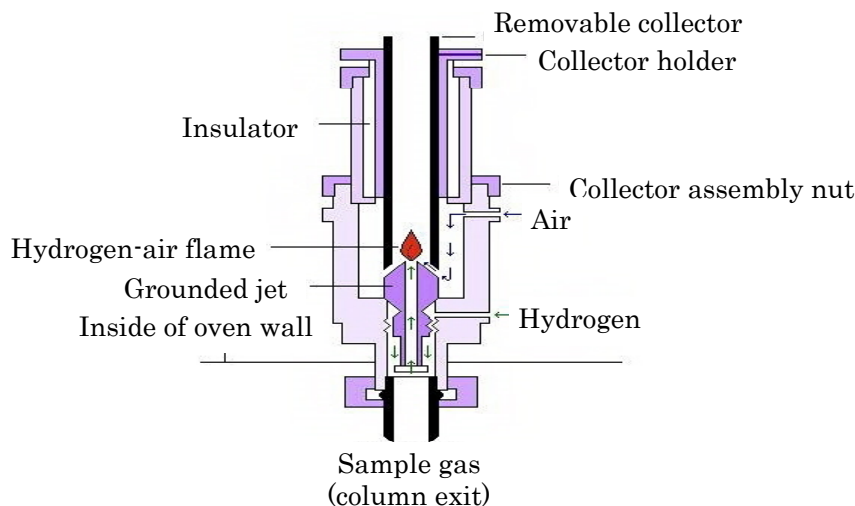
Figure 2.8: Cross section of a flame ionisation detector (Source: [6]).

experienced personnel. Moreover, the combination of a GC and an MS usually makes this measuring technique a complex task [7].

2.2.6 Total organic carbon-instrument (TOC)

The TOC can be used to measure the total organic carbon in water. The water is purged from inorganic carbon. Afterwards the organic bound carbon is converted into CO_2 either thermally at $900\,°C$ or with UV-radiation. The produced CO_2 is stripped and measured in the gas phase with an infra-red detector. The advantage is that the conversion is $100\,\%$. However, the instrument is high-maintenance due to contamination of the oven [39].

2.2.7 Hydrocarbon analyser based on heat tone principle

As illustrated in Figure 2.10 the sample gas is conducted over a reference point and the actual measuring point. The measuring point consists of a catalyst material where the oxidation of hydrocarbons in the sample gas takes place. A thermocouple is used to measure the temperature difference between the reference and the measuring point caused by the oxidation which correlates to the concentration. This technology is capable to detect any hydrocarbon compound except chlorinated and sulphuric hydrocarbons [11]. Determination of individual hydrocarbon species in a mix is not possible.
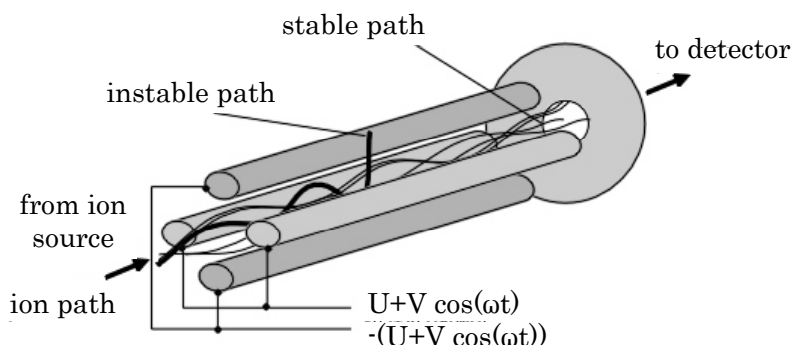
Figure 2.9: Cross section of a quadrupole mass spectrometer (compare [8]).

2.2.8 Draeger tubes

The Draeger tubes consist of a closed glass body filled with a substrate. The substrate is coated with a substance that reacts with a specific gas causing a distinct color change of the substrate. The measuring gas is sucked through the glass body with a manual gas pump. On the outside wall of the glass body a scale indicates the concentration. The higher the concentration the more substrate changes the color. A certain gas flow through the glass body has to be guaranteed. The attached manual gas pump enables a distinct volume that is sucked through the tube each time the pump is pressed and released. For very low concentrations the pump has to be pressed more often to achieve a higher total volume through the tube.

This method is certainly one of the simplest for fast gas analysis. The measurement approximately takes one minute and is very convenient in field tests where no electrical power supply is available. No calibration is necessary. Substrates are available to detect about 500 different gas species [29]. Thus it enables the detection of hydrocarbons such as benzene or toluene. However, the detection of only one species at the same time is possible.

2.2.9 Non dispersive infra red detection (NDIR)

An infrared spectrum is radiated alternately through a measuring and a reference cuvette using a chopper wheel. The measuring cuvette is perfused with the sample gas. Each molecule of the sample gas absorbs a specific wavelength of the infrared light according to the Lambert-Beer law. The reference cuvette is filled with nitrogen, therefore no absorption takes place. The infrared passes two parallel cuvettes and both
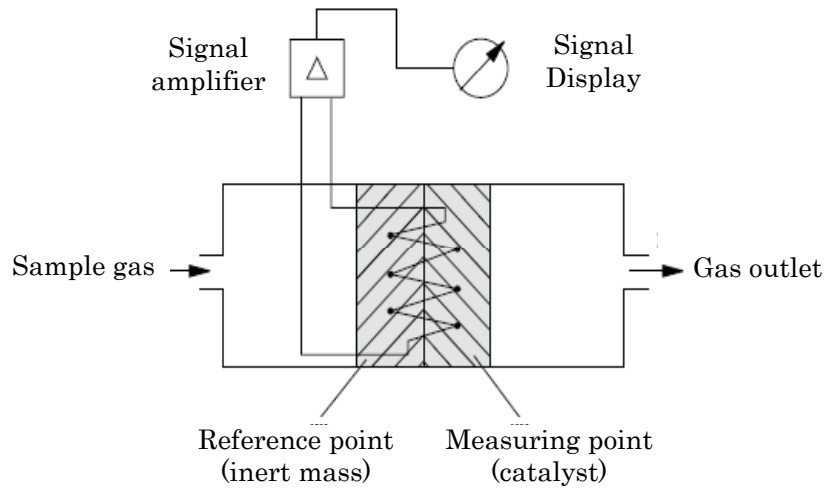
Figure 2.10: Cross section of a hydrocarbon analyser (Source: [11]).

the spectrum of the measuring cuvette and the reference cuvette eventually hit the receiving chamber. The receiving chamber is filled with the gas species which should be detected. The infrared light from the sample gas has a significantly reduced intensity at the wavelength which is absorbed in the measurement cuvette. If the sample gas contains the same species as the receiving chamber then no absorption takes place at this specific wavelength in the receiving chamber. The infrared light coming from the reference cuvette still has the full spectrum and thus absorption in the receiving chamber takes place. The receiving chamber for the infra-red light coming from the measurement and the reference cuvette are separated by a membrane. Due to the different levels of absorption between the two receiving chambers measurable pressure difference occurs which correlates to the concentration of the component that should be measured.

This principle works for the continuous detection of CO, CO_2, NO, SO_2, N_2O, CH_4, NH_3 and a few hydrocarbons between C_2 and C_6 according to [10]. Technically it has to be guaranteed that the dew point of the sample gas is not undershot except for water. Usually a cooler is installed before the gas enters the measuring cuvette in order to condense the water of the sample gas. Therefore, condensation of other species such as hydrocarbons with boiling points above the cooler temperature ($\approx 2\,°C$) cannot be avoided. Therefore only low concentrations of light hydrocarbons can be detected. A detection of tar is probably not possible for this reason.

2.2.10 Galvanoflux

The Galvanoflux measures chlorinated hydrocarbons in liquids. The instrument is installed behind a stripping unit where chlorinated hydrocarbons are transfered from the liquid to the gas phase. After this step a thermal decomposition to chlorine takes place. The chlorine then is measured in a fuel cell [39].

2.2.11 Lambda sonde

Although the lambda sonde is not a sensor to measure the hydrocarbon concentration it is mentioned because it uses a solid electrolyte similar to an SOFC. The lambda sonde is a device to measure the oxygen content in hot exhaust gas of combustion engines. The oxygen content is an important parameter to control the air-to-fuel ratio in automotive applications. A Nernst cell made of YSZ-electrolyte uses Pt electrodes. Pt electrodes are resistant to oxidation in the exhaust gas atmosphere at high temperatures. At the cathode a reference gas (air) is used while the anode is exposed to the exhaust gas. For operation $\lambda < 1$ the oxygen partial pressure in the exhaust gas is very low. For an increasing air-to-fuel ratio the oxygen partial pressure jumps significantly at $\lambda \geq 1$. This increased oxygen partial pressure directly influences the Nernst voltage which is eventually taken as the sensing parameter [7].

2.3 Lab proven measuring principles

2.3.1 Fluorescence spectroscopy

Tar species such as naphthalene, phenol and toluene are stimulated at a certain wave length by a light source and therefore achieve a higher energy level. After the stimulation the molecules fall back to their original lower energy level and emit light with a specific wave length for each molecule. The possibility of tar online analysis using fluorescence spectroscopy is investigated by Baumhakl and Karellas [17, 18]. As a light source low-cost LEDs (265 and 395 nm) are tested. The results show that the gained fluorescence signal corresponds with the tar concentration in the product gas.

Similar investigations are performed by Sun et al. [89] with 266 nm Laser. The method enables more specific excitation of the tar molecules and therefore higher differences of the peak shapes (peak width and peak hight) are achieved. This may enable a differentiation of the different tar groups or molecules.

2.3.2 Electrochemical principles

For the detection of propene in exhaust gas of combustion engines Elumalai et al [34] reports the development of a NiO/Au composite sensing electrode based on YSZ sensor. Exhaust gas mainly contains carbon monoxide, nitrogen, steam and small quantities of oxygen. Therefore 10-400 ppm propene mixed in humidified oxygen/nitrogen gas (5 % O_2, 5 % H_2O and balance N_2) is tested with the sensing electrode. A reference electrode supplied with the base gas composed of humidified oxygen/nitrogen gas only is used to build a voltage difference that is eventually used to measure the propene sensitivity of the sensing electrode at 600 °C. A logarithmic correlation between the propene concentration and the voltage difference is shown in Figure 2.11.
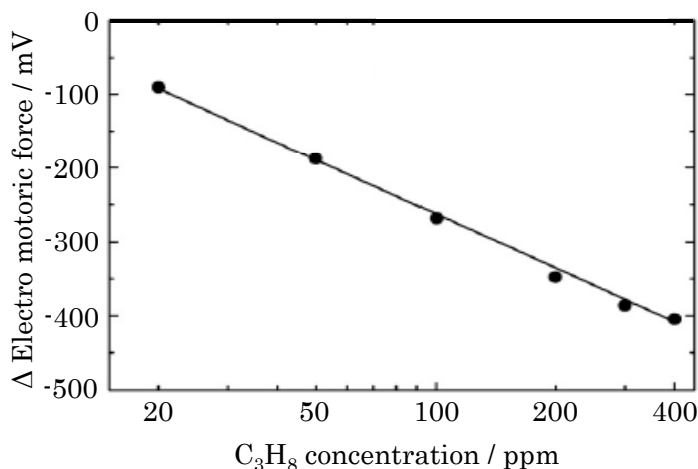
Figure 2.11: Logarithmic correlation between voltage and propene concentration of a NiO/Au-YSZ sensing electrode at 600 °C (Source: [34]).

The mechanism at the sensing electrode is not explained by Elumalai et al. However, an oxidation of propene at these conditions is likely. Consequently the gas composition, especially the oxygen partial pressure at the sensing electrode will change. A reduction of the oxygen partial pressure significantly increases the Nernst potential at the sensing electrode. Hence, a measurable voltage difference between the sensing and reference electrode is caused.

Dutta el al. [31] investigated the performance of a $La(SrGaFe)O_3$ electrolyte sensor. The active electrode is composed of $(Pt_{0.9}Co_{0.1})_{0.9}((CeO_2)_{0.8}(LaO_{1.5})_{0.2})_{0.1}$. As inactive electrode $La_{0.5}Sr_{0.5}MnO_3$ is used. Both electrodes are exposed to the same environment (1 % O_2, C_3H_6 and balance N_2). The operating temperature is 423-673 K. The sensor is operated at 0.5 V in the amperometric mode. A distinct sensitivity is found not only for C_3H_8 but also for alkanes and alkenes (see Figure 2.12).
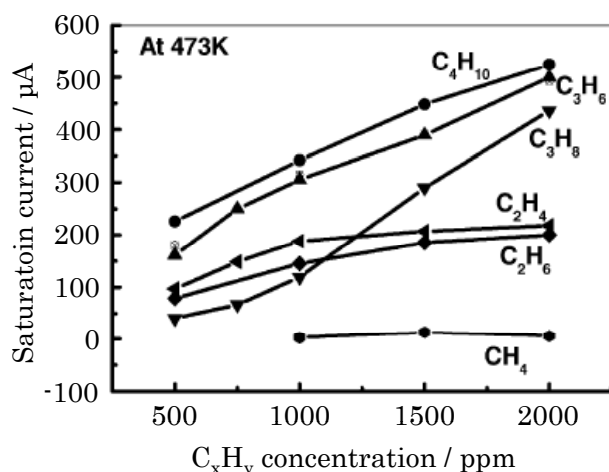
Figure 2.12: Sensitivity for C_3H_8, C_4H_{10}, C_3H_6, C_2H_4, C_2H_6 and CH_4 at 473 K in amperometric mode (Source: [31]).

The sensitivity effect is explained by electrochemical oxidation of hydrocarbons at the active electrode through oxygen ions. At the inactive electrode no oxidation of the hydrocarbons takes place. While other hydrocarbons besides C_3H_8 show good sensitivities, CH_4 seems to be highly tolerant to oxidation at low operating temperature. There are apparently no cross sensitivity effects concerning other gas components such as H_2 and CO. It is assumed that these components will be oxidised on the active electrode as well as on the inactive electrode, thus balancing the sensitivity effect.

Measurements of higher hydrocarbons than C_4H_{10} have not been reported in [34] and [31]. However, the described mechanism requires the presence of oxygen for the oxidation of the hydrocarbons which is not the case for synthesis gas. Therefore, this principle is not applicable for synthesis gas. Furthermore, it is not clear whether water could be an alternative oxidant in this principle.

A sensor principle to detect higher hydrocarbons as well is presented in a patent of the United States Department of Energy [9] for the detection of benzene, toluene, methane and other organic compounds in a concentration range of 1-100 ppm. The idea is to guide the sample gas over a heat element with a catalytic surface. The surface supports the catalytic oxidation of the components that should be detected. However, it is not clearly mentioned what type of oxidant is used. The heating element can also be used as a sensor. The product gas is then further directed to an electrochemical sensor. The differences of the electrochemical activity of the product gas, due to the catalytic oxidation, generates a measurable signal.

2.4 Summary and overview

Although a variety of commercial hydrocarbon detectors and measuring principles exist there is still a lack of a tar sensor that can be utilised in biomass gasification. Table 2.2 summarises the most important properties and shows the benchmark criteria for a biomass tar sensor. A continuous on-line sensor where the hydrocarbon concentration is displayed in-situ is inevitable in order to improve gasification technologies. Compared to the total cost of a biomass gasifier the sensor must be relatively cheap. The approximate price an operator is willing to invest is estimated at 2000 €. Furthermore, operating the sensor must be simple for the operating staff without the need of extensive training or specific background knowledge.

Concerning the targeted hydrocarbon species that need to be measured it is sufficient to measure C_6 to C_{16}. A clear differentiation must be possible between the detection of methane and tar. It is not necessary to measure the individual tar concentration, however a distinction between secondary and tertiary tar is desirable. The upper detection limit is around 3000 ppm to cover typical concentration levels that occur in biomass gasification.

Another important parameter is the operation temperature of the sensor. Ideally the operation temperature of the sensor is as high as the temperature of the process gas stream in order to avoid condensation of tar species. In case the sensor temperature is higher a conversion of the hydrocarbon species before the sensor and thus a change of the composition must be avoided. Since gas phase reactions between the gas components are not assumed, only catalytic surface reactions in the gas supply pipes and the sensor casing must be avoided under all circumstances.

Table 2.2: Overview about commercial measuring technologies for the detection of hydrocarbons in the gas phase

Property	GC[1]	FID[2]	SPA	TarP[3]	DewP[4]	DrTu[5]	NDIR	BeMa[16]
Complexity sampling	middle	low	low	medium	low	low	low	low
Complexity analysis	high	high	high	middle/high	middle	low	low	low
Measurement	on-line	on-line	on-line	on-line	on-line	on-line	on-line	on-line
Analysis	in-situ	in-situ	off-line	off-line	in-situ	in-situ	in-situ	in-situ
Range [ppm]	any	0-100000[20]	any	any	0-15000 [16]	0-1800^6 [29]	0-500^7 [10]	0-3000
HC-species	all	all	$\approx C_9$-C_{24}	$>C_6$	$>C_3^8$	specific^9	C_1-C_6^{10} [10]	C_6-C_{16}
multiple HC[11]	yes	no	yes	no^{12}	no	no	yes	yes^{17}
Sampling time	6 - 20 min	continuous	≈ 2 min	$\approx 1\,^1/_h$	10-30 min [16, 19]	≈ 2 min	continuous	continuous
Operating temperature [°C]	$\approx$20-200	$\approx$200	ambient	ambient	below dew point	ambient	n.k.	>500
Skills Personnel	high	medium	low^{13}	medium^{13}	low	low	low	low
Costs	$\approx$50000 €	$\approx$10000 €	$\approx$2 €^{14}	$\approx$2500 €	-	$\approx$10 €^{15}	$\approx$15000 €	$\approx$2000 €

^{1}either GC/FID or GC/MS is meant
^{2}portable FID without GC
^{3}Tar protocol
^{4}Dew point sensor
^{5}Draeger tube
^{6}Benzene
^{7}2-Methylpentane
^{8}depends on minimum cooling temperature of the sensor
^{9}a list of species can be found in [29]
^{10}only alkanes except C_2H_2 and C_2H_4
^{11}more than one hydrocarbon can be detected simultaneously
^{12}for gravimetric measurement
^{13}not considering the analysis part
^{14}costs per column, external analysis costs not included
^{15}costs per tube
^{16}Benchmark
^{17}only distinction between secondary and tertiary tar necessary

The concept of the hydrocarbon measuring principle focused on in this work is based on a commercial solid oxide fuel cell. SOFCs are known to be an adequate cell for the use of synthesis gas in power generation. It resists the harsh atmosphere at the anode and can be operated up to $1000\,°C$. The idea is to use the electrochemical potential depending on the hydrocarbon concentration to generate a measuring signal. The following chapter investigates the use of hydrocarbons in synthesis gas in SOFCs and their impact on the electrochemical cell potential.

Chapter 3

Conversion of hydrocarbon fuels on SOFC anodes

In the past great efforts have been undertaken to understand the mechanisms to use hydrocarbon fuels in SOFCs. Mainly because this is an important step for the commercialisation of SOFCs using any kind of hydrocarbon fuels based on fossil fuels such as natural gas, jet fuel, coal gas or on biomass fuels such as wood gas from biomass gasification, biogas from fermentation or methanol. Therefore the intention of many investigations is to find safe operating conditions in order to achieve an expected lifetime of 40000 to 80000 h [90] as is necessary for power plant applications.

The requirements of a tar sensor are different compared to those of power plants. Degradation is not as important since the cell in a tar sensor can be easily replaced. Furthermore, the percentage of the cell costs compared to the overall system costs of the sensor are relatively low. However the reaction mechanisms on the SOFC anode of a tar sensor are similar to those of commercial SOFC power plants and can be considered when developing a tar sensor based on an SOFC.

The concept of the tar sensor is to measure the contribution to the electrochemical potential caused by the higher hydrocarbons present in the wood gas of a biomass gasifier. A comparison between a tar-loaded fuel gas and a tar-free fuel gas [38] shows a clear voltage increase that can be attributed to the conversion of higher hydrocarbons. The ability of a nickel containing anode to convert higher hydrocarbons due to the reforming and shift reaction results in an increase of the Nernst potential due to the increase of the partial pressure of H_2 and CO. However, this concept is based on the prerequisite that the reforming and shift reaction are the main responsible reactions for the conversion of higher hydrocarbons. Catalytic cracking, for example, would cause carbon deposition which results in different partial pressures and cell voltages respectively compared to reforming. In fact, the types of catalytic reactions taking place on the anode surface strongly depend on the operating conditions, anode structure/material and gas composition. When focusing on the conversion of hydrocarbons the following reactions need to be considered for the operation of an SOFC with wood gas from biomass gasification:

- direct oxidation of hydrocarbons

- dry reforming with CO_2

- steam reforming in combination with water gas shift reaction

For example dry reforming of methane can be expected at very low steam contents in the presence of significant amounts of CO_2 while steam reforming is dominant at higher steam contents. The water gas shift reaction clearly depends on the available amounts of CO, H_2O, H_2 and CO_2 and can be expected to be very close to equilibrium in the presence of a catalyst at temperatures between 800 and 900 °C. Carbon deposition, to a high degree, depends on the steam content and the catalyst material used. An extensive study about carbon formation on Ni-anodes for the operation with methane for example is shown by Biber [21]. Furthermore, high levels of current density have shown carbon removal due to direct oxidation of deposited carbon. Additionally, temperature has a severe impact on carbon deposition. On the other hand, high levels of H_2O and high current densities can cause the oxidation of the nickel catalyst in the anode. This eventually deactivates the anode and in the worst case leads to physical damage of the anode due to stresses caused by the expansion of the NiO particle. Even though there has not been much evidence yet of the direct electrochemical oxidation of higher hydrocarbons, this possibility needs to be kept in mind as well when operating an SOFC with high levels of methane and higher hydrocarbons.

Based on the gas mixture as obtained from biomass gasification all the afore mentioned mechanisms have to be considered in order to correctly interpret the cell voltage and give a statement about the reactions at the anode. Otherwise a reliable correlation between the tar content and the cell voltage cannot be found. Furthermore, to find the ideal operating conditions of the sensor requires a comprehensive knowledge of the behaviour of the reaction mechanisms. For example, the temperature greatly influences the kinetics of hydrocarbon reforming. The impact of the current density on reforming mechanisms has not been investigated yet. The resistance of the used cell against carbon deposition to operate the sensor in a safe mode needs to be determined as well. Taking all these points into consideration the following literature research intends to figure out the crucial topics concerning the operation of the tar sensor.

3.1 Direct hydrocarbon oxidation

The use of hydrocarbons on the anode of an SOFC raises the question whether the hydrocarbons can be electrochemically oxidised directly as H_2 and CO or if a preliminary reforming step is necessary. This question is closely linked to the hazard of carbon deposition when operating an SOFC on dry hydrocarbon fuel. *"Generally, in steam reforming catalysis, steam-to-carbon ratios of around 2.5-3 are used, i.e. well in excess of the stoichiometric requirement, such that the equilibrium of the water gas shift reaction lies to the right to maximise H_2 production and minimise carbon deposition through hydrocarbon pyrolysis and the Boudouard reaction"* [88].

Direct oxidation of dry methane on Cu/ceria anodes

While conventional Ni-containing anodes face the risk of becoming deactivated at low steam-to-carbon ratio, alternative anode materials such as Cu/ceria-YSZ anodes show the possibility of direct hydrocarbon oxidation. A comparison by Gorte et al. [41, 42] of the theoretical conversion rate based on electrochemical oxidation of undiluted dry methane with that gained from gas analysis at 800 °C for a $CeO_2/Cu/YSZ$ anode show great accordance (see Figure 3.1). CH_4 conversion as well as CO_2 production increase linearly with increasing current density. Very poor performance is achieved using CH_4 as fuel over a Cu/YSZ anode without ceria. No electrochemical oxidation is observed when measuring a V-i curve. This fact leads to the assumption that ceria oxide acts as an oxidation catalyst which is oxidised by the oxygen ions coming from the cathode and is subsequently reduced by the fuel. In this case Cu is only an electronic conductor but not a catalyst for direct oxidation. Images of a Ni-YSZ cermet and a Cu-YSZ cermet, after heating in a dry mixture of CH_4 and toluene at 700 °C for 1.5 h, show complete physical damage of the Ni cermet whereas only a shiny graphite layer is observed on the Cu cermet which can be removed by scrapping. This result points out that the carbon deposition mechanism is different between Ni and Cu cermets. Carbon dissolution into the bulk metal and precipitation of carbon on the surface occurs when using Ni. This can cause very high pressure in the bulk metal, eventually breaking the Ni cermet. On the other hand only surface layers of carbon compounds appear on Cu cermets.

Direct oxidation of higher hydrocarbons on Cu/ceria anodes

More evidence of direct oxidation of hydrocarbons are presented by Park et al. for n-butane, toluene, methane, ethane and 1-butene [77] and by Gorte et al. for decane, toluene and diesel [42]. All hydrocarbons except toluene show good performance results. While toluene could not be used as a fuel for a Cu-ceria composite anode, stable operation is achieved with a Cu-samaria doped ceria anode.

Direct oxidation of liquid hydrocarbons on Cu/ceria anodes

Direct-utilisation of liquid hydrocarbons over a Cu-ceria-YSZ anode between 700 and 800 °C for undiluted n-decane, light naphtha, heavy naphtha and a mixture of 20 vol.% toluene and 80 vol.% n-decane are performed by Kim et al. [60] in order to investigate the mechanism of carbon deposition and therefore the impact of the anode material used. V-i curves principally show the ability to directly utilise hydrocarbons on the anode. It is not clearly mentioned whether direct electrochemical oxidation of the hydrocarbons is assumed or if electrochemical oxidation of deposited carbon causes the cell potential. The OCV for undiluted n-decane between 700 and 800 °C is approximately 1.0 V and thus lower than the predicted Nernst potentials. Considering
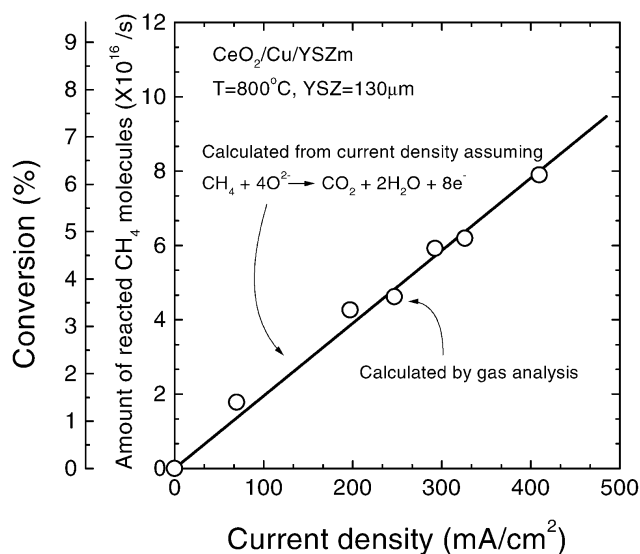
Figure 3.1: The conversion of methane at $1073\,\mathrm{K}$ using a cell with a $Cu/CeO_2/YSZ$ anode and an electrolyte thickness of $130\,\mu\mathrm{m}$. The points (circles) were determined from gas analysis and the line was calculated from the electrical current and the reaction $CH_4 + O^{2-} \rightarrow CO_2 + 2H_2O + 8e^-$ (Source: [41], primary citation [76]).

the significant degradation after $24\,\mathrm{h}$ of operation (see Figure 3.2) associated with the anode pores being filled with tar-like molecules, direct carbon oxidation could be a reason for the difference of the measured OCV and the theoretical Nernst voltage. At the beginning the V-i curve clearly shows polarisation resistance which does not occur when operating this cell with humidified H_2. The carbon deposition is explained by free-radical, gas phase condensation reactions and subsequent formation of high-molecular weight, polyaromatic compounds by pyrolysis. Identical degradation rates for the afore mentioned hydrocarbon fuels indicate that the polyaromatics are formed irrespective of aromatic content in the precursor fuel. Furthermore, temperature programmed oxidation results with H_2O as the oxidant for a ceria free and ceria containing YSZ slab are contrasted to investigate the impact of ceria on the carbon removal rate achieved with steam. The result is that carbon is already removed at $700\,^\circ\mathrm{C}$ with ceria, compared to $900\,^\circ\mathrm{C}$ without ceria.

Operation with benzene in dry diluted hydrogen on Ni-YSZ anodes

Current density effects on the performance of SOFCs exposed to $15\,\mathrm{g/Nm^3}$ benzene in a dry $15\,\%$ H_2/N_2 atmosphere at $765\,^\circ\mathrm{C}$ are investigated by Mermelstein et al. [70]. Benzene is used as a biomass model tar for the tests with Ni-YSZ anodes. V-i
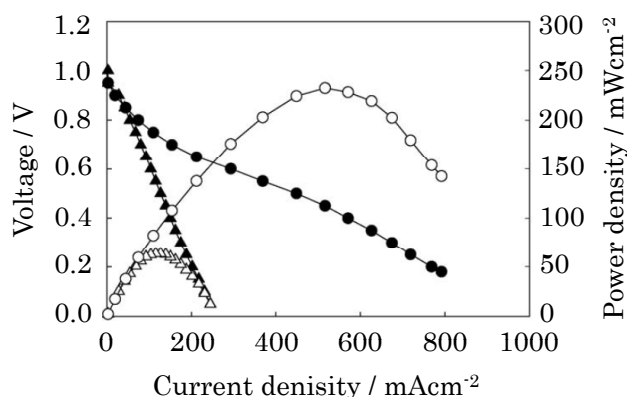
Figure 3.2: Cell potentials (solid symbols) and power densities (open symbols) as a function of current density for cells operating on undiluted n-decane at 1073 K. The data show the initial performance (circles) and the performance after 24 h operation (triangles) (Source: [60]).

curves are shown for initial conditions before exposure to benzene and after 30 min of operation at 0 and 10 mA/cm² current density (see Figure 3.3). While the *OCV* is the same before and after exposure to benzene, the voltage differs significantly at low current densities. The voltage decreases more rapidly after exposure to benzene. However, the voltage is higher after operation at 10 mA/cm² compared to 0 mA/cm² indicating a negative impact on anode kinetics coming from carbon deposition. This negative effect seems to be less strong at 10 mA/cm². Furthermore, a tendency towards the initial value looking at the V-i curves can clearly be observed the higher the current density is. This is explained by the possibility of carbon oxidation during the acquisition of the polarisation curve. Therefore carbon is even seen to act as a fuel for *Ni-YSZ* anodes.

The results of literature show that direct oxidation of hydrocarbons may not be possible for *Ni-YSZ* anodes without risking carbon deposition for dry conditions. However, synthesis gas from a gasifier usually contains significant amounts of water which supports steam reforming rather than direct oxidation. Carbon deposition is obviously less problematic for *Cu*-ceria-*YSZ*. Nevertheless, it is not reported whether direct oxidation of higher hydrocarbons may take place in a similar way as for methane.

3.2 Heterogeneous catalysis on a nickel catalyst

In case a *Ni*-containing anode is used, the possibility of steam reforming is investigated. Nickel for example is a common reforming catalyst in the chemical industry.
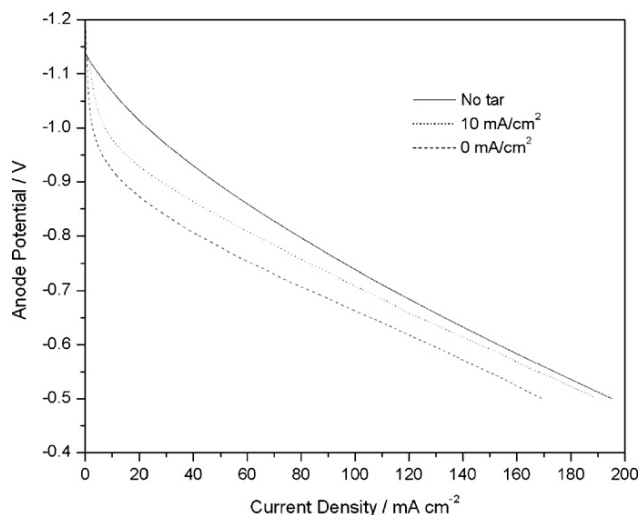
Figure 3.3: Anode potential of SOFC with Ni-YSZ anodes after exposure to $15\,\mathrm{g/m^3}$ benzene tar in a dry $15\,\%$ H_2/N_2 atmosphere at $765\,^{\circ}$C after operating at 0 and $10\,\mathrm{mA/cm^2}$ for $30\,\mathrm{min}$ compared to the initial performance of the cell before tar loading (Source: [70]).

Heterogeneous catalysis with naphthalene, benzene and methane

Heterogeneous catalysis experiments on nickel catalysts with naphthalene, benzene and methane show a temperature depending steam reforming behaviour [54]. Compared to pyrolysis results the conversion temperature for naphthalene is significantly lower and is located between $\approx$600 and $800\,^{\circ}$C by experiments of Jess [54, 55]. The conversion of methane and benzene is observed at even lower temperatures. Mixtures of hydrocarbons illustrate that these species compete for conversion and that naphthalene is the most reactive [28, 54]. In this case methane and benzene are not reformed until the temperature is reached where complete naphthalene conversion takes place.

Reaction mechanism for steam reforming of methane

Xu and Froment [92] postulate a heterogeneous catalysis model for methane steam reforming that suggests the adsorption of methane on the Ni surface, decomposition, surface reaction and desorption of the products from the Ni surface. Products may be H_2 and CO which only then become electrochemically converted. Kinetic inhibition due to the many steps of the reforming reaction can lead to a decreasing reactive surface caused by the adsorption on the Ni particle.
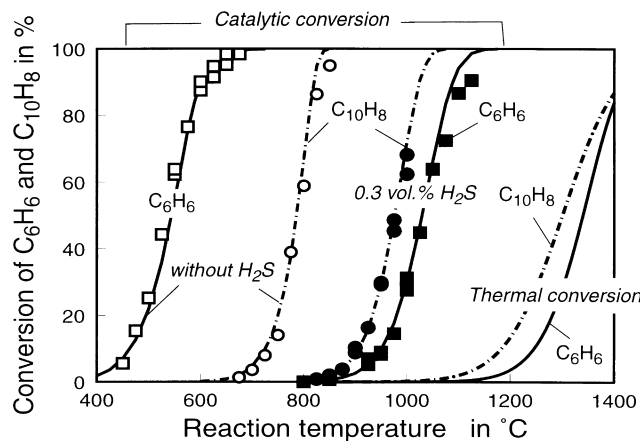
Figure 3.4: Thermal and catalytic conversion of naphthalene and benzene. Residence time with respect to the empty reactor: $0.04\,\text{sec}$ ($1000\,^\circ$C); total pressure: $160\,\text{kPa}$; feed-gas: $25\,\%\ H_2$, $23\,\%\ H_2O$, $0.4\,\%\ C_{10}H_8$, rest N_2; dp: $1.5\,\text{mm}$ (Source: [28]).

Steam reforming of methane, methanol and ethanol on $Ni\text{-}YSZ$ catalyst

Catalytic steam reforming of methane, methanol and ethanol over a $Ni\text{-}YSZ$ catalyst performed between 900 and $1000\,^\circ$C with fuel-to-H_2O ratios from 1:3 to 1:5 are reported from Laosiripojana and Assabumrungrat [65]. The fuel gas enters an annular ceramic reactor where it is conducted over a $Ni/Ce\text{-}ZrO_2$ catalyst prior to the $Ni\text{-}YSZ$ catalyst. The configuration enables the catalyst to work at the same temperature. The $Ni/Ce\text{-}ZrO_2$ catalyst is used to simulate indirect internal reforming for the $Ni\text{-}YSZ$ catalyst. Tests with and without the $Ni/Ce\text{-}ZrO_2$ catalyst illustrate the difference in carbon deposition behaviour on the $Ni\text{-}YSZ$ catalyst for direct and indirect internal reforming. In the case of methane it is clearly shown that for high steam contents the $Ni\text{-}YSZ$ anode can be fed directly without the problem of carbon deposition. A clear tendency to higher H_2 production yields is observed the higher the steam content and the higher the temperature is. Since all the methane is converted for fuel-to-steam ratios as low as 1:3 as well as at $900\,^\circ$C the increasing H_2 production yield at higher steam contents and higher temperature is attributed to the characteristic of the shift reaction. Measurements of CO and CO_2 further confirm this suggestion.

Steam reforming of propane, hexadecane and tetralin on $NiAl_2O_3/Al_2O_3\text{-}YSZ$ catalyst

Steam reforming experiments for propane, hexadecane and tetralin over a $NiAl_2O_3/Al_2O_3\text{-}YSZ$ catalyst are reported by Fauteux-Lefebvre [35]. Hexadecane and tetralin reform-

ing is performed to test the catalyst with paraffinic and aromatic compounds. The reactants mixed in a H_2O/C ratio between 2.3 and 3 are fed to the reactor at 630-750 °C. An increase of the GHSV as well as a decrease of the reaction temperature shows reduced yield rates for H_2, indicating an impact to the conversion for hexadecane. Similarly stable exit gas compositions are achieved for steam reforming of tetralin at 705 °C. In both cases the test duration is between 4 and 5 hours. No significant catalyst deactivation is observed. Furthermore, carbon deposition is detected in only a few experiments. Comparisons of the equilibrium and measured gas concentrations at the exit of the reactor are conform.

3.3 Reforming of methane

The following sections examine to what extend reforming of hydrocarbons occurs on a Ni containing anode. First the behaviour of methane conversion is looked at for steam and CO_2 reforming. Afterwards steam reforming of tar and other higher hydrocarbons is focused on.

Modelling of steam reforming of methane on a SOFC anode

A model of a methane fueled SOFC is deployed by Klein et al. [61] to compare direct and gradual internal reforming. At low inlet H_2O/CH_4 ratios the steam for the reforming reaction comes from the electrochemical oxidation of H_2 which is called gradual internal reforming (GIR). Simulations with high H_2O/CH_4 ratios are attributed to direct internal reforming (DIR). In this model the steam reforming reaction is assumed to take place on the nickel catalyst of the Ni-YSZ anode. Further, the produced CO is said to react in the water gas shift reaction wherever the gas is present, either in the gas channel or in the pores. Only H_2 is considered for electrochemical oxidation. Carbon deposition, due to the Boudouard or cracking reaction, is not regarded in the model. Depending on the inlet H_2O/CH_4 ratio the reforming reaction is faster for DIR compared to GIR. For both modes it is observed that the reforming kinetics are high at the anode inlet and quickly become slower along the cell because of the depletion of methane. The water gas shift reaction, on the other hand is really close to equilibrium.

Steam reforming of methane on tubular SOFC anode

Experimental data on the steam reforming behaviour of methane in a thin-walled extruded zirconia tubular SOFC reactor is reported for methane-to-steam ratios between 5:1 and 15:1 by Finnerty and Ormerod [36]. In particular the conversion rate for methane over a 50 vol% and 90 vol% nickel cermet anode indicates a significant temperature dependency for the tested temperature interval between 1023 and 1173 K. It

is not reported whether the conversion rate is based on reforming only, or on carbon deposition as well. However, TPO measurements indicate the occurrence of two types of carbon species. At $1023\,\text{K}$ both anodes show conversion rates around $31\,\%$ whereas at $1173\,\text{K}$ the $90\,\text{vol}\%$ nickel cermet anode leads to significant higher values, up to $49.2\,\%$. Varying the methane-to-steam ratio between 5:1 and 15:1 indicates a reduced conversion rate at higher ratios for both anodes. This is mainly explained by different formations of carbon species. These results suggest a far too high methane-to-steam ratio for the operation of SOFCs.

CO_2 **reforming of methane on a** Ni-YSZ **anode**

Further experiments investigate the possibility of CO_2 reforming of methane. Three different mixtures (50%/50%, 64%/36% and 37%/63%) of CH_4/CO_2 are tested over a Ni-YSZ anode by Goula et al. [44] at 700-900 °C. A peak of the CH_4-consumption rate is observed at equimolar compositions. The products from CO_2 reforming being H_2 and CO are supposed to add to the total electrochemical potential and are shown by an increased cell voltage at closed circuit conditions (see Figure 3.5). Interestingly this voltage increase coming from CO_2 reforming is not observable at open circuit conditions. However, a competitive adsorption of CH_4 and CO_2 on the Ni surface is suggested. SEM micro graphs show no carbon deposition which is attributed to the possibility of carbon oxidation through oxygen ions coming from the cathode during closed circuit conditions.

CO_2 **reforming of methane on a** $Ni(Au)$-GDC **anode**

Furthermore, Yentekakis [93], in a similar experiment for a $Ni(Au)$-GDC anode, achieved a peak of the CH_4 consumption rate at an equimolar CH_4/CO_2 ratio under open circuit conditions. Coinciding maxima of the production of H_2 and CO establish the expectation that mainly dry reforming occurs. Nevertheless, a blackening of the anode due to a very thin layer of carbon deposited is visible. A degradation of cell performance at alternating closed- and open circuit conditions could not be noticed after $220\,\text{h}$. Linear V-i curves suggest no mutual interference of the dry reforming reaction and the electrochemical oxidation of H_2 and CO. Therefore, dry reforming of methane with CO_2 might be an option for very low steam contents.

CO_2 **reforming of benzene on a** Ni/YSZ **and** Ni/CGO **anode**

The impact of CO_2 reforming on a Ni/YSZ and Ni/CGO anode for a synthesis gas containing $15\,\%$ H_2 and $15\,\text{g/m}^3$ benzene is shown by Mermelstein [68] for an operating temperature of 765 °C. The CO_2 content changes from 10 to $50\,\%$. Carbon formation apparently decreases with increasing CO_2 concentration at dry conditions. An inverse behaviour is achieved for similar tests with $5\,\%$ steam.
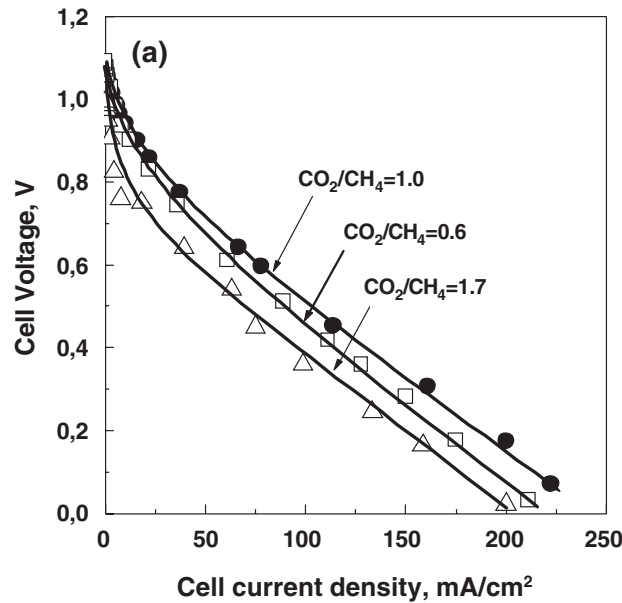
Figure 3.5: Current–voltage behaviour of the biogas fueled fuel cell under equimolar: 50 % CO_2/50 % CH_4, rich-quality: 36 % CO_2/64 % CH_4 and poor-quality: 63 % CO_2/37 % CH_4 biogas feed. Total flow rate: 60 cm³/min (Source: [44]).

Impact of steam and current density on steam reforming of methane on a Ni-YSZ anode

Impedance response at open circuit in order to detect carbon deposition from a methane fueled Ni-YSZ anode is taken to compare the impact of current density and the presence of steam at 750 °C by Koh et al. [63]. Dry and humidified methane in nitrogen is tested at open and closed circuit conditions. From equilibrium calculations a current density of 200 mA/cm² is determined to avoid carbon deposition thermodynamically. Looking at the impedance spectra over time for humidified methane/nitrogen operation shows a steady increase of the anode reaction resistance (see Figure 3.6). *"It seems to take about an hour to saturate the catalytic sites for carbon deposition in our test cell, as the size of arc is almost unchanged after 60 min"* [63]. Running the cell alternately at 200/0/200 mA/cm² shows the reversibility of the carbon deposition. The polarisation resistance after 90 min, at open circuit, is significantly higher compared to the initial spectra at 200 mA/cm². Operating the cell further at 200 mA/cm² for 100 min results in a similar polarisation resistance as at the beginning of the experiment, indicating carbon removal. Apart from the impedance spectra the V-i curves are recorded after each modification of the load (200/0/200 mA/cm²). However, in this case the interpretation of the measured V-i curves do not allow any assumption about carbon deposition since the characteristics of all three curves are almost identical. Another experiment shows irreversible carbon deposition for dry methane operation. Based on

these results Koh et al. postulate that *"It is likely that the reversible carbon deposition occurs at or near three-phase boundaries while the irreversible carbon deposition occurs mostly on Ni surface and/or in case excess methane exists"*.
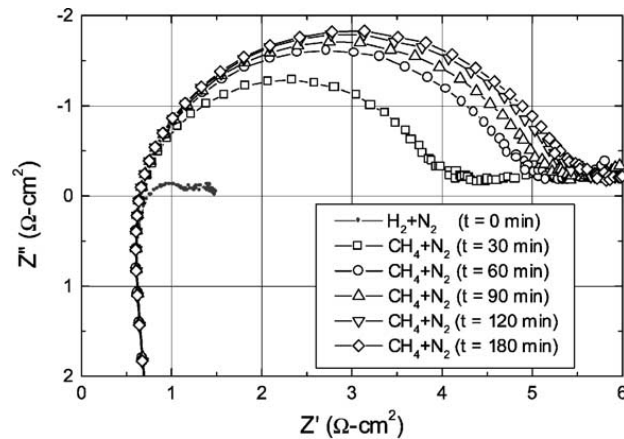
Figure 3.6: Change of impedance spectra with methane as fuel at open circuit condition (Source: [63]).

3.4 Reforming of tar

This section will examine whether the characteristics of methane reforming can be applied to tar as well. The same result as described in Section 3.2 for tar reforming can be expected for nickel anodes even though the catalyst material from heterogeneous catalysis experiments has more favorable properties compared to an SOFC anode in terms of heterogeneous surface reactions.

Steam reforming of methane, naphthalene, phenol and toluene on a Ni-YSZ anode

The results by Frank [38] provide a good comparability showing experiments with methane, naphthalene, phenol and toluene over a Ni-GDC anode between 650 and 850 °C. The conversion rate is illustrated by measuring the open circuit voltage for separate hydrocarbons and mixtures of them. Combinations of naphthalene, toluene and methane in a biogenous gas mixture resulted in an inhibited conversion of methane and toluene in the presence of naphthalene.

Steam reforming of benzene on a Ni-YSZ and a Ni-CGO anode

The effect of steam on the reforming of benzene is illustrated for a Ni-YSZ and a Ni-CGO anode in a study by Mermelstein et al. [70]. A gas composition of $15\,\text{g/Nm}^3$ benzene in a $15\,\%$ H_2/N_2 atmosphere is used at an operating temperature of $765\,^\circ\text{C}$. The steam-to-carbon ratio is varied between 1 and 3 and accounts for 2.5, 5 and $7.5\,\%$ of the anode gas. The negative impact to anode kinetics as described by Mermelstein and treated in Section 3.1 is still visible for the Ni-YSZ anode at low current densities indicating carbon formation even at $S/C{=}3$. However, this negative effect seems to be reduced at higher S/C-ratios. Similar tests with a Ni-CGO anode provide an enhanced performance. The V-i curves, after $30\,\text{min}$ of operation, are located even slightly above the initial V-i curve. Since the V-i curves after $30\,\text{min}$ of operation are taken immediately after benzene is removed from the gas stream, slow desorption of benzene through a reaction with water onto the surface of the nickel until all carbon atoms are converted to CO or CO_2 is considered. *"..., unconverted tar may still have been absorbed on the surface of the anode. The continued reforming of the condensed tar to CO, providing an increase in local fuel concentration, may offer an explanation for the increase in performance"* [70]. This effect is further explained by the OCV when switching back and forth from the tar free to the tar loaded gas composition. An increase of the OCV is clearly detectable when adding benzene, suggesting that the quantities of benzene used in this study act as a fuel to the fuel cell. After removing the benzene from the gas stream the OCV returns back to its initial condition. In another study by Mermelstein et al. [69] toluene and a mixture of benzene/toluene, naphthalene, phenol and pyrene are tested as well as benzene only in dry conditions. The OCV increased from 1.15 to 1.25 V with the addition of each model tar. Several mechanisms leading to the increase of the OCV are given. One of them is the internal catalytic decomposition of the tar into carbon and hydrogen where the increase of partial pressure of hydrogen would cause improved cell potential. Another one in the case of benzene is the direct electrochemical oxidation at the anode which would explain the instantaneous increase of the OCV when tar is introduced. As opposed to the results with benzene described in [70] it is observed *"...that after tar flow had been removed from the system, the OCV still remained above the OCV prior to tar loading"*. In this case the increase of the OCV is attributed to the possibility of electrochemical oxidation of deposited carbon.

Mermelstein et al. [69] postulate weak adsorption of methane and benzene on the surface of the catalyst. Thus no strong competition between these two hydrocarbons, concerning the catalytic conversion, takes place. On the other hand, strongly bound naphthalene condensed on the catalyst reduced the conversion of other tar components eventually leading to a decrease in carbon deposition. Hence, benzene alone is expected to show faster kinetics for carbon deposition compared to a tar mixture that contains naphthalene.

Steam reforming of naphthalene, toluene, phenanthrene and pyrene on a
Ni-CGO **anode**

Ouweltjes [75] tested different tar species such as naphthalene, toluene, phenanthrene and pyrene in synthesis gas at $850\,^{\circ}$C over a Ni-GCO anode. The results show that toluene contributes to the cell potential and thus can be steam reformed. Other species such as naphthalene, pyrene and phenanthrene lower the cell potential and even inhibit the methane conversion. However, this effect is shown to be reversible as soon as the tar addition stops.

Most of the afore mentioned investigations are either heterogeneous catalysis experiments or tests on SOFC anodes at open circuit voltage. In operation, oxygen ions migrate from the cathode to the anode side and interact with the adsorbed fuel components such as H_2 and CO on the catalyst surface [88]. The intention of research so far was to focus on the impact of the current density and the oxygen ion flow, respectively, on carbon deposition. The effect of the drawn current on reforming reactions has not been intensively investigated yet. Since the reforming mechanism occurs on the catalyst surface according to Xu et al. [92] the question whether or not oxygen ions can react with adsorbed hydrocarbons in case of slow reaction kinetic, as it is assumed in the case of naphthalene, needs to be researched further.

3.5 Reforming of higher hydrocarbons

Higher hydrocarbons that are not usually considered as tar are looked at in this section. Nevertheless, some of them have an aromatic structure and thus may have a similar conversion behaviour as typical gasifier tar species.

Catalytic reforming of n-tetradecane, 1-methylnaphthalene and decalin on a
Pt/γ-**Alumina catalyst**

Three approaches - SR, CPOX and OSR - to catalytic reforming of n-tetradecane (paraffin), 1-methylnaphthalene (aromatic) and decalin are reported by Shekhawat et al. [86]. A fixed bed continuous-flow reactor using a Pt/γ-Alumina catalyst is used in this study. One of the aims is to compare the conversion behaviour of the hydrocarbons as well as the product yield, such as H_2, CO and CO_2 for individual hydrocarbons and mixtures. Results from OSR, under identical reforming conditions, show that all three hydrocarbons have higher yields of H_2 and CO the higher the temperature and the lower the space velocity is (see Figure 3.7). CO_2 production, on the other hand, is lower for higher temperatures due to the characteristic of the water gas shift reaction. The tested temperature range is located between 750 and $900\,^{\circ}$C. *"The H_2 production rates at the same conditions decrease in the order: paraffins > naphthenes $\gg$ aromatics."* The products in the gas stream additionally included C_1-C_6
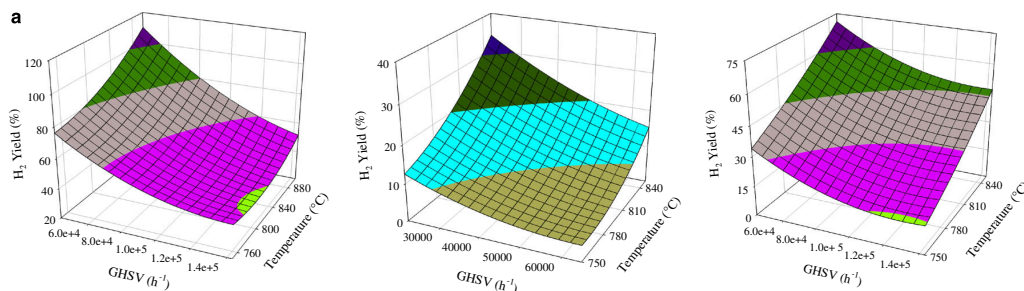
Figure 3.7: Yield of H_2 from oxidative steam reforming of n-tetradecane (left), 1-methylnaphthalene (middle) and decalin (right) (Source: [86]).

n-paraffins, ethylene, propylene, isobutane, n-butane and benzene. Methane, one of the major byproducts is not assumed to be built from the methanation reaction since it is not thermodynamically favorable. Rather α-scission of the hydrocarbons on the metal catalysts is suggested.

Aromatics are said to strongly adsorb to the metal sites. This fact must not necessarily lead to deactivation by carbon deposition but can kinetically inhibit the reforming reactions of other compounds such as paraffins. Experiments with binary and tertiary mixtures underline this theory. The H_2 yield of a mixture of tetradecane and methylnaphthalene during OSR first increases with temperature until reaching a maxima from where the yield rate even decreases with temperature [86]. Interestingly, CPOX is more highly affected by the difference in the reactivity of the fuel components than SR. This is attributed to the abundance of steam for SR. The main statement postulated by Shekhawat et al. [86] is that *"...overall yields from the reforming of a fuel mixture are not additive of yields from individual fuel components, rather the more reactive component is consumed first."*

Catalytic reforming of n-dodecane and tetralin on a $Ni/Ce_{0.75}Zr_{0.25}O_2$ catalyst

Similar behaviour is found for n-dodecane and tetralin by Gould et al. [45]. The substances were tested individually and in a 50/50% mixture in a quartz tube reactor over a $Ni/Ce_{0.75}Zr_{0.25}O_2$ catalyst. The feed stream consists of air, nitrogen, water and the tested hydrocarbon. Autothermal reforming is achieved by varying the oxygen-to-carbon ratio (O/C) between 0.6 and 1.2. The reaction temperature is a result of the feed temperature, which is 550 °C and the exothermic reactions taking place on the catalyst. Depending on the fuel and the O/C ratio the reaction temperature increases to 650 - 950 °C. The conversion rate to CH_4 and CO_x over the O/C ratio for dodecane, tetralin and a 50/50 % mixture shows large differences between the tested components (see Figure 3.8). However, viewing the downstream temperatures give reason to attribute the different conversion rates not only to the molecular structure

40

of the hydrocarbon but rather to the temperature dependent kinetics. A higher conversion for tetralin together with a higher reaction temperature compared to dodecane is observed for the whole O/C range. On the contrary, fairly similar conversion rates around 90 % can be identified when comparing the values for tetralin at a O/C ratio of 0.8 and 1.0 and for dodecane at a O/C ratio of 1.2. In this case the reaction temperature for both species is around 950 °C. The same result is observed for the comparison of tetralin at O/C=0.6 and dodecane at O/C=0.8 leading to a conversion rate of approximately 60 % at 830 °C.

Another finding is that the conversion rate of the 50/50 % mixture is not a linear combination of those of the pure substances but rather close to the behaviour as received from pure tetralin.

A look at the CH_4 yield indicates a very low CH_4 production in all three cases. CH_4 for tetralin is below the accurate detection threshold of the instrument. This result appears consistent since tetralin has a high degree of unsaturation compared to dodecane. Samples of liquid condensate from autothermal reforming of tetralin contain mainly tetralin, along with small quantities of naphthalene, indene, 2-methylindene and 1,2-dihydro-naphthalene. The majority in the liquid samples, after autothermal reforming of dodecane, is unconverted dodecane. Futhermore, 4-dodecene, 1-undecene and oxygenated compounds like tetrahydro-2-isopentyl-5-propyl furan are present.
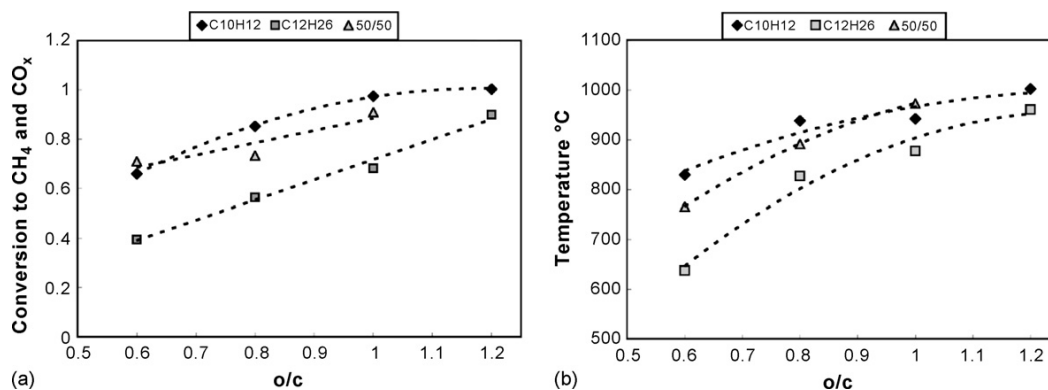
Figure 3.8: Dodecane, tetralin and 50/50 % mixture conversion (left) and downstream temperature (right): feed temperature = 550 °C, $H_2O/C = 2.0$, $O/C = 0.6$-1.2, GHSV= 225000 ^{1}/$_h$ ±10 % (Source: [45]).

Operation of tubular SOFC with dry trimethylpentane, methanol, ethanol, formic acid and octanol

A study by Saunders et al. [82] focusing on carbon deposition reports about the operation of a micro tubular SOFC with blended dry fuel containing trimethylpentane,

ethanol and octanol at 0.5 V and 1023 K. Using ethanol and octanol individually causes deactivation of the cell within 60 minutes while the mixture of both shows a fairly stable current signal. Further individual tests with a variety of hydrocarbons indicate fast cell degradation except for methanol and formic acid. The outlet concentrations show yields of H_2, CO and CO_2. CH_4 is only produced at low temperature ranges. For example the use of methanol leads to a significant portion of CH_4 between 300 and 700 °C.

3.6 Summary

With respect to the wet gas composition of synthesis gas from biomass gasification ($\approx$ 10-50 vol.%) steam reforming of hydrocarbons on a Ni containing anode seems to be suitable. The afore mentioned results from literature show that the conversion of hydrocarbons by steam reforming on Ni containing anodes is generally possible. If the hydrocarbons are converted they will contribute to the electrochemical cell potential due to an increase of the partial pressure of hydrogen and carbon monoxide which influences the Nernst voltage. No results have been reported yet about the exact extend of the contribution to the cell potential caused by hydrocarbons. However, obviously there must be a correlation between the contribution to the cell potential and the hydrocarbon concentration.

Wood gas contains a variety of other hydrocarbons besides methane. In this context it has been explained that the total conversion rate of multiple hydrocarbons may not correspond to the individual conversion rate. Therefore a significant task will be to investigate whether this competing conversion behaviour can be observed by the cell potential as well.

Furthermore, it will be investigated whether the current density during operation has an influence on steam reforming of tar species.

Considering these points it is decided to use a commercial Ni-GDC anode for the experimental investigation shown in Chapter 6.

Chapter 4

Theoretical fundamentals

The theoretical fundamentals are explained in the following sections. Figure 4.1 indicates the topics along the reaction pathway of the synthetic synthesis gas at the SOFC anode. An outline of what the typical tar formation in wood gas looks like and how representative tar species are added to the synthetic synthesis gas (Section 4.1 and 4.2) is first looked at. The next step implies the equilibrium gas composition at the anode surface (Section 4.3) which is the basis for the calculation of the Nernst voltage (Section 4.4). Since equilibrium may not be achieved especially for the operation with tar an investigation of the kinetic inhibition of the catalytic surface reactions is illustrated in Section 4.5.

4.1 Nature and formation of hydrocarbons from biomass gasification

This work focuses on higher hydrocarbons which emerge during the gasification of biomass. These higher hydrocarbons develop in the pyrolysis step of the gasification process and are commonly called "tar". Pyrolysis is the heating-up of biomass without oxidants and happens prior to the gasification step. Therefore, depending on the pyrolysis temperature (240-600 °C) low- and high-molecular hydrocarbons are formed by the depolymerisation of the biomass lignin structure. At high temperatures ($\approx$ 600 °C) the volatile hydrocarbons may polymerise to high molecular hydrocarbons. Based on the stage of the pyrolysis process Milne and Evans [71] distinguish the formation between primary, secondary and tertiary tar. The molecular structure of these hydrocarbons can be aliphatic or aromatic. Some hydrocarbons such as phenol are classified into primary and secondary tar. A comprehensive description about the formation and conversion of biomass gasifier tar can be found in [71]. Table 4.1 lists exemplarily up various tar species.

Looking at Table 4.1 the variety of hydrocarbons in wood gas becomes apparent. Consequently, these hydrocarbons come along with different physical (melting and boiling point) and chemical properties (binding energy) due to their diverse molecular structure. This is a very important fact considering the application of wood gas in
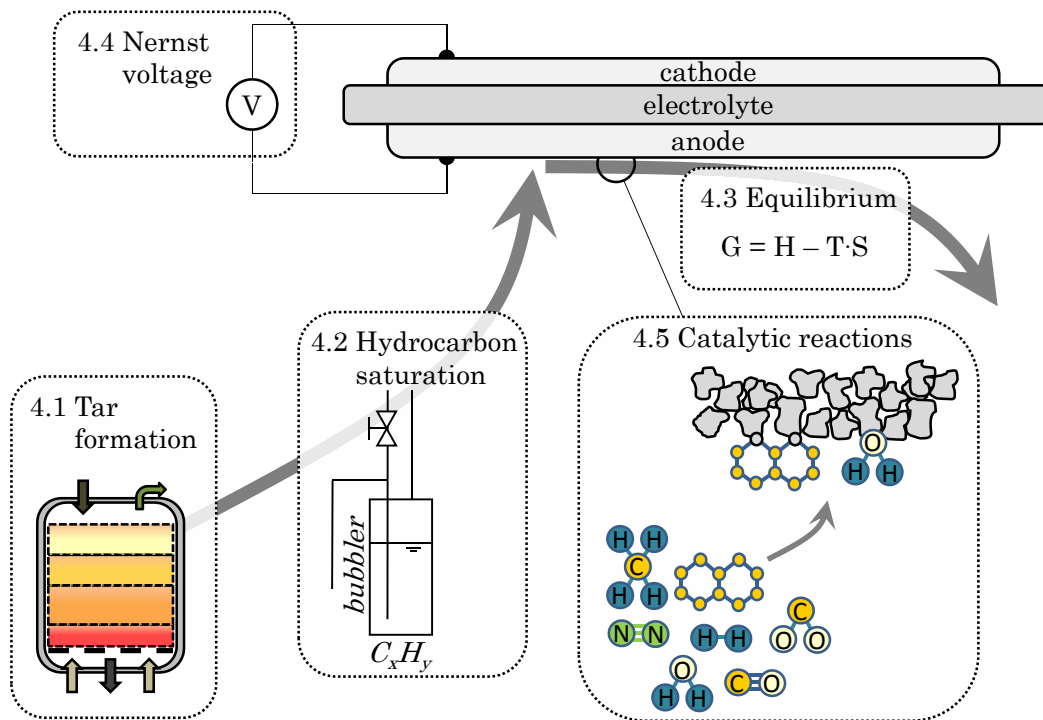
Figure 4.1: Chapter overview about the theory.

downstream processes. For instance, the dew point of high molecular hydrocarbons may lead to condensation and blocking of pipes if a certain process temperature is undershot. Regarding this work the chemical behaviour during the heterogeneous catalysis process on the SOFC anode is important to understand. Especially the complex steam reforming mechanism may differ significantly for each hydrocarbon.

Another important parameter, the concentration of each hydrocarbon species, depends on the gasification technology which can be roughly divided into four groups: fixed bed gasifiers, fluidised bed gasifiers, entrained flow gasifier and multi-zone gasifier [83]. Fixed bed gasifiers are further divided in updraft- and downdraft gasifiers. Furthermore, the fluidised bed gasifiers may have either a bubbling or circulating bed. Comprehensive descriptions of these technologies can be found in [56]. A detailed description of these technologies is not intended in this work as only the concentration of the hydrocarbons in the respective wood gas is a significant boundary condition for the development of the measuring principle. A comparison of the total tar concentration of the most common gasifier technologies is shown in Table 4.2 based on a summarising overview of Milne and Evans [71].

Table 4.2 elucidates a significant difference in the total amount of tar which may

Table 4.1: Examples of tar species present in wood gas (molecular structures are found in the appendix)

Pyrolysis stage	Hydrocarbon	Structure	Formula
Primary	pyridine	heterocyclic, 1-ring	C_5H_5N
	furan	heterocyclic, 1-ring	C_4H_4O
	indene	aromatic, 2-ring	C_9H_8
	thiophene	heterocyclic, 1-ring	C_4H_4S
	phenol	aromatic, 1-ring	C_6H_6O
Secondary	benzene	aromatic, 1-ring	C_6H_6
	phenol	aromatic, 1-ring	C_6H_6O
	toluene	aromatic, 1-ring	C_7H_8
	cresol	aromatic, 1-ring	C_7H_8O
	styrene	aromatic, 1-ring	C_8H_8
	xylene	aromatic, 1-ring	C_8H_{10}
Tertiary	naphtalene	aromatic, 2-ring	C_8H_{10}
	phenanthrene	aromatic, 3-ring	$C_{14}H_{10}$
	anthracene	aromatic, 3-ring	$C_{14}H_{10}$
	pyrene	aromatic, 4-ring	$C_{16}H_{10}$

Table 4.2: Tar emission of several types of gasifiers (Source: [83], primary citation [71])

Gasifier type	Tar load [g/Nm³]		
	Min	Max	Mean
Down-draft	0.04	6	0.1-1.2
Up-draft	1	150	20-100
Fluidised bed, bubbling	<0.1	23	1-15
Fluidised bed, circulating	<1	30	1-15

be present in wood gas depending on the gasifier technology. Here, the measuring principle is considered to be used for wood gas of an allothermal steam gasifier with a bubbling fluidised bed. For this type of gasifier Kienberger [58] measures mainly phenol, naphthalene and derivatives of naphthalene (1-methylnaphthalene, 2-methylnaphthalene) as well as cresols. Aromates including three and more rings such as fluorene, acenaphthene and acenaphthylene are only found in small amounts. Table 4.3 shows the result of an SPA-sample for a typical operating point.

Due to the large variety of tar species it is not possible to test more species within a reasonable time in the experiments explained in Chapter 6. Testing a mixture of all tar species is not useful since the observed results can neither be attributed

Table 4.3: Tar species and tar load of wood gas from a bubbling allothermal steam fluidised bed gasifier (compare [58])

Tar species	Tar load [mg/Nm³]	Tar load [ppm]	Category
phenol	1466	349	prim./sec.
naphthalene	831	145	tertiary
m-cresol	495	103	secondary
p-cresol	395	82	secondary
2-methylnaphthalene	356	56	secondary
o-cresol	266	55	secondary
Σ xylenes	266	56	secondary
indene	204	39	secondary
1-methylnaphthalene	188	30	secondary
acenaphthene	107	16	tertiary
acenaphthylene	91	13	tertiary
biphenyl	60	9	secondary
fluorene	24	3	tertiary
Σ unknown	1269	*364*[1]	-
Total SPA-tar	6018	*1725*[1]	-

[1]Volumetric concentration is given in benzene equivalent

specifically to the total concentration of the tested species nor to the presence of a specific single species. For the experiments in Chapter 6 naphthalene (tertiary tar), toluene and xylene (both secondary tar) are used to represent typical tar species from different pyrolysis stages of wood gas. Table 4.3 shows the tar composition of a bubbling allothermal steam fluidised bed gasifier. The main components are phenol and naphthalene. Phenol is not used in the experiments because it is toxic. Instead of phenol, toluene and xylene are picked since it is expected that they have a similar conversion behaviour to phenol regarding the steam reforming reaction. Steam reforming results of Frank [38] at a SOFC anode show generally a similar conversion behaviour. For example, phenol and toluene are already converted completely above 750 K. Moreover, phenol as well as toluene and xylene has a single aromatic ring. Toluene and xylene contain one and two methyl-groups respectively which is the main difference to phenol that only contains one hydroxy-group. The value of the binding energy of an aromatic C-bond is between those of a single C-bond (C-C) and double C-bond (C=C). Therefore, the binding energy of the aromatic ring is higher than for the hydroxy group (C-O) or the methyl-group (C-C) bindings (see Table 4.4). Therefore the fragmentation of the aromatic ring rather than the hydroxy or methyl group is assumed to be the rate limiting parameter.

The heat-of-adsorption is assumed to be another rate limiting property for heteroge-

Table 4.4: Mean binding energy for polyatomic molecules in gaseous phase (compare [72])

Tar species	Binding energy [kJ/mol]
C-C	347
C=C	619
C-O	335
C-H	414

neous reactions. The heat-of-adsorption depends on the carbon number as described in Figure 4.9. Therefore phenol (C_6), toluene (C_7) and xylene (C_8) may have a similar conversion behaviour when competing against naphthalene (C_{10}). However, this issue is explained in more detail in Section 4.5.

4.2 Gas phase hydrocarbon saturation

In order to test naphthalene, toluene and xylene transported in the synthetic synthesis gas a temperature controlled bubbler is used as shown in Figure 5.1. Nitrogen bubbles through the liquid tar species which eventually evaporates to reach the saturation vapor pressure. The equilibrium between the liquid and gaseous phase of tar above the fluid level inside the bubbler can be described through several equations such as Clausius-Clapeyron, Antoine, Harlacher or Wagner [52]. The desired concentration of tar in the final synthetic synthesis gas determines the required saturation vapor pressure. The saturation vapor pressure is related to a certain temperature which needs to be controlled within the bubbler. To calculate the temperature within the bubbler the following Antoine equation is used,

$$ln(p_{sat}) = A - \frac{B}{C + T} \tag{4.1}$$

where p_{sat} is the saturation vapor pressure and T the related temperature. A, B and C are substance-specific parameters which are usually valid for a certain temperature range. The unit of pressure and temperature determine the magnitude of the parameters A, B and C. In this work the pressure is in *bar* and the temperature in K. These parameters can be found in [73]. Table 4.5 summarises these parameters for typical tar species.

Table 4.5: Antoine parameters for the calculation of the vapor pressure of several hydrocarbons and water obtained from [73]

C_xH_y	A	B	C	Temp. range	Melting point	Boiling point
	[1]	[1]	[1]	[°C]	[°C]	[°C]
naphthalene	4.00000	1832.0000	-61.3290	80 to 179	80.26	218
toluene	4.23680	1426.4480	-45.9570	0 to 24	-95	111
m-xylene	5.09199	1996.5450	-14.7720	0 to 60	-48 to 13.3	138 to 144
phenol	4.24688	1510.0000	-98.9490	107 to 182	41	182
phenantrene	4.51920	2428.4480	-70.9600	100 to 150	98.5	332
pyrene	2.68710	1086.8240	-262.8490	200 to 395	156	394
benzene	4.60362	1701.0000	20.8060	149 to 282	5.5	80.1
water	5.07680	1659.7930	-45.8540	61 to 90	0	100

4.3 Equilibrium gas composition

The calculation of the Nernst voltage of a fuel cell requires the knowledge of the gas concentration above the anode surface. This concentration may differ significantly from the feed gas composition which usually does not correspond to the equilibrium concentration. Especially in the case of the SOFC the high temperature and the catalytic surface shift the gas composition towards the equilibrium. The equilibrium concentration is obtained by minimising the Gibbs enthalpy G of the gas composition [12].

$$G = H - T \cdot S \tag{4.2}$$

where H and S are the enthalpy and entropy of the gas composition and T the temperature at which the equilibrium is considered.

This can be explained in an exemplary way by a single equilibrium reaction such as $H_2 + \frac{1}{2}O_2 \rightleftharpoons H_2O$. First the Gibbs enthalpy of the reactants is determined. Then the Gibbs enthalpy of the products is calculated along the extend of reaction ζ. The reaction is said to be in equilibrium where the Gibbs enthalpy becomes a minimum. At this point the reaction Gibbs enthalpy $\Delta_R G$ is introduced:

$$\Delta_R G = \left(\frac{dG}{d\zeta}\right)_{p,T} = \nu_{H_2O} \cdot \mu_{H_2O} + \nu_{H_2} \cdot \mu_{H_2} + \nu_{O_2} \cdot \mu_{O_2} \tag{4.3}$$

where ν_i is the stoichiometric coefficient of the reactants and products (ν_{H_2}=-1, ν_{O_2}=-$\frac{1}{2}$, ν_{H_2O}=1) and μ the chemical potential. In this case $\Delta_R G$ is the derivative of G with respect to ζ. Furthermore, it can be interpreted as the difference between the chemical potentials μ of the free molar enthalpies between reactants and products of the respective reaction mixture. $\Delta_R G$ equals 0 in the point where G becomes a minimum. This point is called the thermodynamic equilibrium. Using the concentration term $p_i = \frac{p_i}{p_0}$ to describe the activity a_i, $\Delta_R G_{(T,p)}$ can be formulated in the following way:

$$
\begin{aligned}
\Delta_R G_{(T,p)} &= \nu_{H_2O}\left(\mu_{0,H_2O} + R \cdot T \cdot ln\frac{p_{H_2O}}{p_0}\right) + \nu_{H_2}\left(\mu_{0,H_2} + R \cdot T \cdot ln\frac{p_{H_2}}{p_0}\right) \\
&\quad + \nu_{O_2}\left(\mu_{0,O_2} + R \cdot T \cdot ln\frac{p_{O_2}}{p_0}\right) \quad\quad\quad\quad\quad\quad\quad\quad (4.4) \\
&= \Delta_R G^0 + R \cdot T \cdot ln\left[\left(\frac{p_{H_2O}}{p_0}\right)^{\nu_{H_2O}} \cdot \left(\frac{p_{H_2}}{p_0}\right)^{\nu_{H_2}} \cdot \left(\frac{p_{O_2}}{p_0}\right)^{\nu_{O_2}}\right] \quad (4.5) \\
&= \Delta_R G^0 + R \cdot T \cdot ln\,(Q) \quad\quad\quad\quad\quad\quad\quad\quad\quad\quad\quad (4.6)
\end{aligned}
$$

Only in the case of equilibrium the reaction quotient Q is called equilibrium constant K. As mentioned above, $\Delta_R G_{(T,p)} = 0$ in equilibrium. Then, together with the equilibrium constant K it can be written:

$$
0 = \Delta_R G^0 + R \cdot T \cdot lnK \quad\quad\quad\quad\quad\quad\quad\quad\quad (4.7)
$$

where,

$$
K = \left(\frac{p_{H_2O}}{p_0}\right)^{\nu_{H_2O}} \cdot \left(\frac{p_{H_2}}{p_0}\right)^{\nu_{H_2}} \cdot \left(\frac{p_{O_2}}{p_0}\right)^{\nu_{O_2}} \quad\quad\quad (4.8)
$$

$$
K = \prod a_i^{\nu_i} \quad\quad\quad\quad\quad\quad\quad\quad\quad\quad\quad\quad\quad\quad (4.9)
$$

In the case of a multi component mixture such as wood gas, the equilibrium has to be found considering more than one possible reaction. This makes the calculation very comprehensive since the values for enthalpy $H_{(T,p)}$ and entropy $S_{(T,p)}$ have to be known for each component. In this work the software package FactSage is used to calculate the equilibrium concentration. Extensive literature to this topic can be found in numerous textbooks such as [12, 80].

An example demonstrates how the equilibrium concentration diverges from the feed concentration. Typical wood gas compositions and their equilibrium concentrations are listed in Table 4.6. Furthermore, the temperature dependency of the equilibrium in the operation range of an SOFC is illustrated in Figure 4.2. Additionally, it can be predicted when carbon deposition is thermodynamically favorable.

Table 4.6: Examples for wood gas compositions and their equilibrium concentrations (values are in *vol.*%) at $900\,°C$ and $0.99\,$bar (rest is N_2)

Feed gas composition						Equilibrium concentration					
H_2	CO	CO_2	CH_4	H_2O	O_2	H_2	CO	CO_2	CH_4	H_2O	O_2
20.3	13.0	13.0	6.2	28.8	$0.0 \rightarrow$	32.9	18.8	9.9	2.06×10^{-3}	21.8	2.26^2
25.4	7.1	14.2	3.7	32.9	$0.0 \rightarrow$	30.9	13.1	10.2	0.86×10^{-3}	30.2	4.93^2
10.9	7.6	7.6	3.9	45.8	$0.0 \rightarrow$	24.8	8.7	9.7	0.20×10^{-3}	34.8	1.21^2

$^2 \times 10^{-15}$
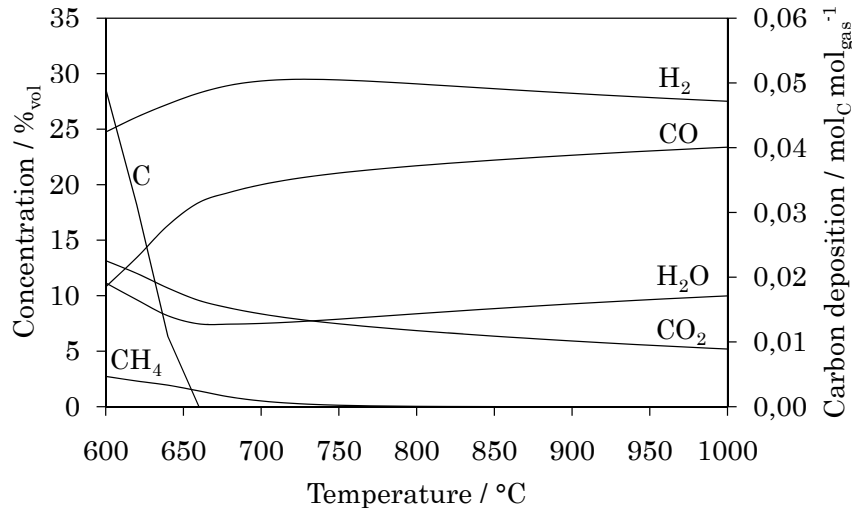
Figure 4.2: Equilibrium concentration depending on temperature for a feed gas composition of $20\,\%\ H_2$, $13\,\%\ CO$, $13\,\%\ CO_2$, $6\,\%\ CH_4$, $10\,\%\ H_2O$ at $0.98\,$bar.

4.4 SOFC Fundamentals

The solid oxide fuel cell is a specific type within the family of fuel cells. There are various parameters, such as operating temperature, membrane assembly, ion conductivity, possible fuel components and cell shape that allow a clear distinction of fuel cell technologies. Table 4.7 shows a comparison of prevailing fuel cell types.

Considering the task to convert higher hydrocarbons in a synthesis gas atmosphere the SOFC remains the only applicable fuel cell type. Most fuel cell types run on pure hydrogen. At low temperatures for example carbon monoxide deactivates the *Pt*-catalyst used in PEMFC anodes. This is one reason for a new trend towards temperatures of about $200\,°C$ for PEMFC. At this temperature the catalyst is less affected by CO.

Table 4.7: Types of fuel cells (compare [33])

Name	Operating temp.	Ion conductivity	Reactant	Electrolyte	Cell shape
PEMFC	$40\text{-}80°C$	H^+	H_2	PSA, PSEPVE [15]	planar
HT-PEMFC	$160\text{-}200°C$	H^+	H_2	PSA, PSEPVE [15]	planar
AFC	$65\text{-}220°C$	OH^-	H_2	Potassium hydroxide	planar
PAFC	$205°C$	H^+	H_2	Phosphoric acid	planar
MCFC	$650°C$	CO_3^-	H_2, CO_2	Li_2CO_3/K_2CO_3, $Li_2CO_3/NaCO_3$	planar
SOFC	$600\text{-}1000°C$	O^{2-}	H_2, CO	YSZ	planar tubular

Table 4.8: Properties of an SOFC

Anode	Nickel + yttria stabilised zirconia ($Ni\text{-}YSZ$), nickel + gadolinium doped ceria ($Ni\text{-}GDC$)
Electrolyte	Yttria stabilised zirconia (YSZ)
Cathode	Lanthan strontium manganate (LSM), lanthanum strontium cobalt ferrite ($LSCF$)
Interconnects	Chromium ferritic stainless steel
Fuel	Hydrogen, carbon monoxide, synthesis gas, reformates of: natural gas, diesel, kerosene, methanol

Another reason for choosing an SOFC is the wide range of operating temperature up to 1000°C in combination with Ni-anodes. This fact makes it a suitable candidate for direct internal steam reforming of hydrocarbons. In this environment the hydrocarbons may be partly or completely converted to H_2 and CO by a subsequent steam reforming and shift reaction. Both molecules can be seen as fuel for the SOFC and therefore will be electrochemically oxidised. The reactions will be explained in more detail in Section 4.5.3. In Table 4.8 some properties of an SOFC are summarised.

4.4.1 Functionality of an SOFC

The operating concept of an SOFC is shown in Figure 4.3. The fuel gas containing H_2 and CO enters the anode chamber. The cathode side is supplied with air or oxygen. As stated in Table 4.8 the anode/electrolyte/cathode assembly consists of various components supporting different tasks. The porous anode is a mixture of Ni and GDC or YSZ. The anode structure must contain enough Ni in order to be sufficiently conductive for electrons. The ratio of Ni to GDC or YSZ where the anode is electrically conductive is determined by the percolation limit. A typical volume ratio of Ni/YSZ is 20-25 %. If the portion of Ni falls below a certain value the electrical conductivity of the anode drops dramatically. Ni is used as a catalyst

for the electrochemical half reaction as shown in Equation 4.11 and 4.12. In this step the electron is released from the fuel component. The released electrons travel via the Ni grains through the anode to the external load and eventually to the cathode. Within the cathode the electrons travel via the LSM or $LSCF$ grains. LSM or $LSCF$ is taken on the cathode side to enable the electrochemical reduction of oxygen (see Equation 4.10). The porous LSM or $LSCF$ structure is conductive for electrons as well as for oxygen ions. YSZ is a gas tight but oxygen ion-conductive material and enables the migration from the cathode side to the anode side by vacancy diffusion. At this point the "triple phase boundary" (TPB) is introduced. The TPB of the porous anode is the line where the fuel gas contacts Ni and YSZ material simultaneously. Theoretically this is the only place where the electrochemical reaction may occur since three requirements have to be fulfilled - the diffusion of the gaseous fuel component that needs to be electrochemically oxidised, the electrical conduction of electrons released by the fuel molecule and eventually the supply of oxygen ions from the cathode. At the TPB the oxygen ion reacts then with the H^+ or CO^+ ion. The products H_2O and CO_2 diffuse back from the anode TPB to the main fuel flow. The respective electrochemical reactions are given below. Similarly a TPB can be introduced at the cathode side where the oxygen reduction takes place.

Cathode:

$$\frac{1}{2}O_2 + 2e^- \rightarrow O^{2-} \tag{4.10}$$

Anode:

$$H_2 \rightarrow 2H^+ + 2e^- \tag{4.11}$$

$$CO \rightarrow CO^{2+} + 2e^- \tag{4.12}$$

$$2H^+ + O^{2-} \rightarrow H_2O \tag{4.13}$$

$$CO^{2+} + O^{2-} \rightarrow CO_2 \tag{4.14}$$

Theoretically the direct oxidation of methane would be possible. However, it is not yet clear whether this reaction occurs in reality on a Ni-YSZ anode when steam is present.

For open circuit conditions where no current is drawn there is neither a conduction of oxygen ions nor of electrons. This means that no electrochemical oxidation of fuel components takes place at the anode side.

Most likely the composition is not in equilibrium when it enters the anode chamber which means that before or parallel to the electrochemical reaction, side reactions such as shift reaction, reforming or carbon deposition may occur. These heterogeneous reactions are not limited to the TPB since they neither require the supply of oxygen

ions nor the possibility to release electrons. These reactions are described in Section 4.5.3.
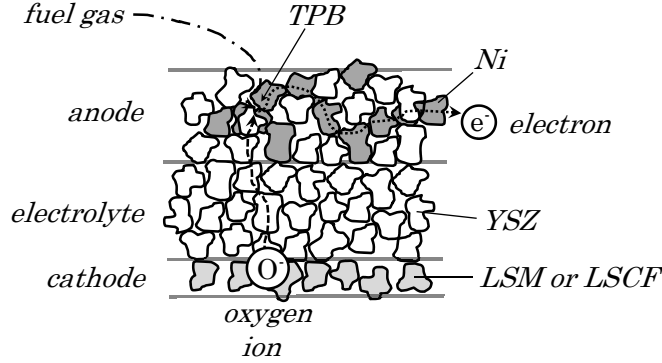

Figure 4.3: Triple phase boundary.

4.4.2 Nernst voltage

The Nernst voltage can be found by using the irreversible work of a fuel cell. The work is achieved due to the electrochemical oxidation reactions of fuel reactants with oxygen ions migrating from the cathode. As mentioned SOFCs can directly process hydrogen and carbon monoxide as shown in Equation 4.11 and 4.12.

The products that emerge on the anode surface dilute the fuel gas mixture. Unavoidable mixing effects of the products along the anode are the reason why a reversible operation of a fuel cell is technically not possible. Therefore the irreversible work W_{irr} depends on the partial pressures of the reactants and products.

$$W_{irr} = \Delta_R G_{(T,p)} = \Delta_R H_{(T,p)} - T \cdot \Delta_R S_{(T,p)} \tag{4.15}$$

For ideal gas, the following formulae are used:

$$\Delta_R H_{(T,p)} = \Delta_R H_{(T)} \tag{4.16}$$

$$\Delta_R S_{(T,p)} = \Delta_R S_{(T)} - R \cdot ln\,(Q) \tag{4.17}$$

$$\Delta_R G_{(T,p)} = \Delta_R G_{(T)} - R \cdot ln\,(Q) \tag{4.18}$$

The pressure dependency of the enthalpy can be neglected. The reaction quotient Q as introduced in Section 4.3 considers the partial pressures of the reactants and products.

With the general equation of the electrical power P of a fuel cell a link between the voltage V and the reaction Gibbs enthalpy $\Delta_R G_{(T,p)}$ can be found.

$$P = V \cdot I = \dot{n}_{fuel} \cdot W = \dot{n}_{fuel} \cdot \Delta_R G_{(T,p)} \tag{4.19}$$

$$V = -\frac{\dot{n}_{fuel} \cdot \Delta_R G_{(T,p)}}{I} = -\frac{\dot{n}_{fuel} \cdot \Delta_R G_{(T,p)}}{\dot{n}_{el} \cdot F} = \frac{\Delta_R G_{(T,p)}}{n^{el} \cdot F} \tag{4.20}$$

The product of the molar flow of electrons $\dot{n}_{el}$ and the Faraday constant F builds the electric current I. The molar flow of the fuel $\dot{n}_{fuel}$ includes the gas components that take part in the oxidation reaction and thus differs from the fuel inlet flow. For the reaction of H_2 or CO the ratio,

$$\frac{\dot{n}_{fuel}}{\dot{n}_{el}} = \frac{1}{n^{el}} = \frac{1}{2} \tag{4.21}$$

can be derived from Equation 4.11 and 4.12.

Eventually the Nernst voltage V_N for an irreversible fuel cell can be formulated by combining Equation 4.18 and 4.20.

$$V_N = -\frac{\Delta_R G_{(T)}}{n^{el} \cdot F} - \frac{R \cdot T \cdot ln\,(Q)}{n^{el} \cdot F} \tag{4.22}$$

This equation as it is found in many textbooks [88] may not be satisfying when it comes to the calculation of the Nernst voltage of a gas mixture that contains not only H_2 but also CO and CH_4. Often the question arises which oxidation reaction has to be taken in order to use the correct $\Delta_R G_{(T)}$ due to the fact that the partial pressures used in the reaction quotient Q are based on the oxidation reaction. In fact, for a gas mixture that is in equilibrium it is regardless whether H_2, CO or even CH_4 is looked at. McIntosh and Gorte [67] and Frank [38] descriptively deduce that eventually the Nernst voltage is driven from the difference of the oxygen partial pressures between cathode and anode, regardless of the oxidation reaction (see Equation 4.26). This seems to be obvious since the driving force for the oxygen ions, to migrate from the cathode to the anode, must be the gradient of the oxygen partial pressure. As shown later, the following equations provide the same Nernst voltage for a gas mixture in equilibrium.

Table 4.9: Parameters for the calculation of the Nernst voltage

$n_{CH_4}^{el} =$	8
$n_{H_2}^{el} =$	2
$n_{CO}^{el} =$	2
$n_{O_2}^{el} =$	4
$R =$	$8.314 \,^{J}/_{mol \cdot K}$
$T =$	$1173.15 \,K$
$F =$	$96485 \,^{C}/_{mol}$
$p_0 =$	$0.99 \,bar$
$x_{O_2} =$	$21 \,vol.\%$
$p_{O_2,air} =$	$0.208 \,bar$
$\Delta_R G_{(900°C,0.99bar),H_2+0.5O_2 \rightarrow H_2O} =$	$-182899 \,^{J}/_{mol}$
$\Delta_R G_{(900°C,0.99bar),CO+0.5O_2 \rightarrow CO_2} =$	$-180680 \,^{J}/_{mol}$
$\Delta_R G_{(900°C,0.99bar),CH_4+2O_2 \rightarrow 2H_2O+CO_2} =$	$-800640 \,^{J}/_{mol}$

$$V_N = -\frac{\Delta_R G_{(T)}}{n_{CH_4}^{el} \cdot F} - \frac{R \cdot T}{n^{el} \cdot F} ln \left(\frac{p_{CO_2} \cdot p_{H_2O}^2}{p_{CH_4} \cdot p_{O_2,cathode}^2} \right) \tag{4.23}$$

$$V_N = -\frac{\Delta_R G_{(T)}}{n_{H_2}^{el} \cdot F} - \frac{R \cdot T}{n^{el} \cdot F} ln \left(\frac{p_{H_2O} \cdot p_0^{\frac{1}{2}}}{p_{H_2} \cdot p_{O_2,cathode}^{\frac{1}{2}}} \right) \tag{4.24}$$

$$V_N = -\frac{\Delta_R G_{(T)}}{n_{CO}^{el} \cdot F} - \frac{R \cdot T}{n^{el} \cdot F} ln \left(\frac{p_{CO_2} \cdot p_0^{\frac{1}{2}}}{p_{CO} \cdot p_{O_2,cathode}^{\frac{1}{2}}} \right) \tag{4.25}$$

$$V_N = \frac{R \cdot T}{n_{O_2}^{el} \cdot F} ln \left(\frac{p_{O_2,cathode}}{p_{O_2,anode}} \right) \tag{4.26}$$

The equations are illustrated by following calculations. For the calculation the first equilibrium gas mixture of Table 4.6 at $900\,°C$ and $0.99\,bar$ is taken. The rest of the parameters are given in Table 4.9.

Using the parameters of Table 4.6 and 4.9 shows that the Nernst voltage is the same regardless of the oxidation reaction taken into account (see Equation 4.27-4.30).

$$V_N = -\frac{(-800640)}{8 \cdot 96485} - \frac{8.314 \cdot 1173.15}{8 \cdot 96485} \cdot ln\left(\frac{0.098 \cdot 0.216^2}{2.04 \times 10^{-5} \cdot 0.208^2}\right) \quad = 0.929V \quad (4.27)$$

$$V_N = -\frac{(-182899)}{2 \cdot 96485} - \frac{8.314 \cdot 1173.15}{2 \cdot 96485} \cdot ln\left(\frac{0.216 \cdot 0.99^{\frac{1}{2}}}{0.326 \cdot 0.208^{\frac{1}{2}}}\right) \quad = 0.929V \quad (4.28)$$

$$V_N = -\frac{(-180680)}{2 \cdot 96485} - \frac{8.314 \cdot 1173.15}{2 \cdot 96485} \cdot ln\left(\frac{0.098 \cdot 0.99^{\frac{1}{2}}}{0.186 \cdot 0.208^{\frac{1}{2}}}\right) \quad = 0.929V \quad (4.29)$$

$$V_N = \frac{8.314 \cdot 1173.15}{4 \cdot 96485} \cdot ln\left(\frac{0.208}{2.24 \times 10^{-17}}\right) \quad = 0.929V \quad (4.30)$$

With Equation 4.26 a very simple formula is introduced where the oxygen partial pressure is the only unknown. Hence, it is shown that the equilibrium gas concentration at the anode has to be determined first in order to find the Nernst voltage.

Hydrocarbons such as naphthalene shift the equilibrium concentration of the synthesis gas and thus change the Nernst voltage. Due to the high temperature and the catalytic anode surface it is likely that equilibrium is partly reached or almost completely. Figure 4.4 demonstrates the correlation between the oxygen partial pressure and the Nernst voltage in dependence of the naphthalene concentration. The same feed gas mixture as listed in Table 4.6 is used. The additional naphthalene load is balanced with N_2. According to Equation 4.26 a lower $p_{O_2,anode}$ causes a higher Nernst voltage. Moreover, the equilibrium and therefore $p_{O_2,anode}$ changes significantly with increasing naphthalene concentration. An explicit voltage increase is observed. This clear correlation between naphthalene concentration and voltage increase is the foundation of the measurement principle developed in this work.

However, these considerations are a theoretical approach. In reality the higher hydrocarbons may not reach equilibrium. Part of it may pass the anode without reaction and stay inert, similar to N_2. The behaviour of the hydrocarbons is diverse due to complex reaction mechanisms. A major part of this work deals with the conversion behaviour of various hydrocarbons such as naphthalene, toluene and xylene. The aim is to investigate a correlation of this behaviour and express it by simple equilibrium considerations.
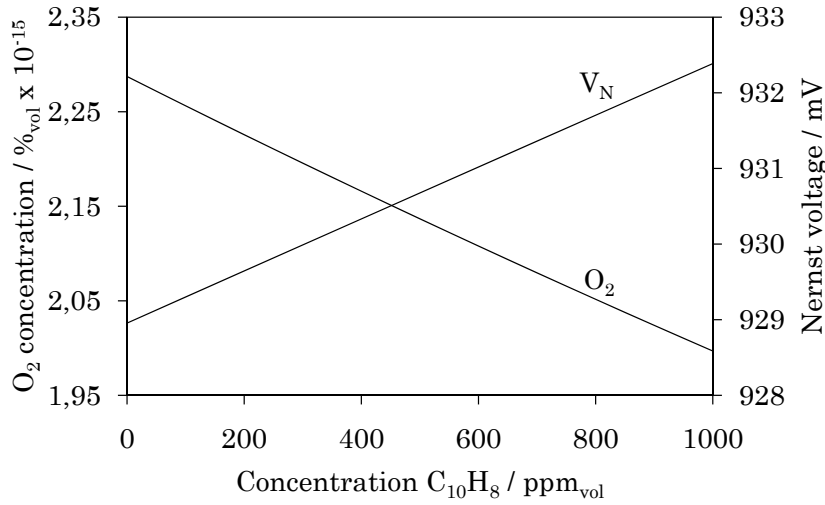
Figure 4.4: Equilibrium oxygen concentration and Nernst voltage depending on naphthalene concentration for a feed gas composition of 20.3 % H_2, 13.0 % CO, 13.0 % CO_2, 6.2 % CH_4, 28.8 % H_2O and 0-1000 ppm $C_{10}H_8$ at 900 °C and 0.98 bar.

4.4.3 Nernst voltage in operation

Under electrical load oxygen ions migrate from the cathode to the anode. Therefore, $p_{O_2,anode}$ increases with the increase of current that is drawn. According to Equation 4.26 this directly affects the Nernst voltage. One can see that the Nernst voltage becomes 0 when $p_{O_2,anode} = p_{O_2,cathode}$. The amount of oxygen ions migrating from the cathode to the anode is directly proportional to the electrical current.

$$\dot{n}_{O_2} = \frac{I}{4 \cdot F} \tag{4.31}$$

The oxygen coming from the cathode can be seen as an additional gas component that is given to the anode gas concentration. This way the new equilibrium concentration under electrical load can be calculated. Figure 4.5 demonstrates how the Nernst voltage decreases with increasing current density. Moreover, it can be seen that with the addition of naphthalene it comes to a higher current density before the Nernst voltage drops to 0. This effect is discussed in more detail by Hauth et al. in [48].

It must be emphasised that the Nernst voltage under electrical load is not the cell voltage as it appears in a real fuel cell. Rather it can be seen as the maximum Nernst potential from the thermodynamic point of view. However, during the operation of a
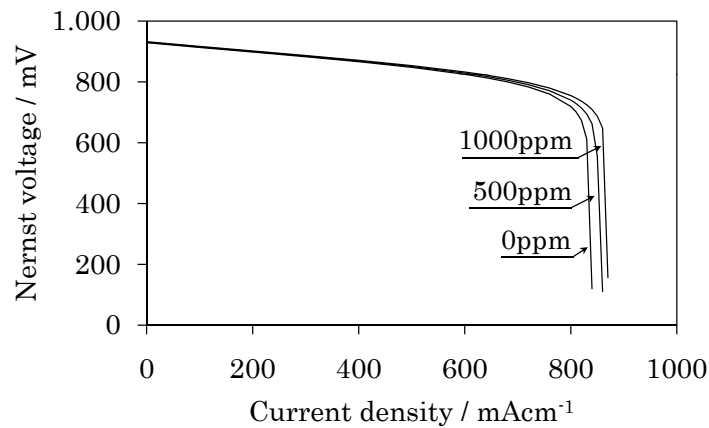
Figure 4.5: Nernst voltage under electrical load for a feed gas composition of 20.3 % H_2, 13.0 % CO, 13.0 % CO_2, 6.2 % CH_4, 28.8 % H_2O and 0/500/1000 ppm $C_{10}H_8$ at 900 °C, 0.98 bar and a feed flow of 1000 $^{\text{Nml}}/_{\text{min}}$.

fuel cell three polarisation effects occur, which diminish the Nernst voltage. A classical V-i curve as can be found in many textbooks is shown in Figure 4.6.

Activation polarisation: The activation polarisation emerges due to the kinetics of the electrochemical reaction at the electrode. The electron transfer from the molecule to the solid electrode represents a barrier that depends on the activation energy. However, at SOFC operating temperatures (800-900 °C) this effect can be neglected. For this reason the V-i curve of an SOFC does not follow the classical V-i curve at low current densities as illustrated in Figure 4.6 or as obtained from PEM fuel cells.

Ohmic polarisation: Resistance of the oxygen ion conduction in the electrolyte accounts in a large part to the ohmic polarisation. The structure of the ceramic electrolyte material is strongly temperature dependent and is cubic above 2377 °C for ZrO_2. Below this temperature the structure is tetragonal and cubic [84]. A cubic structure is necessary for ion conduction [85]. Mixing 8 mol.% Y_2O_3 to YSZ enables a cubic crystal structure of ZrO_2 and thus ion conductivity down to 700 °C. The ionic resistance is therefore reverse to the electrical resistance, which increases with increasing temperature. Additionally, the electrical resistances in the anode and cathode material, the interconnectors and whatever conductor is used in the system have to be considered. However, in single cell tests the voltage measurement is carried out directly at the anode and cathode respectively. Therefore, mainly ionic resistance accounts to the ohmic polarisation that is observed from a V-i curve.

Concentration polarisation: At very high current densities the diffusion of the reactants from the core flow to the triple phase boundary at the electrode surface is too slow. In the same way more products emerge and need to be transported
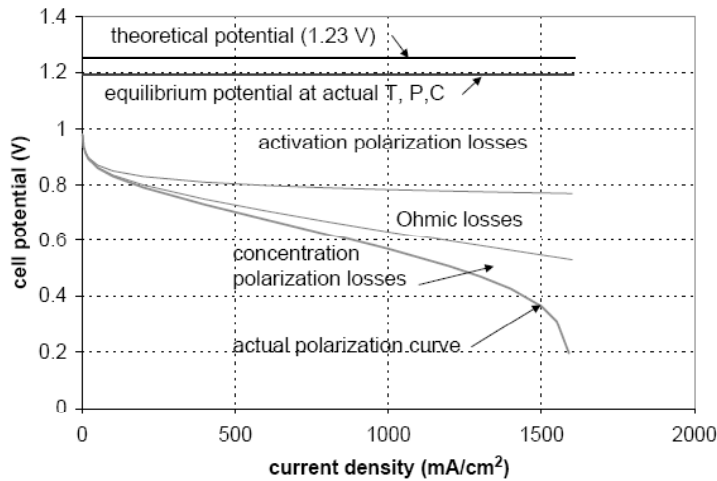
Figure 4.6: Typical V-i curve (Source: [15]).

back to the core flow. If the supply of fuel components such as hydrogen or carbon monoxide stagnates, the oxygen partial pressure increases since no reactant is available. According to equation 4.26 this inevitably causes the Nernst voltage to decrease.

These polarisation effects can be taken to explain degradation effects which are the reason for the cell voltage to decrease over time. Carbon deposition, for example, blocks the porous structure and deteriorates the diffusion of the gas molecules. Additionally, solid carbon covers the anode surface and becomes dissolved in nickel particles. First this minimises the active sites on the nickel catalyst surface. As time progresses, dissolved carbon can burst the anode structure. The electrical connection between the nickel particles in the anode structure becomes worse and results in an increase of the ohmic resistance. However, degradation is not focused at in this work.

4.5 Catalytic reactions

Langmuir proved that heterogeneous catalysed gas/solid phase reactions take place on the catalyst surface. By enabling reaction pathways with lower activation energies the catalyst increases the reaction rate. Another property of a catalyst is that the active sites where the reaction occurs turn back to their original state after each reaction cycle. The equilibrium based on thermodynamics is not influenced by a catalyst whereas the reaction kinetics are significantly dependent on the catalytic properties. A catalytic reaction consists of several steps. One of these steps is the adsorption and desorption of reactants and products.

4.5.1 Competing adsorption of hydrocarbons on catalytic surfaces

Adsorption and desorption are two of the main steps besides gas diffusion and chemical reaction that determine the reaction rate in heterogeneous catalysis. Two types of adsorption have to be distinguished in heterogeneous catalysis - physisorption and chemisorption. Physisorption is caused by van der Waals forces and are not based on electron transfer. The physisorption can take place on all solids even at low temperatures. The reaction rate is usually fast and goes along with low activation energy and a low heat-of-adsorption. Chemisorption is more important for heterogeneous catalysis reactions. In this case chemical bonding between the catalyst material and the reagent is the essential phenomenon. These surface bonds are significantly more reactive compared to free adsorbed molecules from physisorption. Chemisorption has a higher activation energy as well as higher heat-of-adsorption [47]. *"The activation energy represents the barrier that a system must pass on its way from the reactant to the product state"* [27]. A strong temperature dependency of chemisorption is the reason for faster reaction rates at high temperatures. Another crucial characteristic is that chemisorption builds mono layers. Obviously the catalyst has to be in direct contact with the reagent in order to promote the reaction. This is how the impact of the surface can be explained. Whereas for physisorption the magnitude of the surface area is important chemisorption is highly selective with regard to the material and structure. Active sites presumably caused through free atomicities or electron defects due to structural defects (e.g. an edge atom) support the dissociation of the chemical bonds to enable consecutive reactions [47]. This theory is controversially treated in [27] and is based on studies that show that: *"...the regular structural elements of a surface typically account for most of the catalytic activity and that surface defects play a role only under specific conditions."*

Adsorption isotherms help to understand the behaviour of gas molecules when they impinge upon the surface of a catalyst. They are used to illustrate the amount of gas that is adsorbed on a surface when it is in equilibrium depending on the pressure and considering constant temperature. The adsorption isotherms are based on following assumptions: the adsorbed molecules build a localised mono layer; there are no interactions between adsorbed molecules; the solid surface is energetically homogeneous and the heat-of-adsorption does not depend on the surface coverage. Figure 4.7 shows different adsorption isotherms classified by Brunauer. Experiments demonstrate an increasing amount of adsorbed gas molecules on a solid surface with an increase in total pressure. Type I of Figure 4.7 is the classical Langmuir-isotherm according to the empiric equation 4.32:

$$c_A = \frac{a \cdot b \cdot p_A}{(1 + b \cdot p_A)} \tag{4.32}$$

where c_A is the concentration of the adsorbed gas and p_A is the total pressure (a and

b are empirical constants). For a simple reaction $A + F \rightleftharpoons AF$ where the molecule A adsorbs on a free surface spot F Langmuir introduced the surface coverage:

$$\Theta_A = \frac{K_A \cdot p_A}{1 + K_A \cdot p_A} \tag{4.33}$$

where K_A is the equilibrium constant for the surface reaction. Langmuir assumes an energetically homogeneous surface and consequently a heat-of-adsorption that does not depend on the surface coverage. However, in reality the heat-of-adsorption depends, among others, on the surface coverage, surface structure and interactions between adsorbed molecules.
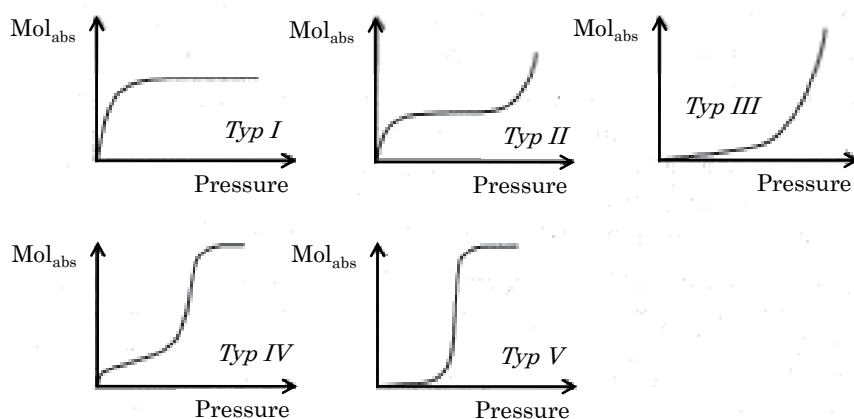

Figure 4.7: Adsorption isotherms (Source: [57]).

Ihm et al. [53] and Gottfried et al. [43] for instance determined the heat-of-adsorption depending on the surface coverage on a single $Pt(111)$ crystal using single crystal adsorption calorimetry.

A molecular beam generates a pulsed flux of benzene that amounts to 7 % of a fully covered mono layer of the crystal. The sticking probability is measured with a quadrupole mass spectrometer in order to determine how much of the beam contributes to the heat-of-adsorption. The sticking probability is close to 1 and starts to fall at 90 % of the amount of the mono layer down to 0 at 100 %. Figure 4.8 compares the measured heat-of-adsorption for benzene (left) and naphthalene (right) at 300 K. Each point is the result of a single gas pulse. The heat-of-adsorption is calculated by dividing the measured calorimetric heat by the number of moles that stick on the surface. This number of moles is equal to the flux of the gas pulse times pulse duration times sticking probability. Then the term $\frac{1}{2}RT^2$ is added to obtain the heat-of-adsorption [53].
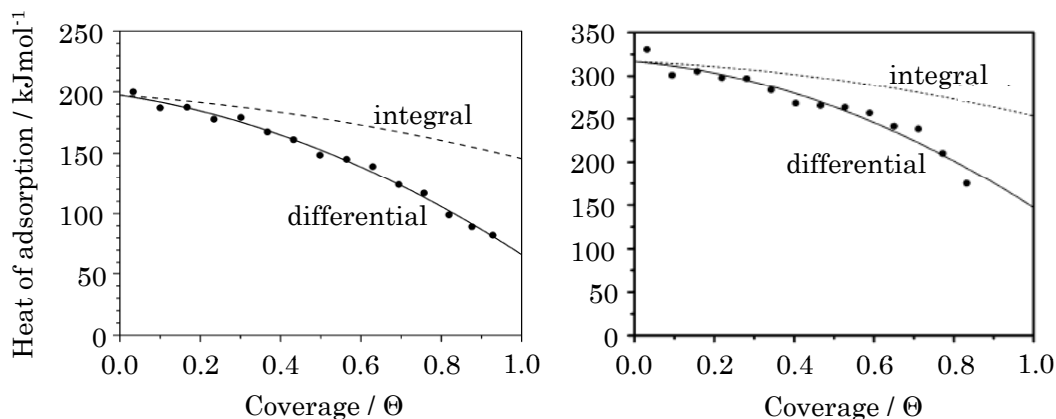
Figure 4.8: Measured differential heat-of-adsorption of benzene (left, Source: [53]) and naphthalene (right, Source: [43]) as a function of coverage on $Pt(111)$ at 300 K. The integral heat-of-adsorption computed using the polynomial of the differential curve (solid line) is shown as the dashed curve.

The results presented in Figure 4.8 reveal a higher heat-of-adsorption of naphthalene compared to benzene at a specific coverage. Gottfried et al. [43] finds a linear correlation when drawing the experimentally gained heat-of-adsorption over the number of C-atoms per molecule for benzene, naphthalene and anthracene (see Figure 4.9 left).

A similar trend is reported from Corma and Ortega [26] for cracking of 1-octene, decalin, tetralin and n-hexadecane at 673 and 773 K on a zeolitic catalyst (see Figure 4.9, right). They tried to derive a correlation for the conversion rate and the catalyst decay based on adsorption effects. Therefore the theoretical conversion model based on Langmuir-Hinshelwood adsorption is used to show adsorption effects of reactants and products. Table 4.10 lists the experimentally gained kinetic parameters for the reaction model.

K_r, K_A, $K_{p_i n_i}$ and K_d are the constants for the reaction rate, reactant adsorption, product adsorption and catalyst decay rate. Furthermore, the heat-of-adsorption is derived from the calculated reactant adsorption constant. The apparent activation energy is obtained by subtracting the heat-of-adsorption from the true activation energy [27]. Eventually the conversion rate for the four substances is given. Based on the conversion rate a reactivity ranking, in the following order, can be observed: 1-octene > decalin > tetralin which corresponds to the true activation energy [26].

When comparing the heats-of-adsorption of these hydrocarbons with those from n-paraffins (see Figure 4.9, right) with the same number of carbon atoms one can see that the heat-of-adsorption is significantly higher for molecules that have double bonds. The heat-of-adsorption depends on the number of carbon atoms as well as on the
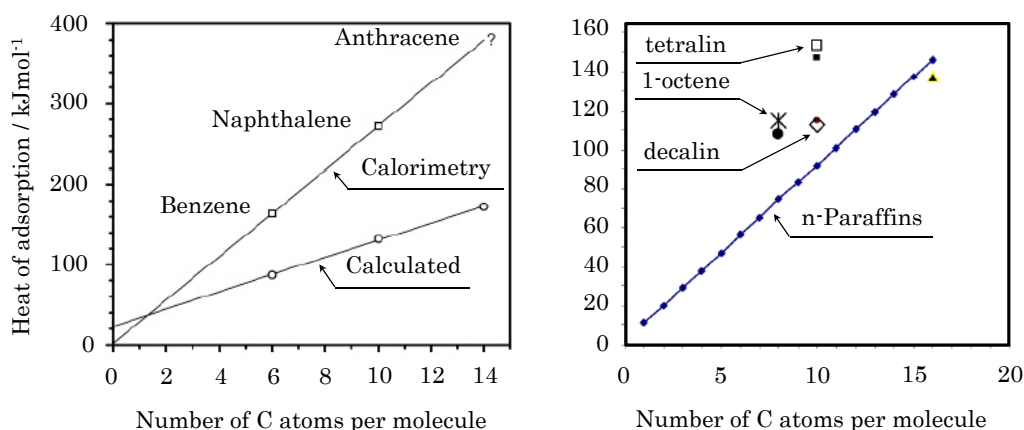
Figure 4.9: heat-of-adsorption of hydrocarbons depending on the number of carbon atoms. Left: Comparison of the experimental integral heats-of-adsorption of benzene and naphthalene on $Pt(111)$ (squares) and the computational results (circles) at the same coverages (Source: [43]). Right: Heats-of-adsorption derived from a kinetic model fed with experimental data (Source: [26]).

number of carbon bonds. For instance the heat-of-adsorption of decalin ($C_{10}H_{18} \rightarrow$ 11 aromatic C-C bonds) is rather close to the one of n-dodecane ($C_{12}H_{26} \rightarrow$ 11 C-C bonds) than the one of n-decane ($C_{10}H_{18} \rightarrow$ 9 C-C bonds). 1-octene ($C_8H_{16} \rightarrow$ 6 C-C bonds, 1 C=C bond) has a clearly higher heat-of-adsorption than n-octane ($C_8H_{18} \rightarrow$ 7 C-C bonds). Tetralin ($C_{10}H_{12}$, aromatic with conjugated C=C bonds), for example, has an even slightly higher heat-of-adsorption than n-hexadecane ($C_{16}H_{34} \rightarrow$ 15 C-C bonds).

In Table 4.10 a higher heat-of-adsorption of the products due to their aromatic rings are taken to explain a higher catalyst decay caused by the strong competition for adsorption which results in a reduction of the active sites [26]. This way catalyst deactivation is not only explained by coke deposition and pore plugging but is also attributed to the adsorbed products. For example the conversion drop observed for 1-octene is low even though high yields of coke are obtained whereas tetralin leads to high catalyst decay and low coke yields. This effect is attributed to the reaction products of tetralin such as di-aromatic naphthalene, methyl naphthalene and heavier aromatics which strongly compete for adsorption and thus reduce the active sites on the catalyst.

The experiments with a fresh catalyst, a coked and afterwards stripped catalyst and a coked unstripped catalyst demonstrate that the activity of the unstripped catalyst is only about 18.4 % compared to 91.4 % of the fresh and 85.6 % of the stripped catalyst

Table 4.10: Kinetic parameters according to the Langmuir-Hinshelwood model (compare [26])

	ΣK_r [$^1\!/\mathrm{s}$]	K_A [$^l\!/\mathrm{mol}$]	$\Sigma K_{p_i n_i}$ [$^l\!/\mathrm{mol}$]	K_d [$^1\!/\mathrm{s}$]	Ads. heat [$^{kJ}\!/\mathrm{mol}$]	App. activ. energy [$^{kJ}\!/\mathrm{mol}$]	True activ. energy [$^{kJ}\!/\mathrm{mol}$]	Conv. rate[3] [wt.%]
Temp.	673 K							
n-Hexad.	8.6	2.31	51	2.200	-137.6	211.7	349.3	-
Decalin	3.69	1.48	13.6	0.081	-112.9	206.0	318.9	19
Tetralin	0.577	7.15	40	1.610	-153.1	204.3	357.4	1
1-Octene	117.3	0.36	12.93	0.010	-115.0	141.9	256.9	92
Temp.	773 K							
n-Hexad.	1147	0.096	16	2.100	-137.6	211.7	349.3	-
Decalin	431	0.109	190	0.144	-112.9	206.0	318.9	42
Tetralin	64.84	0.208	170	0.690	-153.1	204.3	357.4	9
1-Octene	3118	0.025	0.928	0.005	-115.0	141.9	256.9	100

[3] Conversion rate based on TON=12 sec and a conversion feed flow of 3 $^g\!/\mathrm{min}$

respectively [26]. The stripping step is performed with pure N_2 in order to desorb the adsorbed products after the reaction step. In this way it is demonstrated that the adsorbed hydrocarbons at the coked unstripped catalyst obviously deactivate the catalyst significantly.

Furthermore, the temperature dependency of the adsorption can be seen in Table 4.10. The conversion rate increases with temperature and the adsorption constants for the reactant and products decrease. Therefore the catalyst decay decreases as well with increasing temperature. Furthermore the coke yield decreases significantly for all four tested hydrocarbons.

4.5.2 Characteristics of reaction mechanisms on catalytic surfaces

The reaction mechanism of heterogeneous catalytic gas reaction can be very complex and takes place in many steps. After the molecule adsorbs on the catalytic surface it can react with adjacent adsorbed molecules. The adsorbed molecule either dissociates first or reacts in its entirety with other reactants. To gain a basic perception of the reaction sequence two mechanisms have been developed, the Langmuir-Hinshelwood and the Eley-Rideal mechanism. Both mechanisms have great relevance in many industrial processes.

Langmuir-Hinshelwood mechanism

This mechanism is based on the assumption that both reactants are adsorbed on free spots on the catalyst surface without being dissociated. Then the actual surface reaction between the chemisorbed reactants takes place. The adsorbed product eventually desorbs in the final step of the mechanism.

$A_g \rightleftharpoons A^*$ and $B_g \rightleftharpoons B^*$
$A^* + B^* \rightleftharpoons C^*$
$C^* \rightleftharpoons C_g$
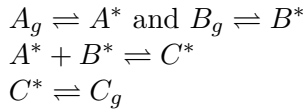
Based on the relations of mixed adsorption following equation for the reaction rate can be postualted:

$$r_{eff} = \frac{dp_C}{dt} = k \cdot \Theta_A \cdot \Theta_B = \frac{k \cdot K_A \cdot p_A \cdot K_B \cdot p_B}{(1 + K_A \cdot p_A + K_B \cdot p_B)^2} \qquad (4.34)$$

The trend of the reaction rate is explained by varying the partial pressure p_A while keeping p_B constant. For a very low p_A the reaction rate is proportional to p_A: $r_{eff} \approx \acute{k} \cdot p_A$ (see Figure 4.10, left). The reaction rate comes to a maximum when the coverage $\Theta_A = \Theta_B$ or in other words when the products $K_A \cdot p_A = K_B \cdot p_B$. If p_A is further increased the reaction rate becomes $r_{eff} \approx \frac{1}{p_A}$.
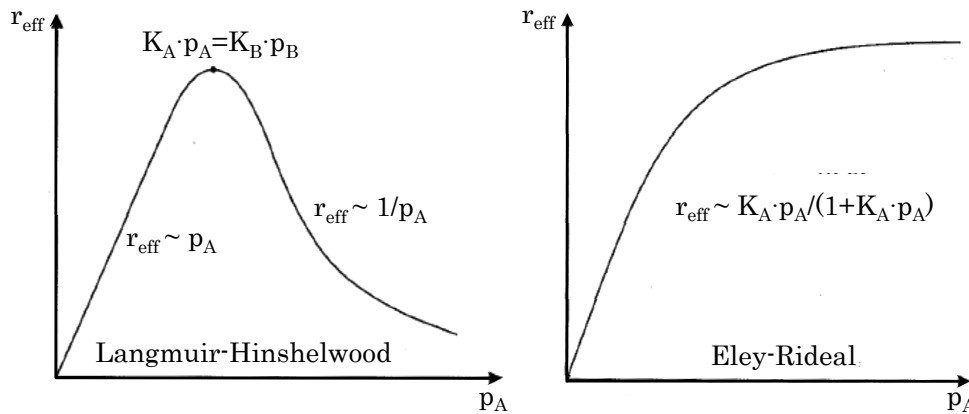

Figure 4.10: Reaction rate of Langmuir-Hinshelwood (left) and Eley-Rideal (right) mechanism (Source: [47]).

65

Eley-Rideal mechanism

In this model only reactant A is assumed to be chemisorbed on the catalyst surface. Reactant B then directly reacts with the activated reactant A without adsorbing to build the product C. The product is still adsorbed after the reaction step before it desorbs. The mechanism is described below:

$$A_g \rightleftharpoons A^*$$
$$A^* + B_g \rightleftharpoons C^*$$
$$C^* \rightleftharpoons C_g$$
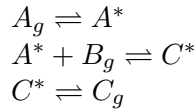
In this case only the coverage of A is important. Derived from the Langmuir-isotherm following rate expression can be found:

$$r_{eff} = k \cdot \Theta_A \cdot p_B = k \cdot \frac{K_A \cdot p_A}{(1 + K_A \cdot p_A)} \cdot p_B \qquad (4.35)$$

Again steadily increasing the partial pressure p_A while keeping p_B constant leads to the curve shown in Figure 4.10 (right). The curve follows the Langmuir-isotherm and nearly becomes constant for a high partial pressure p_A.
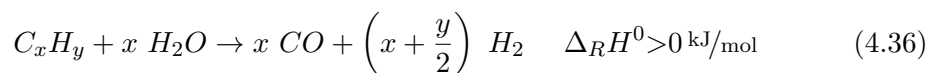
These two mechanisms, the Langmuir-Hinshelwood and the Eley-Rideal mechanism, are fairly straightforward. In fact numerous other mechanisms exist which are described in literature. The knowledge of the exact mechanism is the major requirement to find an accurate correlation between the reaction rate and its influencing parameters [47]. Finding out the mechanism is usually a very difficult task due to the complex measurement techniques necessary. However, these aspects should help to understand the conversion behaviour of the hydrocarbons on an SOFC anode.

4.5.3 Catalytic conversion of hydrocarbons and its impact on the Nernst voltage

As mentioned shortly in Section 4.4.1 reactions such as reforming, shift reaction or carbon deposition may occur in parallel or subsequently to the electrochemical reactions when wood gas is used as fuel. This is enabled by the Ni catalyst in the anode structure. Ni is a common and good catalyst material especially for steam reforming and shift reaction [81]. However, the Ni grains in the anode as well as the geometry of the anode itself are not manufactured to promote heterogeneous catalytic reactions in the first place. This property can rather be seen as a positive side effect in terms of converting fuels with hydrocarbons fuels. Therefore the active Ni surface may be very small compared to special reforming-catalyst pellets. Moreover, the residence

time of the gas components may differ significantly to what is usually achieved in real catalysts. The global reactions of the two main heterogeneous reactions on an SOFC anode are

steam reforming of hydrocarbons:

$$C_xH_y + x\ H_2O \rightarrow x\ CO + \left(x + \frac{y}{2}\right)\ H_2 \quad \Delta_R H^0 > 0\,\text{kJ/mol} \tag{4.36}$$

and water gas shift reaction:

$$CO + H_2O \rightarrow CO_2 + H_2 \quad \Delta_R H^0 = -41.2\,\text{kJ/mol} \tag{4.37}$$
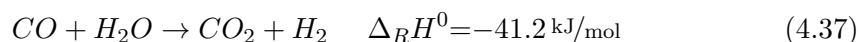
The reaction mechanism for hydrocarbons is usually very complex and is explained by Xu and Froment [92] for steam reforming of methane and the water gas shift reaction. They postulate a heterogeneous catalysis model for methane steam reforming that suggests the adsorption of methane on the Ni surface, decomposition, surface reaction and desorption of the products from the Ni surface.

Products are H_2 and CO which then may be converted electrochemically or react according to the water gas shift reaction. Kinetic inhibition due to the many steps of the reforming reaction can lead to a decreasing reactive surface caused by the adsorption on the Ni particle as described in Section 4.5.2. The kinetic inhibition may be even worse for aromatic hydrocarbons. Establishing a heterogeneous catalysis model to calculate the exact amounts of reformed hydrocarbons is difficult, especially for the situation where more than one hydrocarbon is present at the anode. In this work equilibrium considerations are used to estimate the gas composition based on the conversion rate of the hydrocarbons.

For high H_2O contents (as in the experiments described here) where carbon deposition is thermodynamically not predicted a sequence of the reforming reaction followed by the shift reaction is assumed. In order to define the reforming rate one would have to look at the conversion of the hydrocarbon to H_2 and CO only. The following shift reaction does not allow an isolated observation of the reforming rate using H_2 and CO gas analysis at the anode outlet. The appearance of CO_2 at the anode outlet for example suggests further conversion of CO using H_2O after the reforming step. Therefore, the concentration of the hydrocarbon at the anode outlet is measured by the means of an FID and compared with the anode inlet. Assuming carbon deposition does not occur, the consumption of the hydrocarbon should correlate to the amount that is being reformed. Because of the change of H_2 and H_2O along the reaction affecting the FID signal due to cross-sensitivity effects (see Section 5.3.2), the outlet concentration of H_2O would have to be known in order to calculate the real hydrocarbon load. However, the failure is minor and thus H_2O measurements at the outlet are not carried out. For this purpose the conversion rate CR of hydrocarbons is introduced:

$$CR = \frac{x_{C_xH_y,inlet} - x_{C_xH_y,outlet}}{x_{C_xH_y,inlet}} \qquad (4.38)$$

where $x_{C_xH_y,inlet}$ and $x_{C_xH_y,outlet}$ are the concentrations of the hydrocarbon at the in- and outlet of the anode chamber. CR is estimated and the feed composition of the equilibrium calculation is adapted accordingly. For example, assuming a CR of 90 % for an inlet gas composition containing 1000 ppm C_xH_y leads to a feed gas composition for the equilibrium calculation of 900 ppm. In order to leave the rest of the composition unchanged the missing 100 ppm are balanced with N_2. This way it is possible to estimate the influence of the kinetic inhibition of the reforming reaction on the Nernst voltage. A further explanation can be found in Section 6.1. Figure 4.11 shows the calculated Nernst voltage based on measured conversion rates by Frank [38].
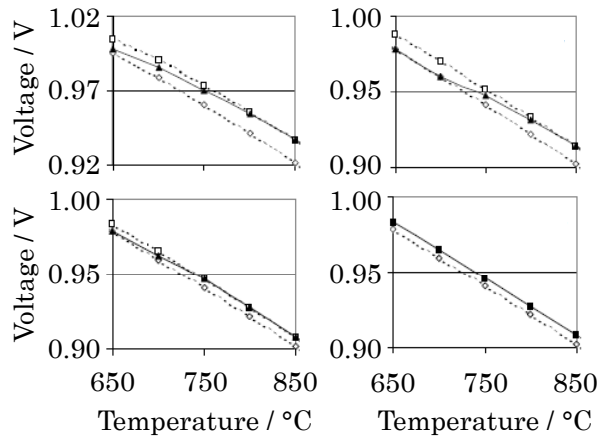

Figure 4.11: Theoretical Nernst voltage for 13 % CO, 13 % CO_2, 21 % H_2, 40 % H_2O with additions of either 3 % methane (top left), 4000 ppm toluene (top right), 2500 ppm phenol (bottom right) or 1500 ppm naphthalene (bottom left), rest N_2. Upper dashed curve = equilibrium of hydrocarbons at all temperatures; Lower dashed curve = no reforming of hydrocarbons; black curve = temperature dependent reforming (Source: [38]).

CR is strongly temperature dependent and may be between 0 and 100 % in a certain temperature range. Frank clearly shows this effect by measuring the Nernst voltage between 650 and 850 °C for operation with synthesis gas containing either toluene or naphthalene. In both cases the Nernst voltage and the conversion rate respectively follow the theoretical trend shown in Figure 4.11. This conversion rate is further supported by gas analysis.

Chapter 5

Test Set-up

5.1 SOFC test rig

The dry synthesis gas consisting of H_2, CO, CH_4, CO_2 and N_2 is mixed using five mass flow controllers to simulate wood gas from biomass gasification. The scheme of the test rig is shown in Figure 5.1. The gas mixture then becomes humidified by means of a water bubbler which is temperature controlled and monitored by a humidity sensor at the outlet of the humidifier. The whole tubing is trace heated to avoid condensation of steam or any tar species and is kept at $150\,^{\circ}$C. Due to the capability of CO_2 absorption in water, CO_2 is bypassed at the humidifier.

For the operation with tar an additional N_2 stream flows through temperature controlled tar bubblers. Up to three tar bubblers can be used which allows the addition of three different tar species simultaneously. N_2 is supposed to be saturated according to the vapor pressure of the respective tar (see Section 4.2). The concentration of tar is varied individually by either changing the N_2 flow through the respective tar bubbler using a mass flow controller or adapting the temperature of the tar bubbler. N_2 for the tar bubblers is branched after the mass flow controller of the main N_2 inlet in order to achieve constant N_2 concentrations in the final gas mixture while varying the N_2 flow through the tar bubblers. The saturated $N_2/\Sigma C_x H_y$ mixture is then conflated with the humidified synthesis gas. To enable a constant humidifier temperature and thus a better comparability the N_2 flows through the tar bubblers are bypassed during tests without tar. With this concept the main synthesis gas flow through the water humidifier is similar for operation with and without tar.

The tar loaded synthesis gas is then directed through stainless steel pipes at $150\,^{\circ}$C to an oven containing the ceramic cell housing (see Figure 5.2). Before the gas enters the anode chamber it is heated up in a ceramic tube and reaches operation temperature. For the cathode supply dry synthetic air ($20\,\text{vol.}\%O_2/80\,\text{vol.}\%N_2$) is provided.

The concentration of the permanent gases before and after the cell are measured with a gas analyser (GA). For determining the hydrocarbon concentration it can be switched to a flame ionisation detector (FID). The 3-way valve in Figure 5.1 enables to switch the measuring point of the gas analysis between cell in- and outlet. For standby

operation a failsafe forming gas (FG, $5\,\mathrm{vol.\%}$ H_2/$95\,\mathrm{vol.\%}$ N_2) line is installed. In case of a malfunction of the SOFC test rig the FG will be turned on automatically. The set-up of the test rig is described in more detail in [66, 91].
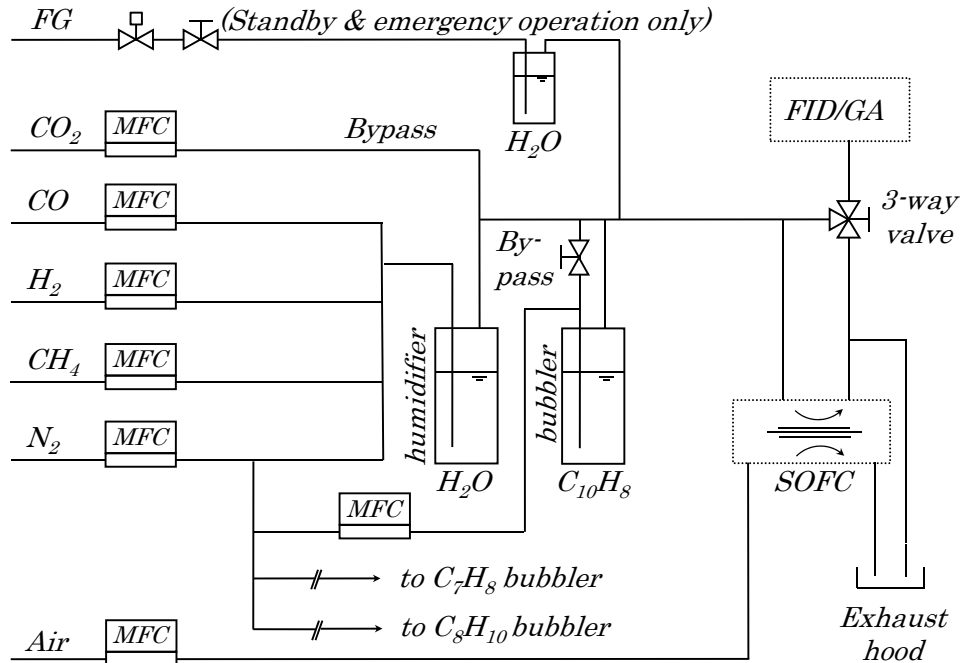
Figure 5.1: Scheme of the SOFC test rig.

5.1.1 Ceramic cell housing for planar cell

The single cell housing in Figure 5.2 consists of Al_2O_3 and carries a commercial planar $10\mathrm{x}10\,\mathrm{cm}^2$ $Ni\text{-}GDC/YSZ/LSM$ electrolyte supported cell. The porous NiO/GDC anode layer is 30 - 50 µm thick. The electrolyte layer consists of $8\,\mathrm{mol\%}$ Y_2O_3 doped ZrO_2 and has a thickness of 80 - 110 µm. On the cathode side two porous layers are used. The layer touching the electrolyte consists of $8\,\mathrm{mol\%}$ doped ZrO_2 mixed with LSM followed by a pure LSM layer. Gas sealing is achieved using planar surfaces between the electrolyte and the ceramic frames of the housing. A weight of approximately $15\,\mathrm{kg}$ is applied on top of the ceramic housing.

Current collection is attained by positioning the coarse nickel mesh, the fine nickel mesh, the nickel foam and the anode side of the cell on top of each other. In the same way the coarse platinum mesh, the fine platinum mesh, the cathode paste and

Top flow field

Air distribution frame

Ceramic frame
Pt current collector
(coarse grid, fine grid)
Ceramic frame
SOFC
Ceramic frame
Ni current collector
(coarse grid, fine grid, foam)
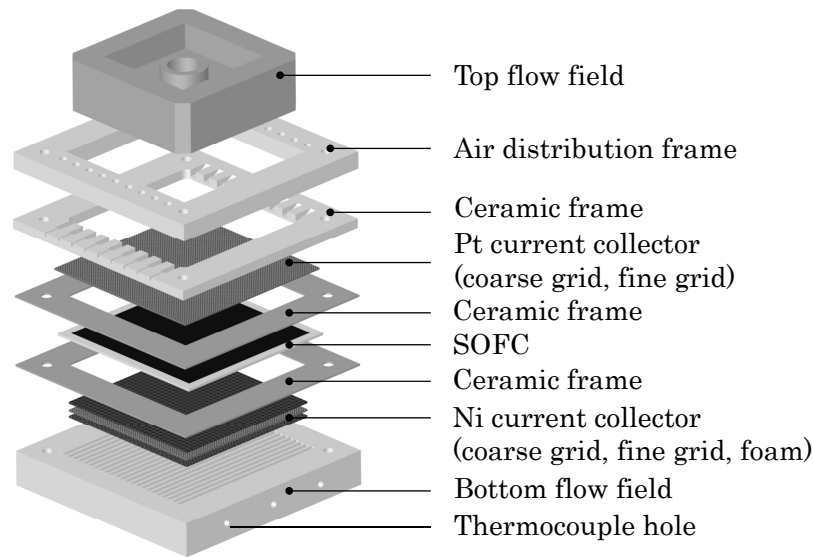Bottom flow field
Thermocouple hole

Figure 5.2: Scheme of ceramic cell housing (Source: [51]).

the cathode side of the cell are positioned. The nickel mesh on the anode side as well as the platinum mesh on the cathode side are connected via platinum wires to the electronic load. Two further platinum wires are used for voltage measurements. At the anode side the feed-through of the platinum wires through the ceramic housing is closed with ceramic paste to ensure gas tightness.

5.1.2 Prototype sensor test rig

The prototype sensor uses an electrolyte supported button cell (Ni-GDC/Ni-YSZ anode, zirconia-based electrolyte, LSM/LSM-GDC cathode) which is implemented in a stainless steel housing (see Figure 5.4). The disc size of the electrolyte is 32 mm while anode and cathode are 12 mm in diameter. The current collection is similar to the cell assembly shown in Figure 5.2.

The scheme of the test rig is shown in Figure 5.3. The anode gas for the cell comes from the gas mixing unit shown in Figure 5.1. The gas passes the reformer before it enters the cell. The 3-way valve allows to bypass the reformer. The anode off gas is sucked to the GA for gas analysis. Both, the reformer and the cell are mounted in an electric oven.

Since the button cell requires a much lower volume flow a mixing concept which allows

to control the volume flow through the button cell is established. The gas mixing unit does not allow the mixing of very low volume flows. A stable volume flow $\dot{V}_{GA}$ which is lower than the anode gas flow $\dot{V}_{fuel}$ coming from the gas mixing unit is adjusted by using the pump of the GA. The excess anode gas is bypassed by the cell directly to the exhaust hood. Since the pump of the GA is limited down to low volume flows an additional mixing air flow is applied. This mixing air $\dot{V}_{MA}$ dilutes the volume flow $\dot{V}_{GA}$ through the GA and reduces the volume flow $\dot{V}_{cell}$ through the cell.
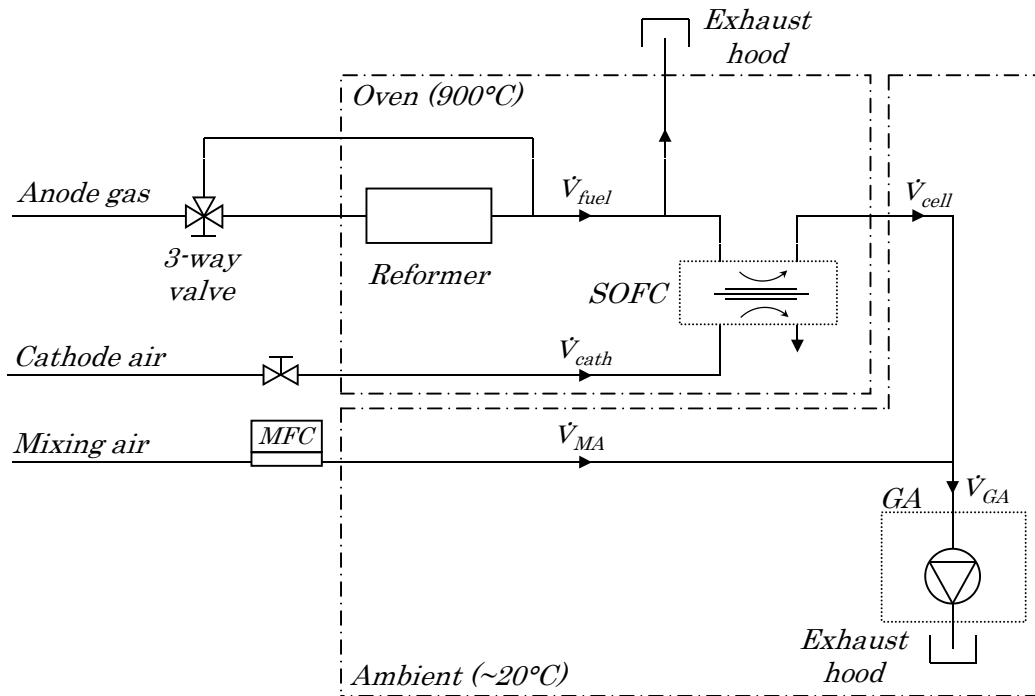

Figure 5.3: Scheme of prototype sensor test rig.

5.1.3 Control technology

A "Power Panel 400" from Bernecker & Rainer is used as control technology system. It enables the whole control task of the experiments including trace heating temperatures, humidifier and bubbler temperatures, volume flows, valve positions, the electronic load, the alarm management and data recording. Furthermore the control engineering implements the monitoring of the gas measurement and visualises the experiment on a touchscreen at the test rig.
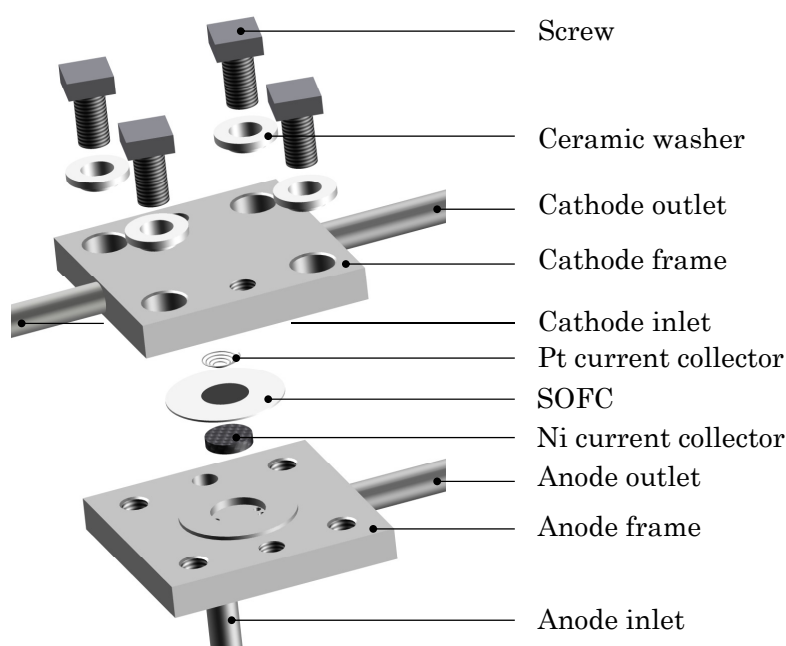
Figure 5.4: Scheme of the prototype sensor housing (Source: [51]).

5.2 Development of representitive synthetic tar mix

In Figure 5.1 the gas mixing unit is shown including the tar bubblers for the addition of a certain tar load. Exemplarily it is shown how the volume flows, the humidifier temperature and the tar bubbler temperatures are determined. Assuming the final gas composition shown in Table 5.1 that has to be achieved the individual volume flows based on a total anode flow of $2400\,\mathrm{Nml/min}$ can be calculated. Then the nitrogen flows through the tar bubblers have to be found in order to achieve the concentration of toluene ($500\,\mathrm{ppm}$), xylene ($500\,\mathrm{ppm}$) and naphthalene ($1000\,\mathrm{ppm}$). The limiting constraints are the tar bubbler temperature and the maximum/minimum nitrogen flow possible through the tar bubblers. On the one hand the tar temperature must be above room or melting temperature and below the boiling point respectively. Furthermore, it should be within the range where the Antoine parameters from Table 4.5 are valid. Eventually the nitrogen flow through the tar bubblers cannot be higher than the total nitrogen flow going into the gas mixing unit. Based on the total anode volume flow and the volumetric tar concentration the tar mass flow can be calculated. The combination of the mass flow of the regarded hydrocarbon and the nitrogen volume flow through the tar bubbler that eventually transports the hydrocarbon due to saturation allows the calculation of the tar bubbler temperature using the Antoine parameters. A higher nitrogen flow through the tar bubbler results in a lower tar bubbler temperature for a specific concentration and vice versa. The tar bubbler temperatures are found

Table 5.1: Example of mixing a representative synthesis gas. The total volume flow amounts to $2400\,\mathrm{Nml}/\mathrm{min}$. The saturation temperature of the tar bubblers are $t_{toluene}$=25.5 °C, t_{xylene}=35.5 °C and $t_{naphthalene}$=84.8 °C. The water humidifier temperature is 75.6 °C

	H_2 [vol.%]	CO [vol.%]	CO_2 [vol.%]	CH_4 [vol.%]	N_2 [vol.%]	H_2O [vol.%]
target	25	13	13	6	13	30
	[Nml/min]	[Nml/min]	[Nml/min]	[Nml/min]	[Nml/min]	[Nml/min]
$N_{2,humidifier}$					30	
$N_{2,toluene}(x_{toluene}=500\,\mathrm{ppm})$					30	
$N_{2,xylene}(x_{xylene}=500\,\mathrm{ppm})$					60	
$N_{2,naphthalene}(x_{naphthalene}=1000\,\mathrm{ppm})$					192	
resulting	600	312	312	144	312	720

to be $t_{toluene}$=25.5 °C, t_{xylene}=35.5 °C and $t_{naphthalene}$=84.84 °C. The corresponding nitrogen flows are listed in Table 5.1. The sum of these three volume flows ($N_{2,toluene}$, $N_{2,xylene}$ and $N_{2,naphthalene}$) must be less than the total nitrogen flow going into the gas mixing unit.

In the same way the humidifier temperature depends on the volume flow going through the water bubbler (H_2, CO, CH_4 and $N_{2,humidifier}$) for a specific H_2O concentration. CO_2 is bypassed at the humidifier due to CO_2 absorption in water.

If the concentration of hydrocarbons has to be modified quickly it is more suitable to adopt the nitrogen volume flow through the considered tar bubbler rather than changing the tar bubbler temperature. Changing the nitrogen flow ($N_{2,CxHy}$) through the tar bubbler leads unavoidably to a change of the nitrogen flow ($N_{2,humidifier}$) through the humidifier (total N_2 stays constant) which will require an adoption of the humidifier temperature in order to keep the water content in the final gas composition constant. However, a change of the tar bubbler temperature instead would also be possible, but this would require a calibration of the temperature dependency of the tar saturation inside the tar bubbler.

The advantage of this mixing concept is that in the case of switching from a tar loaded to a tar free synthetic wood gas, the nitrogen flows through the tar bubblers can easily be bypassed. Thus the volume flow through the humidifier stays constant ensuring a constant water content as well. This is a very significant feature within this work to achieve a high accuracy when comparing the *OCV* for tar loaded and tar free synthesis gas. It has to be guaranteed that the change of *OCV* between these two operating points originates only from the addition of tar and not from inaccuracies of gas mixing.

5.3 Measurement instrumentation

As shown in Figure 5.1 the test rig assembly allows the measurement instrumentation to detect the gas concentration at the cell in- and outlet. Due to the high volume flows needed for the gas analyser as well as for the flame ionisation detector ($\approx 800\,\mathrm{Nml/min}$) it is not possible to operate both devices at the same time. Measuring the concentration before the cell may cause a cell failure if a higher volume flow is sucked from both devices than is supplied from the gas mixing unit. On the other hand the volume flow through the cell is limited and therefore cannot be increased. A significant reduction of the volume flow through the cell has to be accepted whenever the concentration at the cell inlet is measured either with the GA or the FID. This certainly has to be taken into account when validating the cell voltage due to the slight change in cell pressure.

5.3.1 Gas analyser (GA)

A gas analyser (ABB Advanced Optima 2005) is used to measure the H_2, CO, CO_2, CH_4 and O_2 concentration. The position of the GA can be seen in Figure 5.1 and enables the detection of the gas components in the feed stream as well as in the exhaust gas of the SOFC. The GA consists of a gas cooling unit, a gas pump and the following three detectors:

- Thermal conductivity detector (TCD): H_2

- Non dispersive infrared detector (NDIR): CO, CO_2, CH_4

- Electrochemical cell: O_2

The gas cooling unit cools the gas at the entry down to approximately $2\,°\mathrm{C}$ to avoid condensation of water vapor in the downstream pipes and detectors. Thus the measured gas concentration represents the dry gas concentration. The three detectors are put in series and allow a continuous measurement of the gas components. The gas components are not altered by the detectors.

For the TCD the information about the concentration of the gas components, other than H_2, is necessary to determine the H_2 concentration. The values for CO, CO_2, CH_4 and O_2 are obtained directly from the NDIR and the electrochemical cell. The balance is assumed to be N_2. Therefore the existence of large amounts of other gas components than the afore mentioned such as C_2H_2 or C_2H_6 will lead to wrong measuring results.

Table 5.2: Response-factors of hydrocarbons for FID (Source: [87]).

Hydrocarbon	Response factor [1]
naphtalene	1.00
toluene	0.98
xylene	0.93

5.3.2 Flame Ionisation Detector (FID)

A FID (Bernath & Atomic 3005) is used to measure the hydrocarbon concentration. The position of the FID can be seen in Figure 5.1 and enables the detection of the hydrocarbons in the feed stream as well as in the exhaust gas of the SOFC. The signal of the FID represents the volumetric concentration of all hydrocarbons present in the gas mixture measured in propane gas equivalence.

Measuring principle

The measuring principle of the FID is similar to the one described in section 2.2.4.

Propane gas equivalence

If other hydrocarbons than propane are used, the FID signal needs to be converted according to the considered hydrocarbon. This is only possible if one single hydrocarbon is present in the gas mixture. Depending on the amount of carbon atoms and the response factor the real concentration can be calculated with the following equation:

$$x_{C_xH_y} = x_{measured} \cdot \frac{C_{Propane}}{C_{C_xH_y} \cdot f_{Response}} = x_{measured} \cdot f_{C_xH_y} \qquad (5.1)$$

where $x_{measured}$ is the value measured by the FID. $C_{Propane}$ and $C_{C_xH_y}$ are the number of carbon atoms of propane and the considered hydrocarbon respectively. The response-factor $f_{Response}$ is a device related value and comes with the manufacturer. Table 5.2 lists the response-factors used in this work. Eventually a conversion factor $f_{C_xH_y}$ can be introduced.

Calibration of FID

As for most detectors a zero- and endpoint calibration is necessary. The zero point is found by feeding the FID with pure nitrogen. For the endpoint calibration a

propane/nitrogen gas mixture with a certificated propane concentration is used. Only the zero point is adjusted at the FID. The deviation between the measured value and the endpoint concentration is considered by the calibration factor f_{cal}:

$$f_{cal} = \frac{x_{cal}}{x_{measured}} \tag{5.2}$$

where $x_{measured}$ is the concentration measured in the endpoint and x_{cal} the known concentration of propane in the calibration gas.

Influence of hydrogen on the signal

Cross-sensitivity effects are observed when using hydrogen as part of the gas mixture. To determine this dependency nitrogen is compared with a nitrogen/hydrogen mixture both containing the same amount of one hydrocarbon species. Even though the hydrocarbon concentration is similar different signals are obtained. This difference is represented by the conversion factor f_{H_2}:

$$f_{H_2} = \frac{x_{hydrogenfree}}{x_{hydrogen}} \tag{5.3}$$

where $x_{hydrogenfree}$ and $x_{hydrogen}$ are the concentrations measured by the FID for the hydrogen-free and the hydrogen-containing gas mixture respectively. The values for this factor can be seen in Figure 5.5 (left) for a $20/80$ vol.% H_2/N_2 mixture compared to pure nitrogen gas. The tar concentration as well as the tar species are varied. This shows that the influence of the hydrogen concentration is equal regardless of the hydrocarbon concentration and species.

The dependency of the conversion factor f_{H_2} on the the hydrogen content is assumed to be linear (see Figure 5.5, right). Obviously the factor becomes 1 for 0 vol.% H_2. This dependency is expressed using the following equation:

$$f_{H_2} = \frac{\left[\left(\frac{X}{Y} - 1\right) \cdot x_{H_2}\right]}{Z} + 1 \tag{5.4}$$

where X, Y and Z are experimental parameters (see Table 5.3) and x_{H_2} is the H_2 concentration in the gas mixture in *vol.*%.
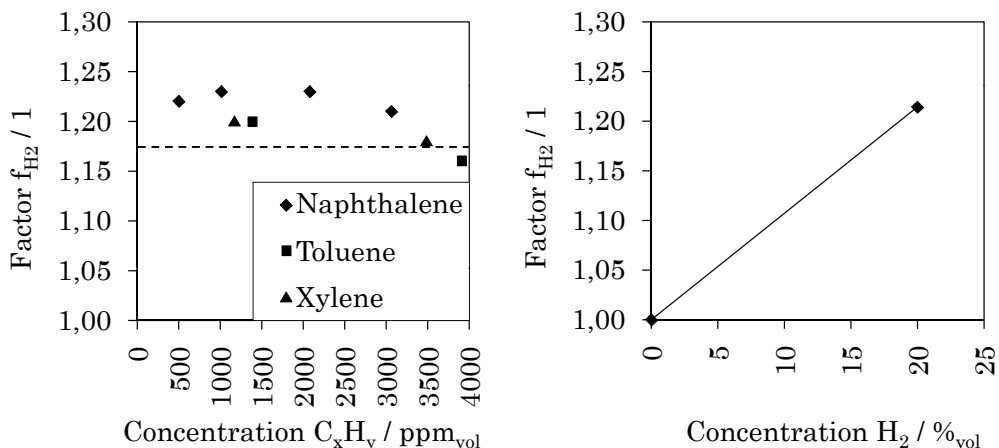
Figure 5.5: Conversion factor f_{H_2} at 20 vol.% hydrogen for different concentrations of naphthalene, toluene and xylene (left). Linearity of the conversion factor when altering the hydrogen content is assumed (right).
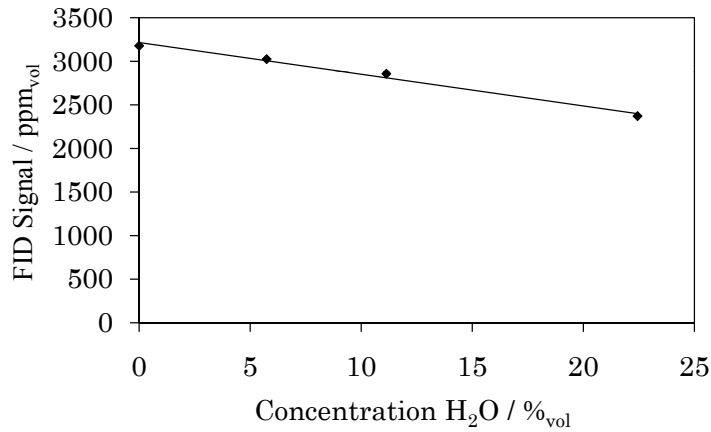
Table 5.3: Experimental parameters for the calculation of f_{H_2} and f_{H_2O}

HC	Hydrogen f_{H_2}			Water f_{H_2O}			
	X	Y	Z	X	Y	Z	**Range**
	[ppm]	**[ppm]**	**[vol.%]**	**[ppm]**	**[ppm]**	**[vol.%]**	**[ppm]**
naphthalene	3060	2460	22.75	2371	3178	22.4	0-4000
toluene	4000	3250	23.31	3250	2750	19.5	≈1000
toluene	11300	9550	23.31	9500	8100	19.5	≈3000
xylene	3650	2950	23.31	2950	2600	19.5	≈1000
xylene	10850	9000	23.31	9000	7700	19.5	≈3000

Influence of H_2O-content

Similar to the influence of H_2 an influence of H_2O on the FID signal is observed. A gas mixture with ≈22/78 vol.% H_2/N_2 and a theoretical naphthalene concentration of approximately 3200 ppm is used. The H_2O-content is varied between 0/5.7/11.1/22.4 vol.% while the naphthalene concentration is kept constant. Figure 5.6 shows the FID signal for these four gas mixtures. The signal already considers the slight differences in the H_2 and $C_{10}H_8$ concentration resulting from the limited accuracy of the MFCs of the gas mixing unit. Further the calibration factor f_{cal} is applied. Although the hydrogen and naphthalene concentration is the same for all four tested gas mixtures a clearly decreasing FID signal with increasing H_2O-content is obtained.

To correct the measured value considering the H_2O-content the conversion factor f_{H_2O}

Figure 5.6: Influence of H_2O-content on the FID-signal

is introduced:

$$f_{H_2O} = \frac{\left[\left(\frac{X}{Y} - 1\right) \cdot x_{H_2O}\right]}{Z} + 1 \tag{5.5}$$

where X, Y and Z are experimental parameters (see Table 5.3) and x_{H_2O} is the H_2O concentration in the gas mixture in *vol*.%.

Conversion of the measured FID signal into the real tar concentration

In order to convert the measured signal gained from FID measurements, all four calibration and conversion factors, respectively, need to be taken into account:

$$x_{C_xH_y} = x_{measured} \cdot f_{cal} \cdot f_{C_xH_y} \cdot f_{H_2} \cdot f_{H_2O} \tag{5.6}$$

At the cell inlet all boundary conditions for the determination of the conversion factors are known. By contrast, a conversion of the signal at the cell outlet is difficult because the H_2O concentration and the type of hydrocarbon is not known at this sample point. Hence, an exact determination of $f_{C_xH_y}$ and f_{H_2O} at the cell outlet is not possible. However, the influence is very small and therefore the failure of $x_{C_xH_y}$ at the cell outlet is negligible.
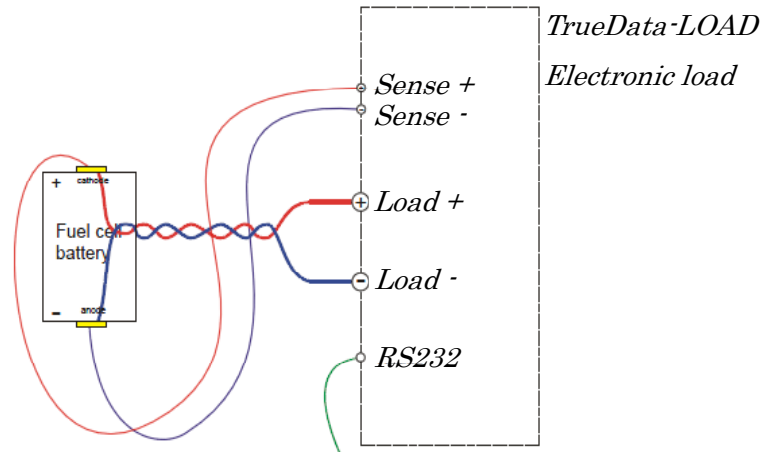
79

Figure 5.7: Electronic load (Source: [40]).

5.4 Electronic load

For the tests carried out on the SOFC test rig (discussed in Chapter 6) the electronic load "TrueData-LOAD" (see Figure 5.7) from FuelCon is used. The electronic load allows to set a constant current for recording V-i curves. The voltage is measured via the two sense wires while the electronic load is conducted over the much thicker load cables. The electronic load is connected via an RS232 interface to the "Power Panel" (see Section 5.1.3) of the control technology.

The prototype sensor tests discussed in Chapter 7 only require a voltage measurement which is carried out with an "Elpro" mobile data logger.

Chapter 6

Investigation of hydrocarbon conversion

This chapter shows the systematic approach of the investigation of hydrocarbon conversion on an SOFC anode. Section 6.1 explains the calculation model that is used to verify the plausibility of the experimental results. The experiments can be divided in those with diluted hydrogen (gas mixture of $H_2/H_2O/N_2$, see Section 6.3 - 6.5) and those where representative synthetic wood gas compositions (see Section 6.6 - Section 6.7) were used. By applying diluted hydrogen the intention was to exclude possible influences on the reforming reaction caused by gas components such as CO, CO_2 and specifically CH_4. This way the strong focus on individual tar reforming gives a reference for the subsequent experiments with synthetic wood gas. Another substantial point of the approach is to test the basic behaviour with the 10x10 cm^2 planar cell in the ceramic housing to exclude any interfering mechanisms coming from stainless-steel housings. From the gained conversion characteristic a concept for the tar sensor including a reformer unit is developed based on theoretic calculations. This concept is then verified for small planar cells in the stainless steel housing of the tar sensor in Chapter 7.

6.1 Calculation model of the equilbrium Nernst voltage

Figure 6.1 shows the different steps for the calculation of the equilibrium concentration and the corresponding equilibrium Nernst voltage for open- and closed-circuit conditions. The Excel add-in named "Chemsheet" based on a thermodynamic database extracted from "FactSage 6.1" is used for the calculation of the equilibrium concentrations. The Nernst voltage is calculated in excel based on Equation 4.26. The combination of excel and the thermodynamic database allows the calculation of the Nernst voltage including the variation of parameters such as temperature, pressure, inlet gas concentration, current density, fuel utilisation rate, anode flow and cathode flow. At the entry of the anode chamber the gas composition as it comes from the gas mixing unit (see Figure 5.1) is taken for step 1 of the calculation. The model enables the calculation for the following gas molecules: H_2, CO, CO_2, CH_4, N_2, H_2O, O_2, $C_{10}H_8$, C_7H_8, C_8H_{10}, C_6H_6O, C_6H_6, $C_{11}H_{10}$, $C_{12}H_{10}$, C_7H_8, C_8H_8, C_9H_{10} and $C_{15}H_{18}$. Additionally solid Ni can be added as well to investigate Ni-oxidation of the

anode.

The equilibrium calculation based on the minimum Gibbs energy includes 228 possible gaseous, liquid and solid products. Ideal gas behaviour is taken into account. Hydrocarbons, up to $C_{20}H_y$, are chosen as possible products from the database. Inhibitions of the equilibrium reactions due to slow kinetics cannot be considered.

In the model the resulting equilibrium concentration may only consist of: H_2, CO, CO_2, CH_4, N_2, H_2O, O_2, $C_{10}H_8$, C_7H_8, C_8H_{10}, C_6H_6O, C_6H_6, $C_{11}H_{10}$, $C_{12}H_{10}$, C_7H_8, C_8H_8, C_9H_{10} and $C_{15}H_{18}$. In order to control whether carbon deposition or nickel oxidation takes place the solid components C and NiO are included to the resulting composition. All other possible products usually occur in negligible amounts. The resulting equilibrium concentration, in particular the oxygen partial pressure is then taken to calculate the Nernst voltage at open-circuit conditions.

To obtain the Nernst voltage in operation the resulting equilibrium concentration at open-circuit conditions is taken and augmented by the amount of oxygen migrating from the cathode to the anode side. The oxygen migration flow is determined through the desired current density or the fuel utilisation respectively. In both cases the stoichiometric amount of oxygen necessary for the electrochemical reactions of H_2 and CO to H_2O and CO_2 can be calculated (see Equation 4.10-4.14. Additionally, the model supports the option to consider the electrochemical oxidation of CH_4. In this case the amount of oxygen coming from the cathode side likewise considers the stoichiometric amount for CH_4 oxidation. Consequently the new equilibrium concentration for closed-circuit conditions is calculated in a second step.

For the calculation of the Nernst voltage the air at the cathode side is used with $21\,\text{mol\%}$ O_2 and $79\,\text{mol\%}$ N_2. For closed-circuit conditions the cathode air is reduced by the amount of oxygen that is used for the electrochemical oxidation of H_2 and CO. However, the air composition is considered constant in order to avoid effects due to the decrease of the oxygen partial pressure at the cathode side for high current densities. This effect is achieved by using a very high air flow which can be adopted in the model by choosing a very high air/fuel ratio λ. Atmospheric pressure for both anode and cathode is used for all calculations.

The aim of the model is to enable the simulation of different conversion rates of the hydrocarbons (definition see Equation 4.38) between 0 and $100\,\%$ as gathered later from real measurement data. According to the equilibrium the hydrocarbons will be reformed and shifted completely in the presence of sufficient water at temperatures above $800\,^{\circ}\text{C}$. In reality this is not always the case due to kinetic inhibition. Since there is no possibility to partly suppress the reforming reaction within the equilibrium calculation, the start concentration of the considered hydrocarbon is changed accordingly. For example having an individual hydrocarbon concentration of $2000\,\text{ppm}$ and aiming at simulating a reforming rate of $60\,\%$ leads to an individual hydrocarbon concentration of $1200\,\text{ppm}$. These $1200\,\text{ppm}$ are taken to calculate the equilibrium while the remaining $800\,\text{ppm}$ are balanced by N_2 to keep the concentration of the other gas
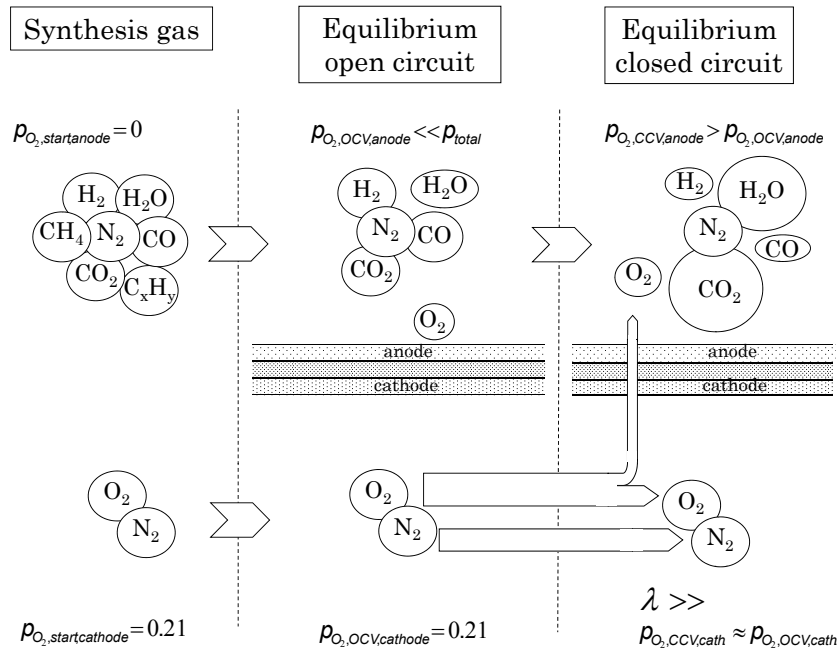
Figure 6.1: Calculation model.

species untouched. When comparing measured values with theoretical values later the considered conversion rate will be referred to. This is important when considering carbon deposition for lower conversion rates. In reality a lower conversion rate signifies a certain amount of hydrocarbons that are not converted. Nevertheless, this amount could still lead to carbon deposition whereas in this calculation this effect is not considered due to the use of balance N_2.

6.2 Estimation of failure sources

The aim of the experiments is to measure the *OCV* as well as the cell voltage in operation and verify its plausibility by the calculation of the Nernst voltage using the cell inlet gas composition. In this work the measured *OCV* is compared with the theoretical Nernst voltage. When comparing the experimental and the theoretical value, possible failure sources have to be taken into account. In this context it can be said that the experimental value of the voltage is closer to the real value than the Nernst voltage, based on the fact that the voltage can be measured quite accurately and has less failure sources. However, differences between the experimental *OCV* and the theoretical Nernst voltage may evolve because the *OCV* and the Nernst voltage deviate from the real value.

1. Failure of *OCV*: the voltage measurement of the electronic load deviates from the real value.

2. Failure of Nernst voltage: the assumption for the calculation of an equilibrium gas composition at the anode may not represent the real state. For example, in terms of reforming, kinetic inhibition is a very significant factor why the equilibrium may not be reached. Other operating parameters such as temperature, pressure or inlet gas composition taken for the calculation are obtained from measurements and thus may not represent the real state. These deviations arise simply because of systematic errors or uncertainties of the measurement equipment.

Certainly these considerations are most important if one wants to verify the absolute value of the voltage. However, the failure might be eliminated when a voltage difference between two operating points is focused on (as for the increase of *OCV* described in Figure 6.3). The failure plays a minor role and may be accepted when predicting trends. To be able to assess the results of the experiments properly the individual failure sources are quantified in Table 6.1. The values presented are calculated with the simulation model shown in Section 6.1. A reference gas composition at 900 °C and 0.984 bar absolute, for which the Nernst voltage is determined, is used. At the cathode side air with 21 vol.% O_2 and rest N_2 is taken.

For each failure source the respective parameter is changed while the rest is kept constant. For example if the real temperature was 910 °C instead of 900 °C as gained from the thermocouple the Nernst voltage would be −3.5 mV lower than expected. This is important to consider since the actual cell temperature which is significant for the cell voltage cannot be measured in situ. The thermocouples are located inside the oven compartment and within the cell housing beneath the anode (see Figure 5.2). The difference according to thermocouple measurements usually amounts to ≈ 20 K. By contrast, inaccuracies of the measurement of the cell pressure appear not to play a big role.

A failure source which is hard to estimate is the impact of the H_2O-content. The real value is difficult to measure. Gravimetric H_2O measurements as done in this work are not very precise because they represent only a mean value. However, an offset of +2 vol.% absolute, as the maximum deviation from the theoretical value is presumed to be for the temperature range where the humidifier is used, leads to a voltage difference of −2.7 mV.

The major failure source truly arises from the knowledge about the exact dry gas composition at the cell inlet. In this work two ways to determine the dry gas composition are applied. Calculating the composition from the individual flows of the MFCs which are calibrated with a certified volume flow meter (GIL) is one method. The second option is to measure the dry gas composition with the gas analyser (GA). For this work it was decided that the first method is the more accurate. Therefore the dry gas composition used for the calculation is always based on the first method. However,

the gas composition at the outlet shown in the results section are measured values from the gas analyser. Table 6.1 shows a typical deviation as it occurs when either the gas composition from method one or two is taken for the calculation of the Nernst voltage.

Another failure source that is difficult to value is the prediction of the conversion rate of the hydrocarbons. Whereas the real amount of converted methane can be measured with the gas analyser it is rather difficult for mixtures of higher hydrocarbons as the amount of each species converted cannot be detected. To follow the calculations in the results section the estimated conversion rate will be quoted accordingly.

Poor sealing of the cell housing can have two effects: Either air enters the anode chamber where the oxygen would most likely react with the hydrogen or fuel happens to leak. The exact process is not known, however in experiments with diluted hydrogen the gas composition is measured before and after the cell. Under open circuit conditions a decrease from 29.02 down to 28.05 vol.% H_2 between in- and outlet of the cell is observed. Theoretically this can be caused through dilution and oxidation of hydrogen if 1.43 vol.% air enters the anode chamber. In case of a fuel leakage one would assume that the concentration of the fuel does not change since all gas components would leak in the same proportion. However, hydrogen is a very small molecule and therefore it is conceivable that only hydrogen streams out due to poor sealing. Then, simply, a decreased hydrogen concentration by ≈ 1 vol.% absolute at the inlet has to be considered. Both cases are shown in table 6.1.

Here, mostly voltage differences rather than the exact value of the absolute voltage are of interest. Therefore the failure sources are eventually categorised whether they impact the absolute value of the Nernst voltage (offset) only or the difference (ΔU) as well.

Failure estimation of measured OCV

The absolute failure of the voltage measurement of the electronic load in the range of 600 to 1100 mV is estimated to be ± 2.3 mV as no technical specification of the measurement device is available. However, the voltage is frequently compared with a "multimeter". The two measured values for the voltage from the electronic load and the "multimeter" deviate from each other approximately around 1 mV.

Failure estimation of calculated Nernst voltage

The calculation of the Nernst voltage is based on measurements of the parameters m_i: temperature, pressure, inlet gas composition (x_{H_2}, x_{CO}, x_{CH_4}, x_{CO_2}, x_{N_2} and x_{H_2O}), concentration of higher hydrocarbons ($x_{C_xH_y}$) and the assumption that an equilibrium gas composition is reached. The uncertainties u_{x_i} are estimated or taken from the measurement device if given (see Table 6.2).

Table 6.1: Failure sources and their impact on the Nernst voltage. The differences refer to the reference Nernst voltage of 932.3 mV for an anode gas mixture based on GIL measurements at 900 °C and 0.984 bar. Air is used at the cathode

Failure sources	Absolute [mV]	Difference [mV]	Difference [%]	Impact
Gas composition				
based on GIL[1] (reference)	932.3	-	-	
based on GA[2]	923.9	-8.4	-0.90	offset
Conversion rate				
+200 ppm abs. $C_{10}H_8$	933.0	+0.7	+0.08	ΔU
+1 vol.% abs. CH_4	937.1	+4.8	+0.51	ΔU
poor sealing				
+1.43 % abs. Air	930.9	-1.4	-0.15	offset
−0.97 % abs. H_2	931.4	-0.9	-0.10	offset
Temperature +10 K	928.8	-3.5	-0.38	offset
Pressure +20 mbar	932.8	+0.5	+0.05	offset
H_2O-content +2 vol.% abs.	929.6	-2.7	-0.29	offset

[1] 20.25 % H_2, 12.95 % CO, 12.96 % CO_2, 6.17 % CH_4, 28.79 % H_2O, 2000 ppm $C_{10}H_8$ and bal. N_2

[2] 19.32 % H_2, 13.04 % CO, 16.24 % CO_2, 5.58 % CH_4, 28.79 % H_2O, 2000 ppm $C_{10}H_8$ and bal. N_2

Then the absolute uncertainty of the Nernst voltage in mV is calculated with the following equation according to the Gaussian error propagation:

$$u_{V_{Nernst}} = \sqrt{\sum_{x_i} \left(\frac{\Delta V_N}{\Delta x_i} \cdot u_{x_i} \right)^2} \tag{6.1}$$

The Nernst voltage is exemplarily calculated for a gas mixture of 22.5 % H_2, 16.0 % CO, 16.5 % CO_2, 6.9 % CH_4, 19.5 % H_2O, 2000 ppm C_7H_8 and balance N_2 at 0.99 bar and 900 °C. Considering Equation 6.1 the resulting Nernst voltage accounts to 950.3 ± 1.8 mV. It can be stated that the value of the uncertainty $u_{V_{Nernst}}$ will be approximately the same for all other gas compositions used in this work. In the case of diluted hydrogen $u_{V_{Nernst}}$ will be lower as less gas components have to be mixed.

In Figure 6.2 the dependency of $u_{V_{Nernst}}$ on the parameters $x_{C_7H_8}$, x_{H_2}, x_{H_2O}, t and p_0 are shown. For the calculation of these curves the gas mixture from Table 6.2 is taken. Each diagram shows the alteration of the Nernst voltage and the uncertainty $u_{V_{Nernst}}$ if one parameter is varied. Generally it can be seen that there is not a big variation of $u_{V_{Nernst}}$ in the range where those parameters are used.

Eventually the absolute value of the Nernst voltage accounting to 950.1 mV must be corrected according to the offset resulting from poor sealing and the real equilibrium

Table 6.2: Parameters for the calculation of the uncertainty $u_{V_{Nernst}}$. The Nernst voltage accounts to 950.3 mV

m_i	**Value**	$\frac{\Delta V_N}{\Delta x_i}$	u_i
t	900 °C	0.35 mV/°C	±2.9 mV
p	990 mbar	0.03 mV/mbar	±2.9 mV
x_{H_2}	22.5 vol.%	0.54 mV/vol.%	±2.4 mV
x_{CO}	16.0 vol.%	0.42 mV/vol.%	±2.6 mV
x_{CH_4}	6.9 vol.%	0.20 mV/vol.%	±2.9 mV
x_{CO_2}	16.5 vol.%	0.43 mV/vol.%	±2.6 mV
x_{N_2}	18.6 vol.%	0.47 mV/vol.%	±2.6 mV
x_{H_2O}	19.5 vol.%	0.28 mV/vol.%	±1.4 mV
$x_{C_7H_8}$	0.2 vol.%	0.02 mV/vol.%	±0.001 mV
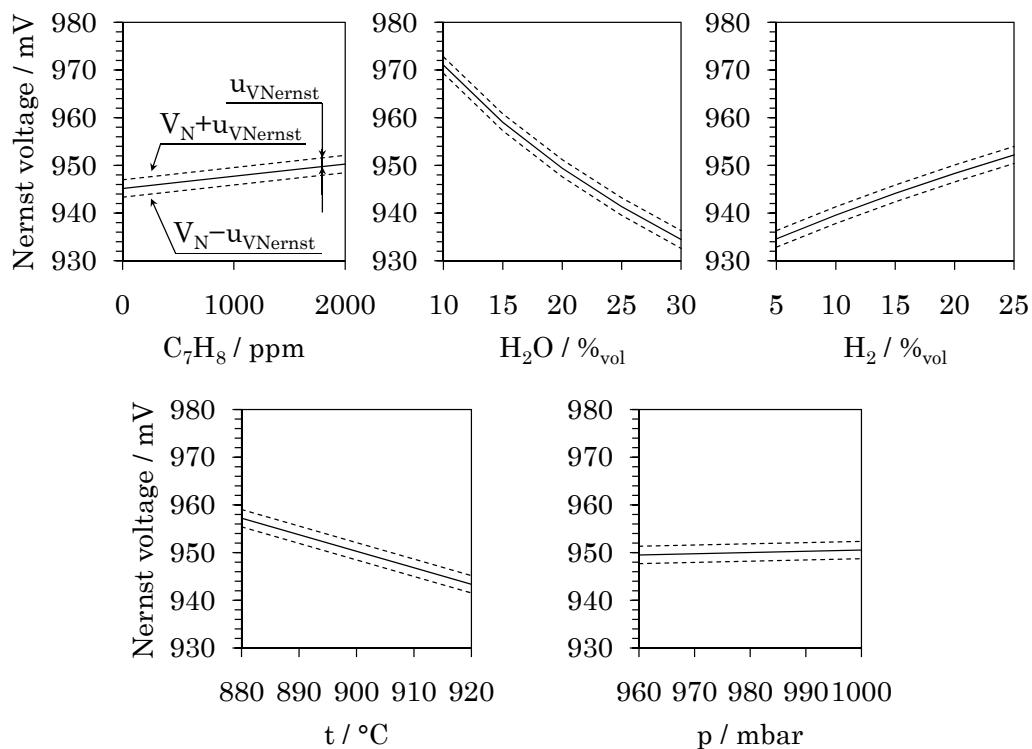
Figure 6.2: Nernst voltage including the uncertainty $u_{V_{Nernst}}$ for the operation with synthesis gas (22.5 % H_2, 16.0 % CO, 6.9 % CH_4, 16.5 % CO_2, 19.5 % H_2O, balance N_2 and 2000 ppm C_7H_8) at 900 °C and 990 mbar. For each diagram the parameter on the x-axis is varied while the other stay constant (except balance N_2).

87

gas concentration which necessitates the conversion rate of the hydrocarbons. This offset will be mentioned specifically for the following tests.

6.3 Ideal operation temperature of the measurement cell

The first step is to find the ideal operation temperature at which all hydrocarbons become steam reformed. Another aim is to avoid carbon deposition which requires high temperatures. With a view to the stainless-steel sensor housing that is eventually supposed to be used, temperatures above $900\,°C$ are not favorable due to the material properties. The tests described in this section are carried out with the $10x10\,cm^2$ planar cell mounted in the ceramic housing (see Figure 5.2). Diluted hydrogen ($H_2/H_2O/N_2$) with additions of either naphthalene, xylene or toluene is tested at 800 and $900\,°C$ to find out the lowest temperature necessary to reform the hydrocarbons.

Testing procedure

In the beginning of the test a tar free gas mixture is applied until a constant voltage signal is obtained and a longterm drift can be excluded. At stable operating conditions the *OCV* usually varies by 2-3 mV (see Figure 6.3) which is likely to be related to the slightly intermittent humidification of the gas stream. This means that the humidity itself is slightly fluctuating in reality. At dry gas conditions the *OCV* varies only by 1 mV.

After attaining a stable voltage signal one tar species is added by closing the bypass of the respective tar humidifier (see Figure 5.1). As can be seen exemplarily from Figure 6.3 a voltage increase of $\Delta OCV \approx 4$ mV is observed immediately after starting with the addition of naphthalene. For the determination of the voltage increase an average value of the slightly fluctuating voltage signal is taken.

Assessment of failure sources

As the gas flow through the water humidifier as well as the humidifier temperature is retained it can be guaranteed that the following voltage increase can be ascribed to tar conversion rather than to an unintended change in humidification. Moreover, the dry gas composition at the cell inlet monitored by the GA is similar for the operation with and without tar load. A voltage increase due to a decreasing temperature based on the cooling effect of the endothermic reforming reaction at the anode can be excluded because no such indication was observed from the thermocouples. The tested tar concentrations are listed in Table 6.3. The tar concentration is measured with the FID at the cell inlet. Since only one tar species at a time is used the FID signal
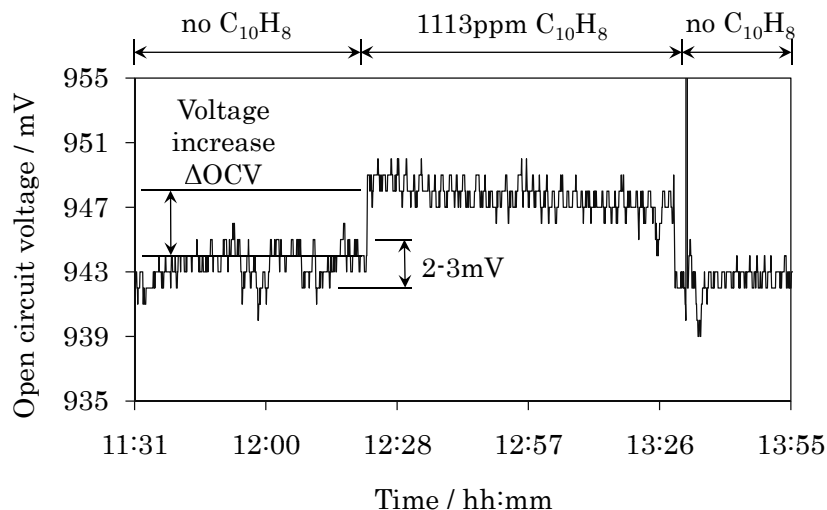
Figure 6.3: *OCV* for the operation with diluted hydrogen (23.3 % H_2, 19.5 % H_2O, balance N_2) and 1113 ppm $C_{10}H_8$ at 800 °C.

Table 6.3: Tar concentrations at the cell in- and outlet of the experiments shown in Figure 6.4 at 900 °C. The outlet concentrations are given in propane gas equivalence.

Tar	500		1000		2000		3000	
	inlet	outlet	inlet	outlet	inlet	outlet	inlet	outlet
	[ppm]	[ppm]	[ppm]	[ppm]	[ppm]	[ppm]	[ppm]	[ppm]
naphthalene	483	*0*	1113	*3*	2118	*27*	3606	*99*
xylene	-	-	1034	*2*	2215	*2*	3377	*2*
toluene	-	-	1306	*1*	2632	*1*	3949	*2*

at the inlet can clearly be converted to the actual concentration. At the outlet it is not known which kind of hydrocarbon is present since it would be possible that the signal is produced by cracking products and not by the inlet hydrocarbons. For this reason, it is not possible to convert the listed outlet signal into a specific hydrocarbon concentration.

Temperature dependent conversion of hydrocarbons

Figure 6.4 shows the increase of the open circuit voltage ΔOCV between operation with tar free gas and tar loaded gas. As can be seen ΔOCV is higher, the higher the inlet tar concentration is (solid curve). The linearity of the increase corresponds to the predicted voltage increase based on equilibrium calculations (dashed curve). The
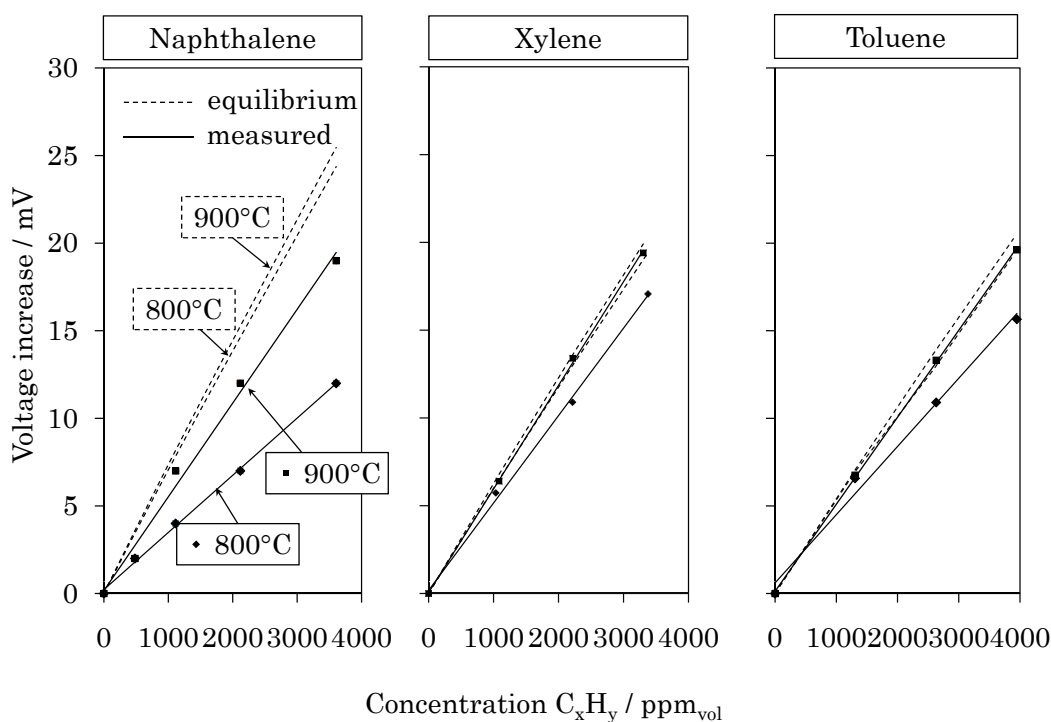
Figure 6.4: Increase of *OCV* due to the conversion of naphthalene, toluene or xylene for the operation with diluted hydrogen (23.3 % H_2, 19.5 % H_2O, balance N_2 and a varying C_xH_y concentration) at 800/900 °C and 0.99 bar.

calculation of the Nernst voltage is based on complete conversion of the hydrocarbons. Furthermore, a clear temperature dependency can be attributed to all three tested tar species resulting in a larger voltage increase at 900 °C compared to 800 °C. However, for naphthalene only 75 % of the theoretical voltage increase of 25 mV at 900 °C and 3606 ppm is reached. Looking at the naphthalene outlet concentration, which is 99 ppm, one would assume that the real voltage increase must be closer to equilibrium. The conversion rate at 900 °C apparently decreases with increasing naphthalene concentration. Hence one could expect that the *OCV* increases other than linearly for naphthalene concentrations above 3606 ppm.

While FID analysis only provides information about the amount of tar converted to non-hydrocarbon products more information is gained by looking at the amounts of H_2, *CO* and CO_2 at the cell outlet. Assuming that reforming and shift reaction dominate the conversion of tar the GA analysis enables an estimation about the limiting reaction. In Figure 6.5 the H_2, *CO* and CO_2 outlet concentrations at 800 and 900 °C are given for the tested naphthalene loads and compared to equilibrium calculations. The measured

value of H_2 is corrected to account for $\approx 1\%$ absolute H_2 leakage. The comparison corresponds to the assumption of a temperature dependent conversion rate. H_2 and CO_2, being below equilibrium concentration, differ more the higher the naphthalene concentration is and show a similar non-linear characteristic as seen from the FID signal. The gaps between the measured values and equilibrium are smaller at $900\,°$C than at $800\,°$C. CO nearly matches equilibrium concentration which may occur due to a limited reforming reaction combined with a limited shift reaction. In this case less CO is produced by reforming followed by a lower consumption due to the shift reaction. A limited shift reaction could be one explanation why the voltage increase does not correspond to equilibrium even though FID analysis shows almost complete conversion of naphthalene (see Table 6.3). To confirm this scenario a more precise detection regarding the type of hydrocarbons at the outlet would be necessary to verify whether cracking products of naphthalene are present. FID measurements listed in Table 6.3 suggest almost complete conversion of naphthalene at $900\,°$C considering that the signal correlates to the naphthalene content. If other hydrocarbons were present the signal would have to be interpreted differently.

Comparing the results of the three tar species (see Figure 6.4) one can see that equilibrium voltage increase is reached for xylene and toluene at $900\,°$C. This is further confirmed by FID analysis of the outlet concentration (see Table 6.3). The outlet concentration varies between 1 and 2 ppm showing complete conversion.

Correlation between voltage increase and tar concentration

Figure 6.4 shows that the absolute value of the voltage increase for a specific tar concentration depends on the tar species. For instance 1000 ppm naphthalene create a higher voltage increase compared to 1000 ppm toluene or xylene. However, if the theoretical voltage increase is drawn over the tar concentration in g/Nm³ on a wet basis as illustrated in Figure 6.6 it becomes obvious that a linear correlation exists. In this figure each point represents 3000 ppm of the respective tar species which results in a certain concentration in g/Nm³ on a wet basis. A scale (see additional x-axes in Figure 6.6) for the conversion from g/Nm³ in *ppm* is given for a better illustration in the case of naphthalene and toluene. Because of the distinct molecular weights of the tar species the concentration in g/Nm³ on a wet basis is different although the volumetric concentration in *ppm* is the same. Interestingly, all points for the non-alcoholic hydrocarbons (no OH group) are located on one straight line. This shows that the voltage increase can be brought in direct relation to the total tar concentration in g/Nm³ on a wet basis according to following equation,

$$w_{C_xH_y} = k_{C_xH_y} \cdot \Delta V_N = 0.802 \cdot \Delta V_N \tag{6.2}$$

where $w_{C_xH_y}$ is the total tar load in g/Nm³ and ΔV_N is the Nernst voltage increase in

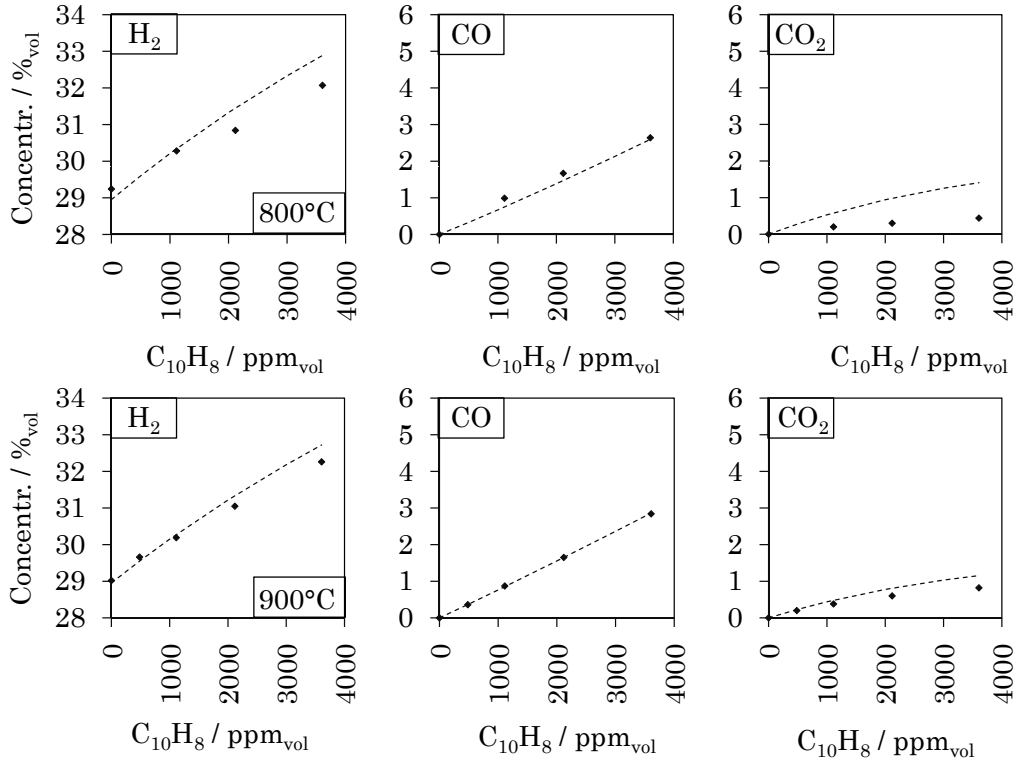Figure 6.5: H_2, CO and CO_2 anode outlet concentration (dotted: equilibrium, points: measured) for the operation with diluted hydrogen (23.3 % H_2, 19.5 % H_2O, balance N_2) and a varying $C_{10}H_8$ concentration (0, 483, 1113, 2118 and 3606 ppm) at 800 and 900 °C.

mV. The slope $k_{C_xH_y}$ is given in $g/(\text{Nm}^3\cdot\text{mV})$. In the same way the following equation can be found for alcoholic hydrocarbons (such as phenol).

$$w_{C_xH_yO_z} = k_{C_xH_yO_z} \cdot \Delta V_N = 1.028 \cdot \Delta V_N \qquad (6.3)$$

Alcoholic hydrocarbons generate a lower voltage increase due to their hydroxyl group. The hydroxyl group eventually increases the oxygen partial pressure in equilibrium which directly affects the Nernst voltage according to Equation 4.26. It is important to note that Equation 6.2 and 6.3 are only valid for the gas mixture as used in Figure 6.6. Other gas mixtures, for example synthesis gas, may lead to different slopes $k_{C_xH_y}$ and $k_{C_xH_yO_z}$.

To determine an equivalent concentration following conversion can be used for example for naphthalene or toluene,

$$E_{C_{10}H_8, equivalent} = \frac{3000}{17.17} \cdot w_{C_xH_y} \qquad\qquad = 174.7 \cdot w_{C_xH_y} \qquad (6.4)$$

$$E_{C_7H_8, equivalent} = \frac{3000}{12.34} \cdot w_{C_xH_y} \qquad\qquad = 243.1 \cdot w_{C_xH_y} \qquad (6.5)$$

where $E_{i,equivalent}$ is in *ppm* and $w_{C_xH_y}$ in g/Nm³ on a wet basis.

Additionally the voltage increase of a real tar mix based on the concentration shown in Table 4.3 is calculated and indicated in Figure 6.6 (blank triangle). The concentration of the tar species is measured by means of SPA. It is based on a dry synthesis gas composition (consisting of H_2, CO, CO_2, CH_4 and N_2). However, the same tar concentration that is based on a dry basis is taken and converted to a wet basis using 19.5 % H_2O as used in Figure 6.6 (23.3 % H_2, 19.5 % H_2O, balance N_2) in order to compare the tar mix with the individual tar species. Therefore, the tar load of 6018 mg/Nm³ (based on dry synthesis gas, see Figure 4.3) changes to 4854 mg/Nm³ (based on 19.5 % H_2O as used in Figure 6.6). This results in a theoretical voltage increase of 5.7 mV. It is shown that the tar mix is between the straight line for non-alcoholic and alcoholic hydrocarbons. This seems to be conceivable considering that the ratio between the concentration of non-alcoholic and alcoholic hydrocarbons for the known tar species amounts to 0.8. This means that the amount of non-alcoholic (2127 mg/Nm³) tar species is almost as much as those of the alcoholic (2622 mg/Nm³) tar species.

The ratio between non-alcoholic and alcoholic tar species depends on the gasification technology and gasification parameters. Usually, the tar composition is roughly known for a specific gasification technology and thus the ratio can be estimated. In particular, for a bubbling allothermal steam fluidised bed gasifier, the phenolic tar components depend on the gasification temperature and the steam value [58].

If the voltage increase can be measured for synthesis gas in the same way as it is shown in Figure 6.6 then it is possible - considering the estimated ratio between non-alcoholic and alcoholic tar species - to determine the total tar concentration in g/Nm³. This method will be investigated in more detail in Chapter 7.

To further verify this theory the measured voltage increases of Figure 6.4 are shown over the concentration in g/Nm³ on a wet basis in Figure 6.7. For 900 °C xylene and toluene are located very close to each other supporting the theoretical values of Figure 6.6. The values for naphthalene are below the expected common line for non-alcoholic hydrocarbons for reasons explained above in Figure 6.4.
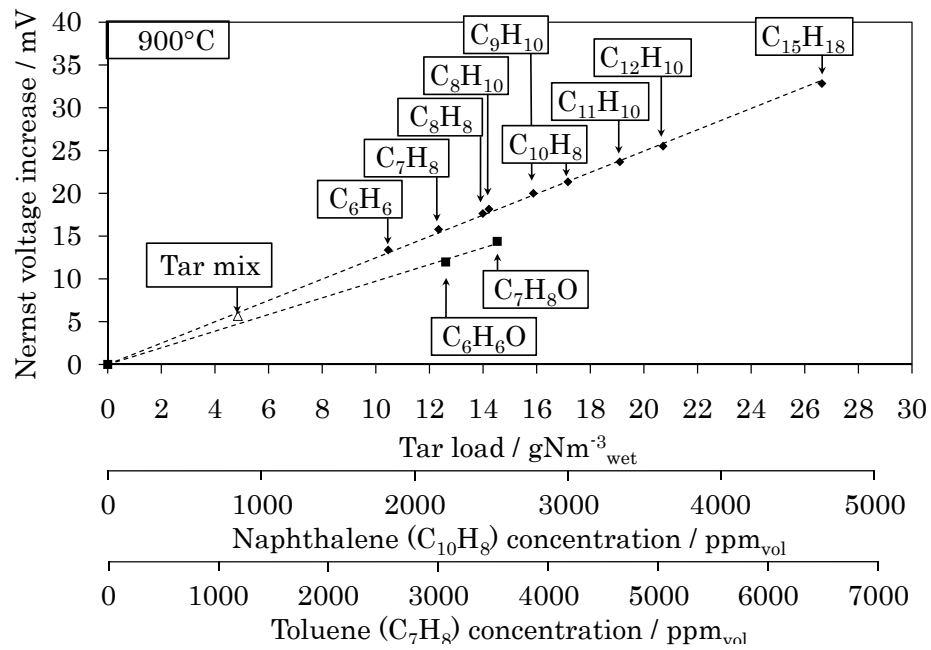
Figure 6.6: Increase of Nernst voltage due to the conversion of tar for the operation with diluted hydrogen (23.3 % H_2, 19.5 % H_2O, balance N_2) and 3000 ppm of C_xH_y or $C_xH_yO_z$ at 900 °C and 0.99 bar. The blank triangle indicates a representative tar mix of 4854 mg/Nm³.
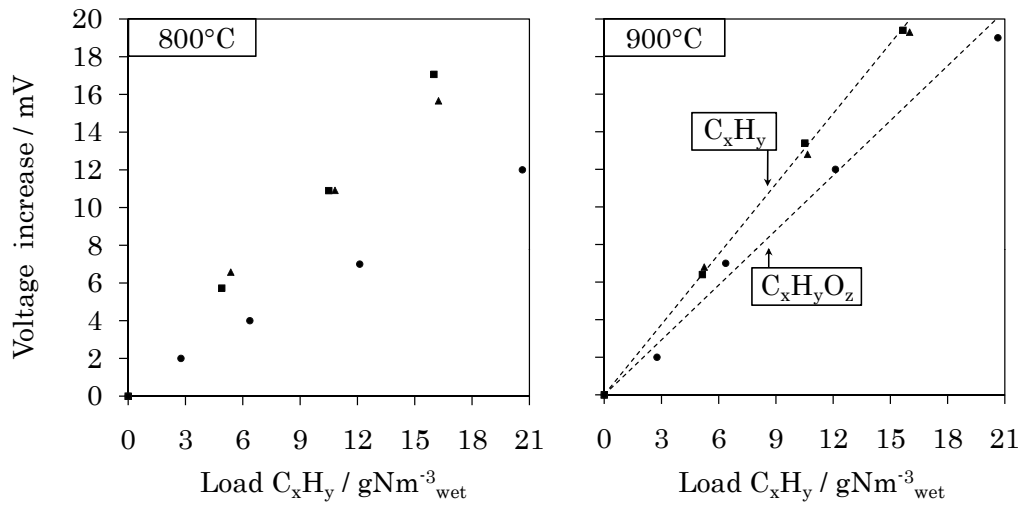
Figure 6.7: Increase of the *OCV* due to the conversion of tar for the operation with diluted hydrogen (23.3 % H_2, 19.5 % H_2O, balance N_2) and a varying concentration of $C_{10}H_8$ (circles), C_8H_{10} (squares) and C_7H_8 (triangles) at 800 °C (left) and 900 °C (right). The dotted curves in the right graph represent the fit curves for $w_{C_xH_y}$ and $w_{C_xH_yO_z}$ according to Equation 6.2 and 6.3.

Shift reaction

The investigation of an inhibited shift reaction may be the reason why the voltage increase does not reach equilibrium for the operation with naphthalene is shown in Figure 6.8. The aim of this experiment is to demonstrate whether or not the shift reaction is in equilibrium in order to proof that reforming of naphthalene itself is the limited reaction. Therefore the intention is to separate the reforming step from the shift step. For this reason an inlet gas composition is calculated based on the assumption of complete reforming but no shift reaction of a gas mixture containing 23.3 % H_2, 19.5 % H_2O, 3606 ppm $C_{10}H_8$ and balance N_2 (as used in the prior experiment).

The new obtained gas mixture consists of 27.0 % H_2, 15.1 % H_2O, 3.4 % CO and balance N_2. The comparison between the measured and the thermodynamically predicted values for CO and CO_2 based on the dry gas composition shows good conformity. Furthermore the measured value for H_2 (=31.5 %) is very close to the theoretical value (=31.3 %). The calculation considers an H_2 leakage of 1.2 % absolute to account for poor sealing. The voltage signal is shown to confirm stable operating conditions. "Inlet" and "outlet" indicate whether the gas composition is measured before or after the cell. At ≈10:42 the experiment is finished and it is switched to an $H_2/H_2O/N_2$ gas mixture.

Due to these results it can be expected that the shift reaction itself is not the limiting step. However, in this case no reforming step and therefore no possible adsorption effects of naphthalene interfered with the shift reaction. Competing adsorption or reaction respectively between naphthalene and carbon monoxide may still occur. Furthermore in reality the shift reaction takes place after the reforming step, leaving less time for the shift reaction to achieve completion. In order to investigate whether an increased residence time would close the gap between the measured and the theoretical voltage increase in Figure 6.4 for naphthalene the volume flow needs to be reduced. However, limitations of the gas mixing unit do not allow such experiments.

As a result of the first set of experiments the ideal operating temperature is found to be 900 °C. Although a higher temperature than 900 °C may have advantages regarding naphthalene conversion kinetics, limitations of the potential sensor material (stainless steel) do not suggest further experiments at higher temperatures.
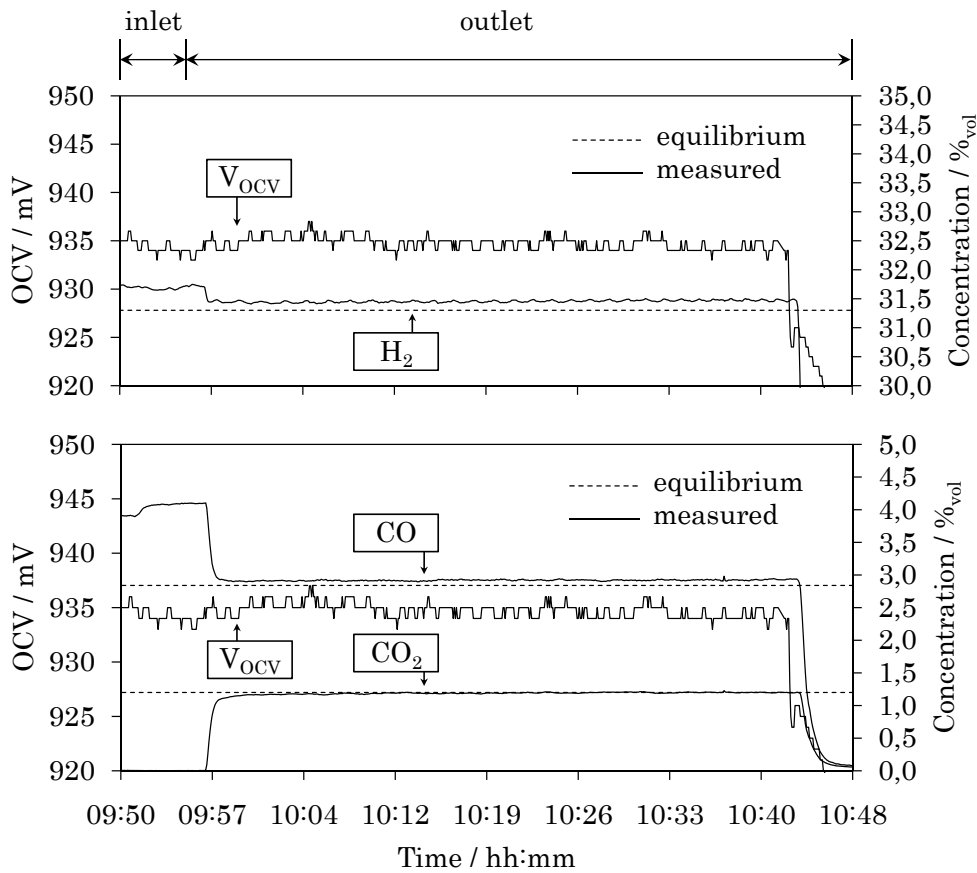
Figure 6.8: H_2, CO and CO_2 anode outlet concentration (dashed: equilibrium, solid: measured) for a wet gas mixture (27.0 % H_2, 15.1 % H_2O, 3.4 % CO and balance N_2) at 900 °C and open circuit (note that the values in the diagram are based on a dry gas composition).

6.4 Influence of current collector on hydrocarbon conversion

The anode layer is contacted with a Ni foam and two Ni grids for current collection as can be seen in Figure 5.2. As Ni is catalytically active it is investigated to which extend the anode layer and the Ni current collection respectively supports the conversion of hydrocarbons. Therefore, three different test series are performed with diluted hydrogen at 900 °C. For the first test the electrolyte material without anode layer is used in order to verify whether the Ni current collector is capable to convert hydrocarbons. In the second test the SOFC (with anode layer) is used but without current collector to prove that the anode layer supports the conversion of hydrocarbons. Dur-

Table 6.4: Conversion of tar for three different cell assembly set-ups for diluted hydrogen ($\approx 22\,\text{vol.\%}$ H_2, $22\,\text{vol.\%}$ H_2O, balance N_2 and $\approx 3200\,\text{ppm}$ $C_{10}H_8$) at $900\,^\circ\text{C}$

Test	$C_{10}H_8$ conc. before anode [ppm]	$C_{10}H_8$ conc. after anode [ppm]	Conversion rate [%]
No anode/with current collector	3240	68	97.9
With anode/no current collector	3130	47	98.5
No anode/no current collector	3180	2410	24.2

ing the last test only the electrolyte material without anode layer and without current collector is used. This way it can be verified whether a conversion due to thermal cracking or decomposition takes place. The hydrogen content varies between the three tests from 21.6 to 23.7 % while the water content is kept between 21.8 and 22.4 %. The tests are described in more detail in [62]. Table 6.4 shows the conversion rates for an inlet concentration of naphthalene of $\approx 3200\,\text{ppm}$. In this table it is assumed that the hydrocarbon present after the anode is still naphthalene. Therefore, the outlet concentration represents the naphthalene equivalent.

From the results it can be deducted that the anode layer itself supports the conversion. This is an important information for a potential sensor design where the current collection may be accomplished differently in a way that less or no Ni material is used for current collection.

6.5 Operation under electrical load

This section is supposed to work out whether the electric current under load conditions has any influence on the occurring reactions such as reforming or shift. Normally the oxygen migrating from the cathode to the anode reacts with the H_2 or CO at the triple phase boundary (TPB, see Section 4.4.1). It is not entirely clear yet whether a direct electrochemical oxidation of methane or even higher hydrocarbons are practically possible on Ni anodes. Theoretically, the oxygen ion may react with the adsorbed hydrocarbon as well. However, as reported in Chapter 3 the material used for the anode configuration is of major importance for electrochemical oxidation of hydrocarbons. The anode material used in this work (Ni-GDC) is rather expected to either support steam reforming or carbon deposition depending on the amount of water used. This is most likely due to the reason of Ni being a good catalyst for these reactions. As the reforming reaction is expected to take place on the Ni-surface (see Section 4.5.3)

and not at the TPB a reaction between oxygen and adsorbed hydrocarbon molecules seems further unlikely. On the other hand the produced water at the TPB from the electrochemical reaction may influence the steam reforming reaction positively.

However, for the overall concept the opportunity of operating the tar sensor under electrical load may offer a wider spectrum of modes of operation. For instance the positive effect regarding the avoidance of carbon deposition may be a desirable feature for the measurement of synthesis gas with low levels of water.

Voltage increase at elevated current densities

Figure 6.9 shows V-i curves at 800 and 900 °C for a gas mixture of 23.3 vol.% H_2, 19.5 vol.% H_2O and balance N_2 for 0, 483 and 3606 ppm $C_{10}H_8$. The current density is increased approximately every 10 min in steps of 40 mA/cm². Due to the technical limitation of the electronic load no current densities higher than 190 mA/cm² can be applied. After reaching 190 mA/cm² the voltage is kept for 10 min and then decreased in the same way down to 0 mA/cm². The solid line represents the V-i curves for increasing current densities ("up") whereas the dashed curve represents decreasing ("down") current densities. To avoid effects resulting from transient operation the V-i curves are measured once a stable outlet concentration of naphthalene is detected with the FID. Initially it takes up to an hour upon switching to naphthalene addition until a steady state is reached (see Section 6.7).

At 900 °C the V-i curves are flatter and start at a lower open circuit voltage compared to 800 °C as expected from the theory. Furthermore, the curves are linear suggesting ohmic losses only in the tested current density range. The cell voltage is generally higher when the cell is operated with naphthalene. This indicates that the conversion of naphthalene is not affected by the current density. For example the voltage increase at 800 °C and 150 mA/cm² for 3606 ppm naphthalene amounts to 15 mV which is approximately the same compared to 17 mV at open circuit conditions (compare with Figure 6.4).

The clear temperature dependency of the conversion step is still obvious under electrical load. Therefore these results suggest that the conversion is not influenced by the electrical current through electrochemical oxidation of H_2 and CO.

An interesting abnormality occurs at 800 °C and 3606 ppm naphthalene. For this case a clear difference between the values of the "up" and "down" curves is observed. This must be an effect that occurs at the beginning when the V-i curve is recorded and which disappears after a certain amount of time. Recording more V-i curves in a row shows no more changes compared to the "down" curve of Figure 6.9. A temperature effect arising from the heat of the electrochemical reaction of H_2 and CO is excepted because this would require the observation of the same effect during operation at 900 °C or at lower naphthalene concentrations respectively.

Biber [21] refers in her investigation to the positive effects of carbon deposition observed by several researchers. Isolated nickel particles may be connected by carbon depositions and thus improve the electrical conductivity. However, these enhancements are followed by drastic degradation of the cell voltage enabling the positive effects only for a short time. Since carbon deposition is more favorable at lower temperatures this could be an explanation why this effect is not seen at $900\,°C$.

Comparison with syngas operation

Similar tests are performed with synthetic wood gas mixtures as illustrated in Figure 6.10. The same behaviour concerning the gap between the curves for increasing and decreasing current densities occurs. However, in this case the gap at $800\,°C$ exists for operation with and without naphthalene indicating that this effect is not restricted to the operation with naphthalene but could be caused by any other carbon containing molecules such as methane.

More importantly, it is recognised that the voltage increase induced by naphthalene which is again under electrical load as high as for open circuit conditions.

Outlet gas analysis

No changes of the reforming activity under electrical load is further supported by FID analysis. The outlet concentration of naphthalene for the test shown in Figure 6.9 are fairly constant while altering the current density. Observations of slight changes of the FID signal are attributed to the changing amount of H_2 and H_2O which both cause cross-sensitivity effects (see Section 5.3.2).

The outlet concentration of H_2, CO and CO_2 is drawn over the current density in Figure 6.11 for a gas mixture of $23.3\,\%$ H_2, $19.5\,\%$ H_2O, $483/3606\,\mathrm{ppm}$ $C_{10}H_8$ and balance N_2 at $900\,°C$. The measured H_2 concentration is corrected to take into account a leakage of about $1\,\%$ absolute. The values for open circuit conditions at $0\,\mathrm{mA/cm^2}$ are the same as in Figure 6.5. For the predicted equilibrium concentration not only the inlet gas concentration has to be known precisely but also the value of the total anode flow is important otherwise a wrong ratio between the amount of the anode gas components and the oxygen coming from the cathode is used for the calculation. Based on the trend of the H_2 concentration the calculated and measured curves match properly. *CO* on the other hand seems not to be consumed at high current densities whereas a slight increase of CO_2 can be observed. However, the theoretical amounts of *CO* consumption are low and within the detection limit of the GA. For $3606\,\mathrm{ppm}$ $C_{10}H_8$ it can be seen that equilibrium does not seem to be reached neither for open circuit nor under electrical load whereas for $483\,\mathrm{ppm}$ $C_{10}H_8$ the concentration is close to thermodynamics. No specific behaviour can be found from the operation under
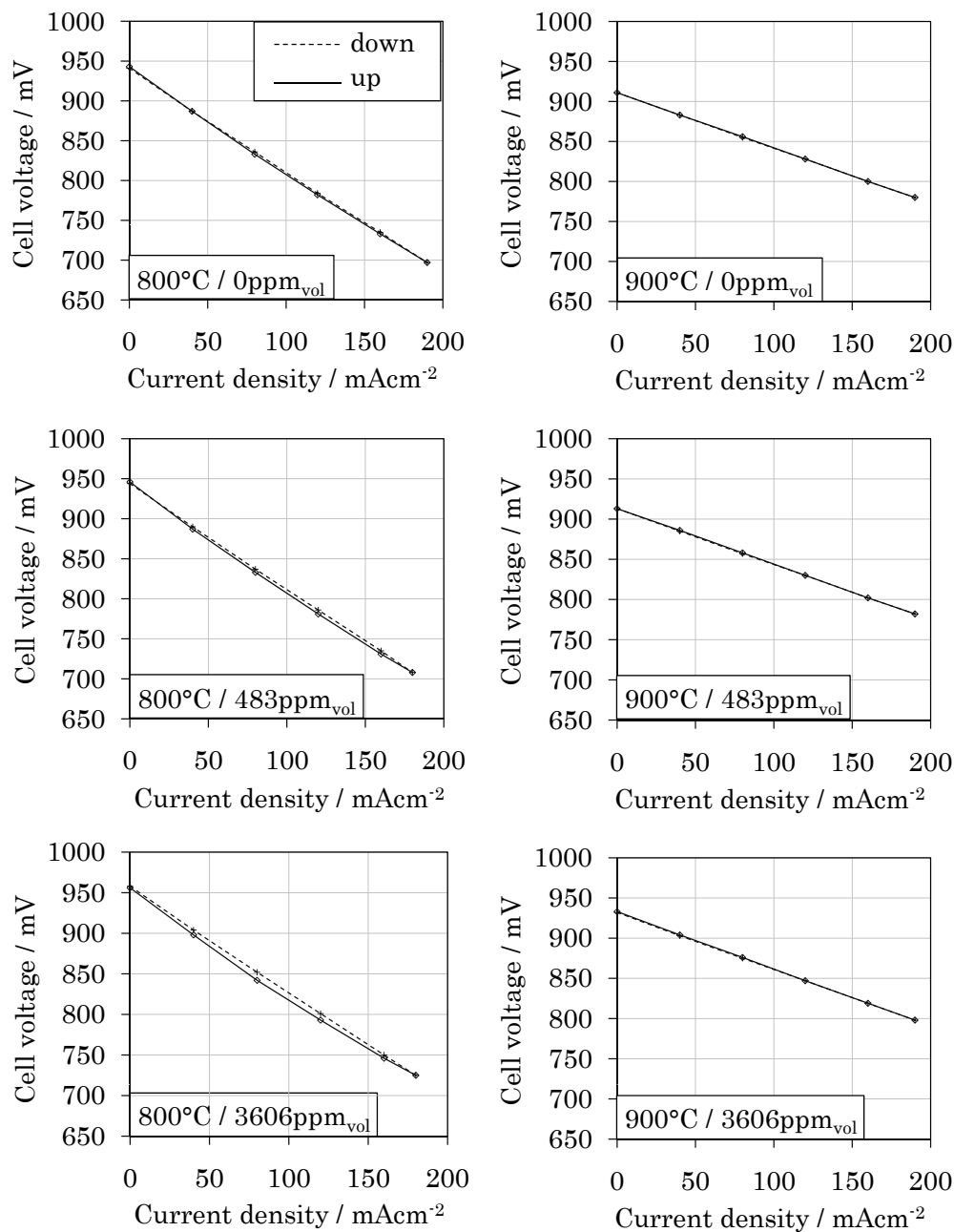
Figure 6.9: V-i curve for the operation with diluted hydrogen (23.3 % H_2, 19.5 % H_2O, balance N_2) and a varying $C_{10}H_8$ concentration (0, 483 and 3606 ppm) at 800 (left) and 900 °C (right).
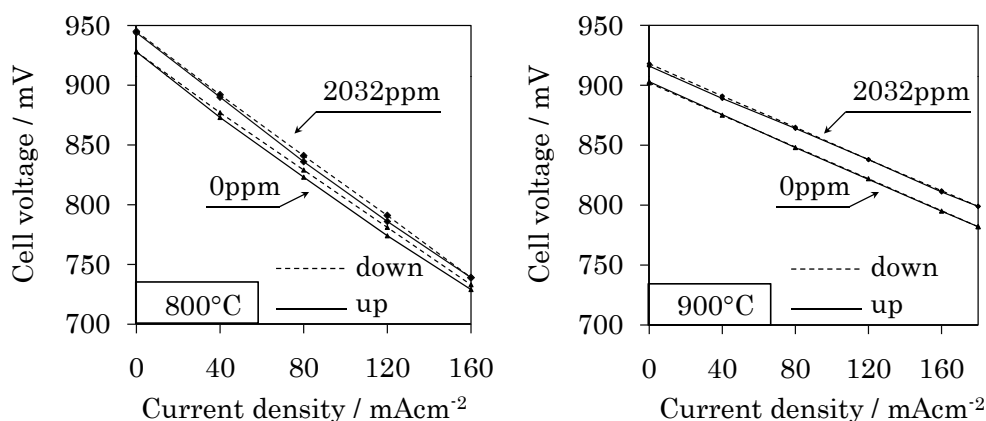
101

Figure 6.10: V-i curve for the operation with "synGas" (20.8 % H_2, 13.3 % CO, 13.3 % CO_2, 6.3 % CH_4, 26.8 % H_2O, balance N_2) and a $C_{10}H_8$ concentration of 0 and 2032 ppm at 800 (left) and 900 °C (right).

electrical load which is seen as further evidence that the conversion is not influenced during the electrical operation of the cell.

Reforming activity of methane:

To verify whether the reforming activity of methane on a Ni-GDC anode under synthesis gas conditions is influenced under electrical load, the outlet concentration belonging to the V-i curve shown in Figure 6.10 at 900 °C is displayed in Figure 6.12. The solid lines represent the permanent gas components and the dashed lines show the value of the current density. Whereas in the prior described experiment the consumption of CO is hardly visible here a clear decrease of CO with increasing current density can be detected. CH_4 which is hardly converted due to the presence of $C_{10}H_8$ (more about this phenomenon in Section 6.6) does not show any changes due to the increase of the current density suggesting neither any interference with the conversion reaction nor with the electrochemical oxidation.

Figure 6.13 shows the interval between 17:15 and 17:49 of Figure 6.12. The addition of naphthalene is stopped around 17:20 (I) while the rest is kept constant. A slowly decreasing amount of methane indicates an increasing conversion rate of methane due to the absence of naphthalene. At 17:31 the current density is again switched from 0 to 180 mA/cm². Electrochemical oxidation of H_2 and CO is clearly visible while no effect on methane occurs. This further suggests that the electrical current or the oxygen ion flow coming from the cathode respectively does not interfere with the competing reforming reaction of the hydrocarbons on the Ni-surface.
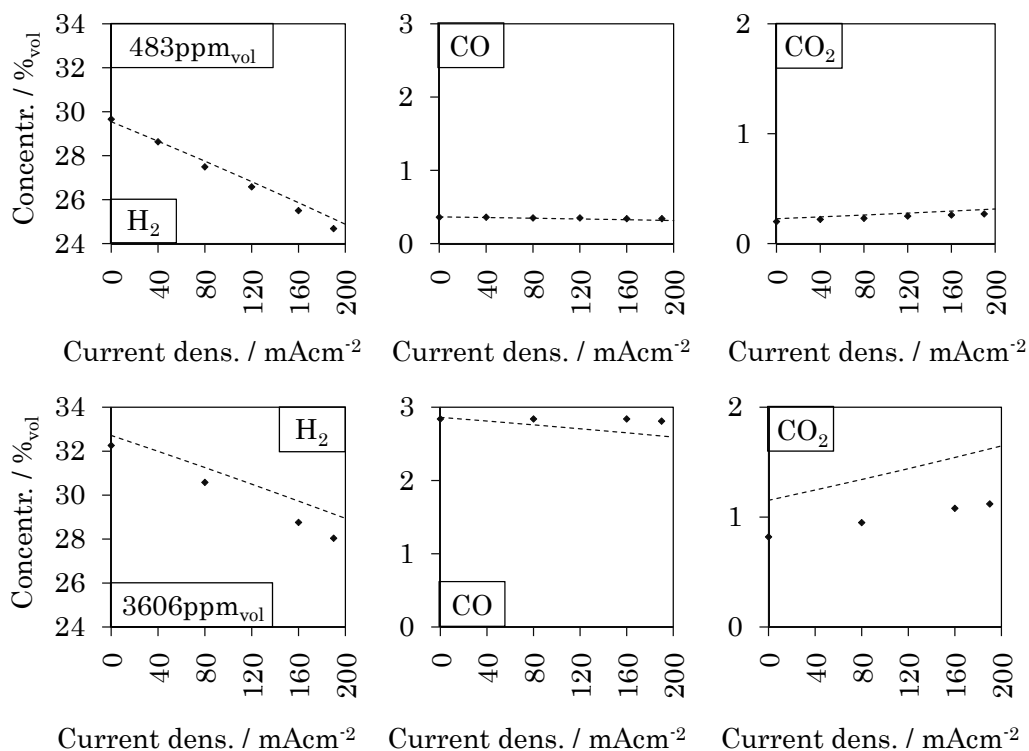
102

Figure 6.11: H_2, CO and CO_2 anode outlet concentration (dotted: equilibrium, points: measured) for the operation with diluted hydrogen (23.3 % H_2, 19.5 % H_2O, balance N_2) and a varying $C_{10}H_8$ concentration (top: 483, bottom: 3606 ppm) at 900 °C for varying current densities.
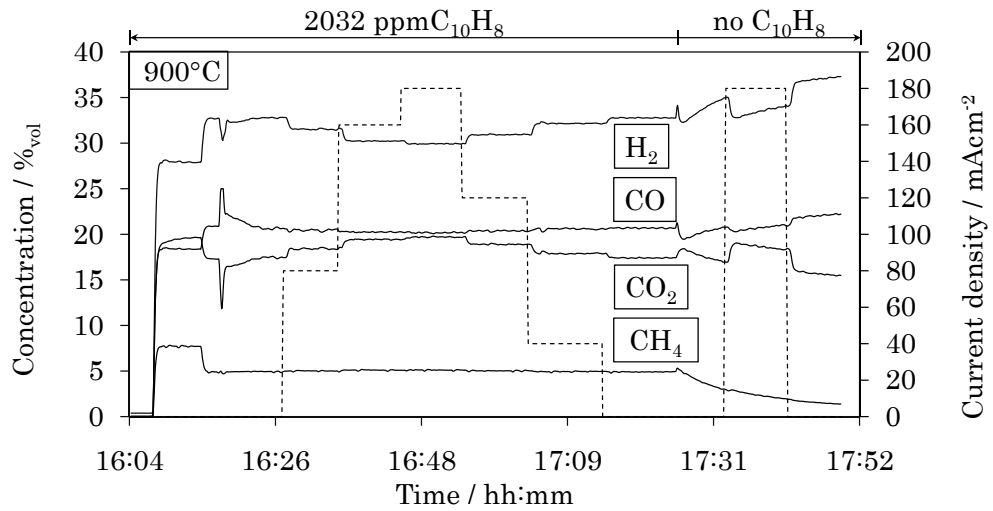
Figure 6.12: H_2, CO, CO_2 and CH_4 outlet concentration (solid) and current density (dashed) for the operation with "synGas" (20.8 % H_2, 13.3 % CO, 13.3 % CO_2, 6.3 % CH_4, 26.8 % H_2O, balance N_2) and 2032 ppm $C_{10}H_8$ at 900 °C.
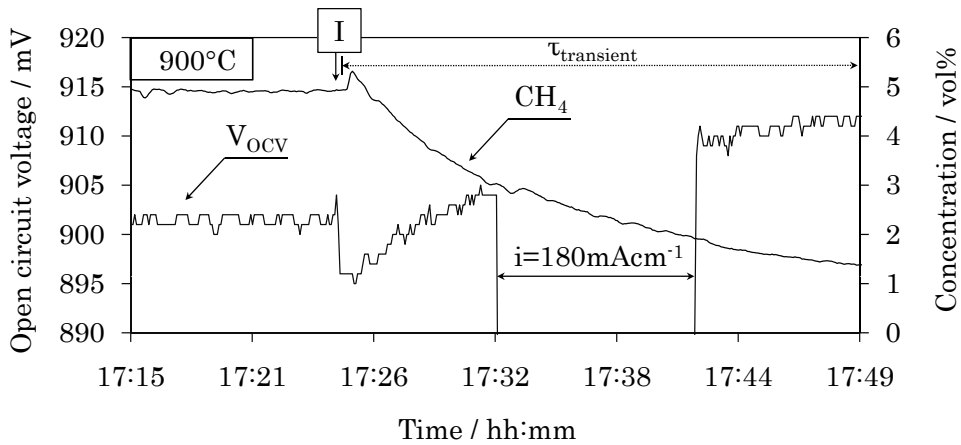
Figure 6.13: CH_4 outlet concentration and OCV for the operation with "synGas" (20.8 % H_2, 13.3 % CO, 13.3 % CO_2, 6.3 % CH_4, 26.8 % H_2O, balance N_2) and 2032 ppm $C_{10}H_8$ at 900 °C.

6.6 Measuring a mixture of multiple hydrocarbon components

This chapter investigates the voltage increase of the *OCV* for simultaneous use of several hydrocarbons. In fact first diluted hydrogen is tested with naphthalene, toluene and xylene. Then synthetic wood gas containing CH_4 is tested as well with these three tar species. In particular it is focused on the mutual impact of the simultaneous conversion of the hydrocarbons present at the anode.

6.6.1 Diluted hydrogen with naphthalene, toluene and xylene

The results of Figure 6.4 are taken and extended with results from experiments where naphthalene, toluene and xylene is mixed in various combinations. Diluted hydrogen (23.3% H_2, 19.5% H_2O and balance N_2) is tested at 800 and 900 °C. Table 6.5 shows the test matrix in order to illustrate which tar concentrations are combined. The table also shows the results of the real measured voltage increase (ΔOCV) and what can be expected from equilibrium considerations (ΔV_N). As before it can be seen that the voltage increase is much lower for 800 °C.

The main point of this test is to verify whether the resulting voltage increase for a combination of tar corresponds to the sum of the individual voltage increases of the tar species as achieved in Figure 6.4. The sum is reached where ΔOCV is close to ΔV_N. In this case both tar species are completely converted as for the combination of toluene and xylene (ΔOCV=12.3 mV close to ΔV_N=13.1 mV). The situation is a bit different when naphthalene is additionally present in the gas mixture. While naphthalene alone is converted almost completely (ΔOCV=7.3 mV close to ΔV_N=8.2 mV) a combination of naphthalene, toluene and xylene does not reach equilibrium (ΔOCV=17.7 mV lower than ΔV_N=20.8 mV).

Another illustration is given in Figure 6.14. There, the real (solid) and the theoretical (dotted) voltage increase is represented by the diameter of the spheres. The three-dimensional diagram is used to show the combinations of these three tar species. Each

Table 6.5: Test matrix for the simultaneous use of naphthalene, toluene and xylene at 900 °C for diluted hydrogen (23.3% H_2, 19.5% H_2O, balance N_2)

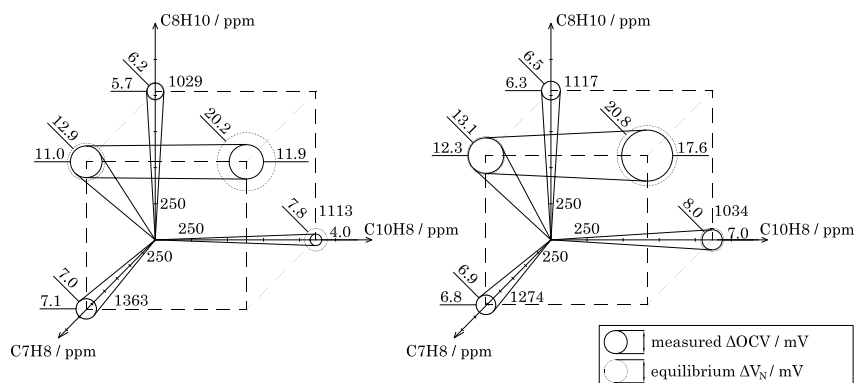| $C_{10}H_8$ [ppm]	C_7H_8 [ppm]	C_8H_{10} [ppm]	V_{OCV} [mV]	ΔOCV [mV]	ΔV_N [mV]	Σtar [g/Nm³]
0	0	0	910.7	0	0	0
0	0	1034	917.0	6.3	6.5	4.27
1117	0	0	918.0	7.0	8.0	5.57
1117	1274	0	923.0	12.3	14.8	10.13
0	1274	1034	923.0	12.3	13.1	8.83
1117	1274	1034	928.3	17.6	20.8	14.40

Figure 6.14: Comparison of the increase of the OCV (solid spheres) and the Nernst voltage (dotted spheres) in mV due to the conversion of tar for the operation with diluted hydrogen (23.3 % H_2, 19.5 % H_2O, balance N_2) and a varying concentration of $C_{10}H_8$, C_8H_{10} and C_7H_8 at 800 (left) and 900 °C (right).

axis represents the concentration of one specific tar. The numbers attached to the spheres show that either ΔOCV (for solid spheres) or ΔV_N (for dotted spheres) are similar to what is shown in Table 6.5.

Apparently, the conversion of some or all tar species becomes incomplete the more species that are mixed. Figure 6.21 shows the FID outlet concentration for a stepwise combination of the three tar species (the explanation of the testing procedure is found in the respective text in Section 6.7.1). While a combination of toluene and xylene still leads to high conversion rates the addition of naphthalene seems to slowly inhibit the conversion step. Therefore an increasing FID signal is gained. Nevertheless the OCV increases due to the additional naphthalene.

For this reason the voltage increase is not automatically the sum of the individual voltage increases coming from the tar species. These results show that the determination of the individual concentration of the tar species is in this case not possible because there is no information about how much each tar species contributes to the total voltage increase. However, according to Figure 6.6 the voltage increase can clearly be related to the total concentration in g/Nm³.

Figure 6.6 shows that a voltage increase of ΔOCV=17.7 mV, as achieved for the combination of naphthalene, toluene and xylene (see Table 6.5), theoretically results in concentration of $\approx$ 14.2 g/Nm³ on a wet basis. This is close to the applied concentration of 14.40 g/Nm³ (see Table 6.5).

Table 6.6: Tested gas mixtures in Figure 6.15 for the impact of naphthalene on methane conversion (balance is N_2)

Gas mixture	H_2 [%]	CO [%]	CO_2 [%]	CH_4 [%]	H_2O [%]	C_8H_{10} [ppm]	C_7H_8 [ppm]	$C_{10}H_8$ [ppm]
"synGas"	20.3	13.0	13.0	6.2	28.8	0/606	0/721	0-2874
"smart synGas"	25.4	7.1	14.2	3.7	32.9	0/576	0/681	0-2349
"LowFuel"	10.9	7.6	7.6	3.9	45.8	0/547	0/794	0-2249

6.6.2 Synthetic wood gas with naphthalene, toluene and xylene

As explained in the section before the combination of hydrocarbons may lead to inhibitions concerning the hydrocarbon conversion step which directly influences the OCV. As the measuring principle is intended to be used for synthetic wood gas it has to be tested whether the conversion of methane is influenced as well by other hydrocarbons. Therefore three different synthetic wood gas compositions (see Table 6.6) are investigated in a similar test matrix as used in Table 6.5. As the prior results show that a temperature of 900 °C is favorable to reach equilibrium no experiments at 800 °C are carried out.

The three gas compositions ("synGas", "smart synGas" and "LowFuel") are tested once with naphthalene only and once simultaneously with naphthalene, toluene and xylene. The concentrations can be seen in Table 6.6. First the cell outlet gas composition is measured with the GA in order to monitor the methane outlet concentration. By comparing it with the inlet concentration the conversion rate CR_{CH_4} is found. A clear dependency of CR_{CH_4} from the naphthalene concentration is shown in Figure 6.15. As long as there is no naphthalene present CR_{CH_4} is almost 100 %. Toluene and xylene do not seem to impact the methane conversion. However, additions of small amounts of naphthalene already significantly lower the conversion rate of methane. By comparing the data from tests with (filled points) and without (blank points) toluene/xylene reveal that these two hydrocarbons do not significantly influence the CR_{CH_4}-curve. Interestingly, the results are very similar for all three gas compositions, although major differences in the amount of the permanent gas components exist. For example the water content differs substantially (from 28.8 to 45.8 % H_2O). Another significant observation is that the methane inlet concentration does not have an influence on the conversion rate of methane in the investigated range (from 3.9 to 6.2 % CH_4). These methane inlet concentrations are approximately the range that represents allothermal steam gasification. Following empiric equation describes the conversion of methane at the SOFC anode at 900 °C.

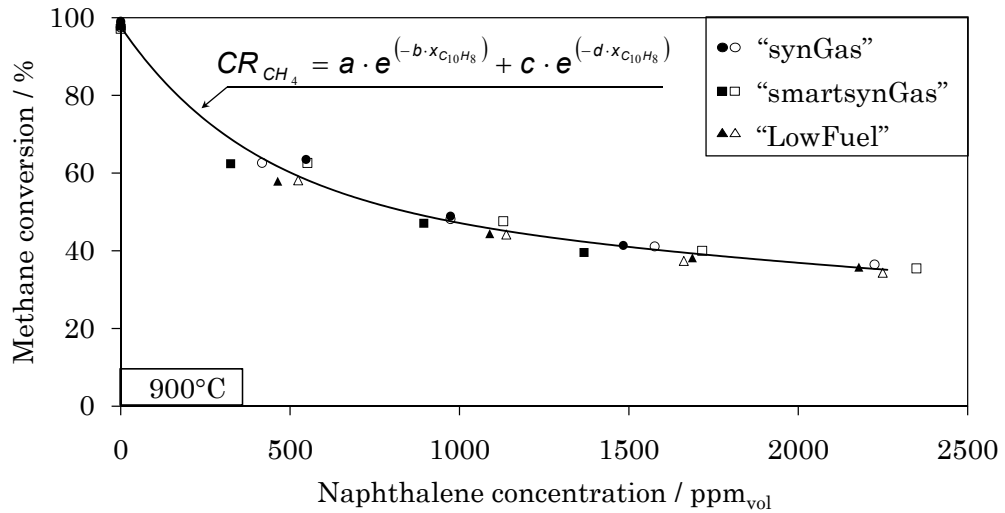$$CR_{CH_4} = a \cdot e^{-b \cdot x_{C_{10}H_8}} + c \cdot e^{-d \cdot x_{C_{10}H_8}} \tag{6.6}$$

Figure 6.15: Conversion of methane in the presence of naphthalene for three differ-
ent gas mixtures (see Table 6.6) with (filled points) and without (blank
points) toluene/xylene (fit curve parameters: $a = 45.1686$, $b = 0.0026$,
$c = 52.5143$, $d = 0.0002$).

The parameters of the fit curve are: a=45.1686, b=0.0026, c=52.5143, d=0.0002.

Furthermore, it would be interesting to know by how much the conversion of toluene
and xylene is inhibited by naphthalene. An exact determination, as achieved for
methane, is not possible since there is no possibility to measure the individual hydro-
carbon outlet concentration continuously.

Another important issue is the residence time. Here, the volume flow is $2413 \, \mathrm{Nml/min}$
which is obviously low enough to reach $CR_{CH_4} \approx 100\%$ for operation without naph-
thalene. However, increasing the volume flow up to $4800 \, \mathrm{Nml/min}$ clearly shifts the
whole CR_{CH_4}-curve downwards. For operation without naphthalene but toluene and
xylene a CR_{CH_4} of about 91.9% is achieved. The impact of the volume flow will be
discussed in more detail in Section 7.1.2.

The reduced methane conversion must have an effect on the *OCV* as well since the
equilibrium concentration is obviously not reached. To estimate this effect the Nernst
voltage of "synGas" depending on the methane and naphthalene concentration is cal-
culated. The inhibited methane conversion according to Equation 6.6 is considered.
Then ΔV_N (see Figure 6.16) is built by subtracting the Nernst voltage at a certain
naphthalene concentration from the Nernst voltage at 0 ppm naphthalene.

$$\Delta V_N = V_{N,x_{C_{10}H_8}>0\,\mathrm{ppm}} - V_{N,x_{C_{10}H_8}=0\,\mathrm{ppm}} \tag{6.7}$$
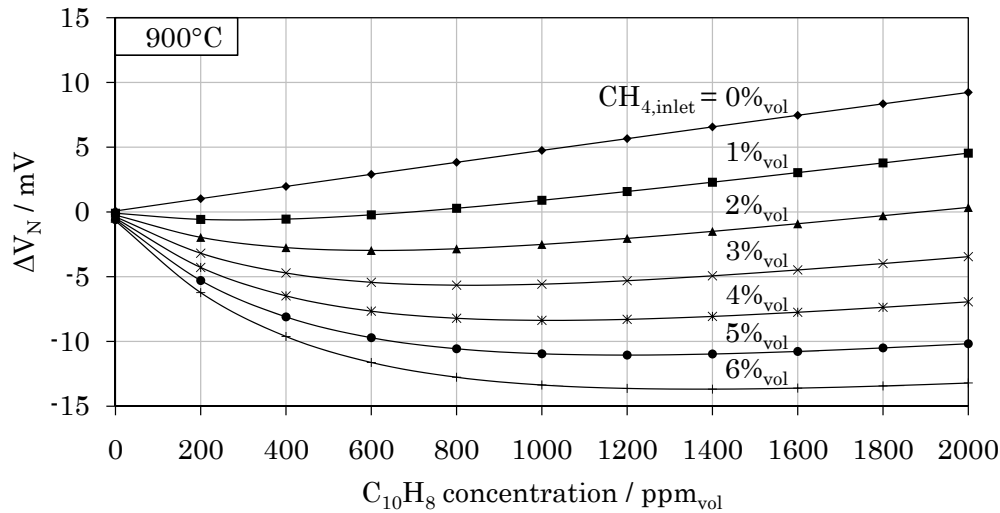
Figure 6.16: Change of Nernst voltage ΔV_N depending on the naphthalene concentration for the operation with "synGas" (20.3 % H_2, 13.0 % CO, 13.0 % CO_2, 28.8 % H_2O, balance N_2) at 900 °C. The methane content is varied between 0 and 6 % and balanced with N_2.

ΔV_N consists basically of two parts. On the one hand, there is the positive contribution from naphthalene due to its heating value. On the other hand, there is the negative contribution due to the inhibited methane conversion cause by naphthalene.

Figure 6.16 shows that the more methane is in the inlet gas mixture the more ΔV_N is influenced negatively. This is because the absolute percentage of methane which cannot be converted due to naphthalene, increases the higher the methane inlet concentration is.

The same behaviour for the *OCV* depending on the naphthalene concentration is shown in Figure 6.17. The measured data (solid, filled points) is compared to what is expected from equilibrium (dashed, blank points). For the equilibrium calculation an inhibited methane conversion is considered by using the fit curve shown in Equation 6.6. The reduced amount of methane at higher naphthalene concentrations is balanced with N_2. This way the amount of methane which is unconverted is considered to be inert and does not contribute to the Nernst voltage. Naphthalene on the other hand is considered to be converted completely for the calculation.

It can be seen that for all three gas compositions the *OCV* curve follows the equilibrium trend. However, an offset is observed leaving the equilibrium curve 5 to 10 mV above. This may originate from inaccuracies of the gas measurement or the water content on which the equilibrium calculation is based on.
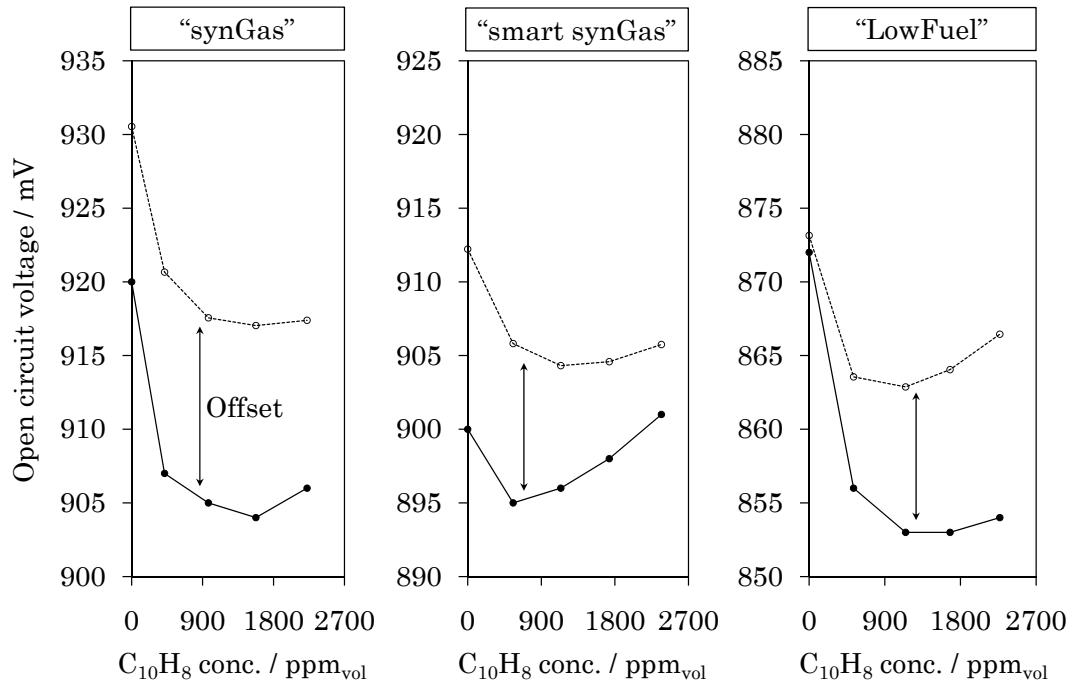
Figure 6.17: Measured (solid) and equilibrium (dashed) *OCV* of synthetic wood gas with naphthalene at 900 °C.

Figure 6.18 compares *OCV* measurements for synthetic wood gas compositions. The upper curves (blank points) are the results for synthetic wood gas containing toluene and xylene (besides naphthalene). The bottom curves are without toluene and xylene (filled points) and are therefore similar to those in Figure 6.17. The trend between the two respective curves is similar. As assumed from the CR_{CH_4} curve in Figure 6.15 toluene and xylene do not have any impact on the methane conversion. The curves with toluene and xylene are located at slightly higher *OCVs* as can be expected. Obviously the conversion of toluene and xylene is hardly affected by naphthalene because the voltage increase between the two curves stays fairly constant even for higher naphthalene concentrations. If the conversion of toluene and xylene would be affected in the same way as methane this voltage increase would have to diminish.
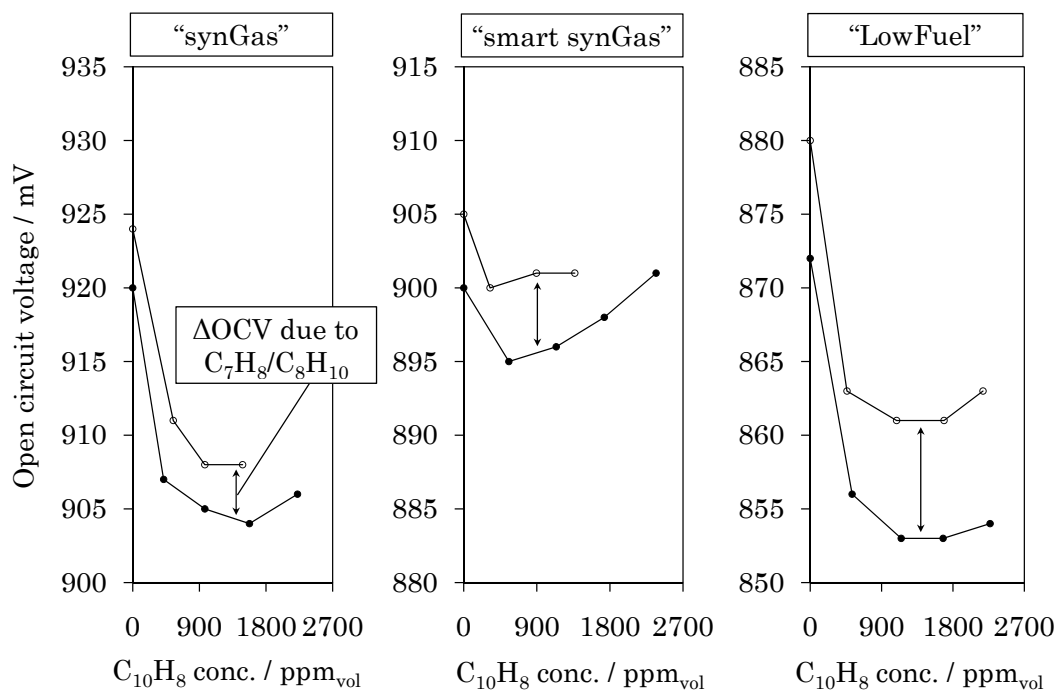
Figure 6.18: *OCV* of synthetic wood gas containing naphthalene with (blank points) and without (filled points) toluene/xylene at 900 °C.

6.7 Transient operation mode

The results discussed in Sections 6.3 - 6.6 are based on stable operating conditions. However, as for many heterogeneous catalytic processes the conversion of reactants shows a transient behaviour during start-up. In the beginning the fresh catalyst surface is free of any adsorbed reactants, intermediates or products. The longer the catalyst is in operation the more surface will be covered if there is a rate limiting step. On the other hand the amount of desorbed products will increase the higher the surface coverage is. Depending on the rate limiting steps the surface may be blocked due to the strong adsorption of either the reactant, intermediate or product. Therefore the transient behaviour lasts until an equilibrium flow between the adsorbing reactants on the surface and the desorbing products from the surface is reached. The following results in Section 6.7.1 and Section 6.7.2 are part of a paper from Hauth et al. [49].
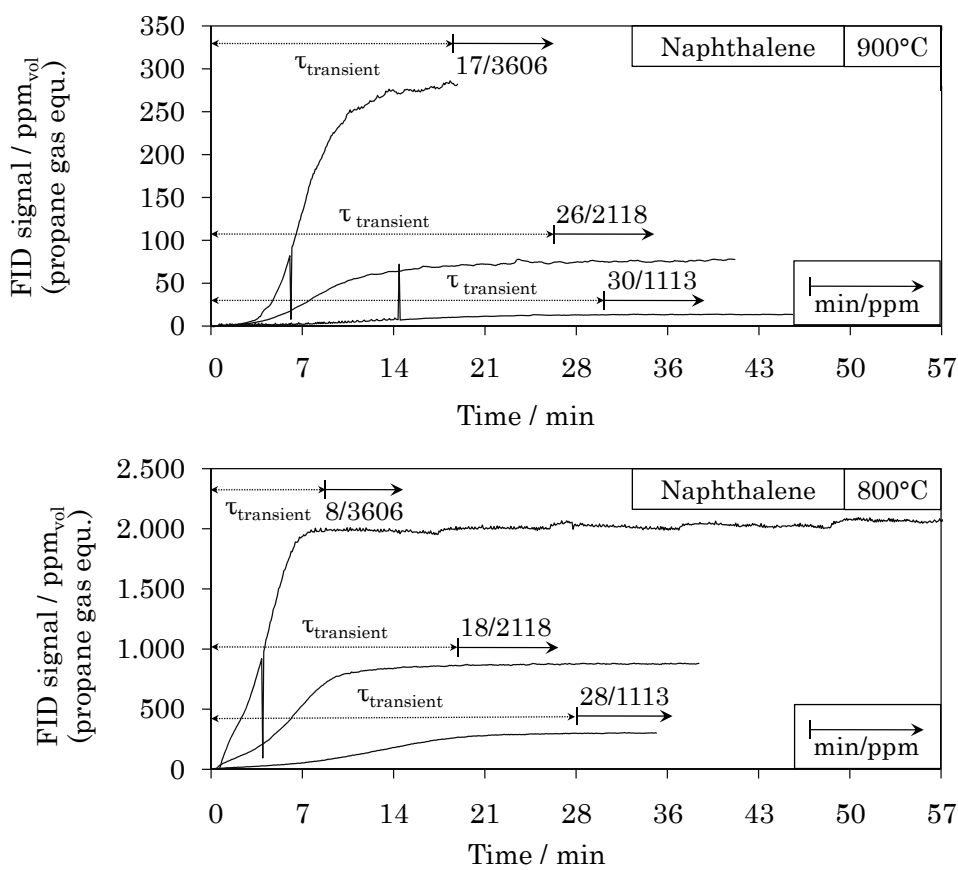
111

Figure 6.19: FID signal for the operation with diluted hydrogen (23.3 % H_2, 19.5 % H_2O, balance N_2) and a varying $C_{10}H_8$ concentration (1113, 2118 and 3606 ppm) at 800 (bottom) and 900 °C (top).

6.7.1 Transient response of the conversion rate of naphthalene, toluene and xylene

The first set of experiments comprises the transient response of the conversion rate of $C_{10}H_8$, C_7H_8 and C_8H_{10}. Therefore the in- and outlet concentration is measured with the FID in order to determine the conversion rate of hydrocarbons that are converted in the anode chamber as defined in Equation 4.38. The hydrocarbons are mainly converted due to steam reforming and the following shift reaction step.

Figure 6.19 shows the results for diluted hydrogen with either 1113, 2118 and 3606 ppm $C_{10}H_8$ at 800 and 900 °C. The addition of $C_{10}H_8$ begins at 0 min. The numbers below the arrows in the graphs indicate the approximate time until steady conversion
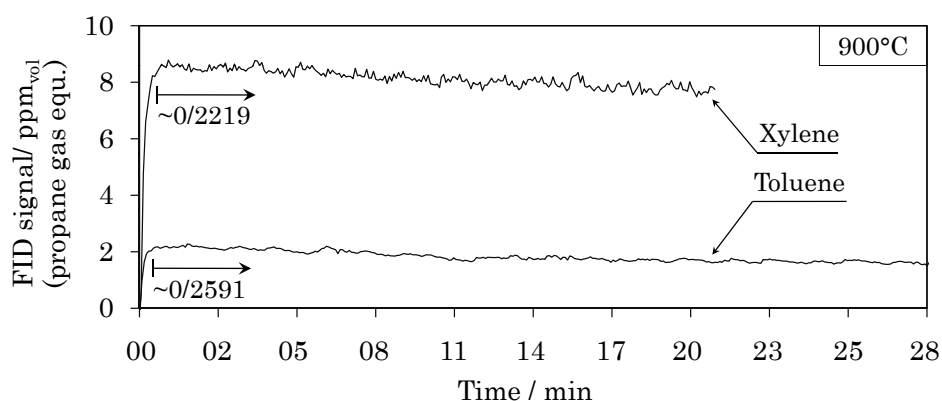
Figure 6.20: FID signal for the operation with diluted hydrogen (23.3 % H_2, 19.5 % H_2O, balance N_2) with either 2219 ppm C_8H_{10} or 2591 ppm C_7H_8 at 900 °C.

is achieved and the inlet concentration of naphthalene in *ppm*. The outlet concentration given in propane gas equivalence must not be compared quantitatively with the indicated inlet concentration. To obtain the real C_xH_y concentration the FID signal must be divided approximately by 3 (exact conversion see Section 5.3.2). However, the intention of the graphs is to allow a qualitative analysis of the conversion rate. Relatively little $C_{10}H_8$ is converted the higher the inlet concentration is. Nevertheless, the cell is capable to utilise amounts of naphthalene that are typical for fluidised bed steam gasification (< 500 ppm $C_{10}H_8$ [58]). Moreover, it can be seen that the transient response time TRT until steady conversion is reached is higher at low concentrations. The same experiment at 800 °C shows much lower conversion rates and slightly lower $TRTs$. It can be excluded that the TRT arises from a delay of the gas stream because measurements at the cell inlet show an immediate increase upon $C_{10}H_8$ addition.

Tests with C_7H_8 and C_8H_{10} show a similar conversion behaviour as $C_{10}H_8$ regarding the dependency on the temperature and inlet concentration. However, the conversion rate for C_7H_8 and C_8H_{10} is much higher and can be assumed almost 100 % for the inlet concentration as shown in Figure 6.20. Analysing the TRT suggests that steady conversion is achieved immediately after the addition of toluene or xylene.

In order to check whether the individual conversion rates can be achieved as well for the simultaneous use of C_7H_8, C_8H_{10} and $C_{10}H_8$ a test is shown in Figure 6.21 where these hydrocarbons are added consecutively. Certain points are indicated with roman numerals and signify following procedure:

  I: start addition of 1274 ppm C_7H_8 (toluene)

113

II: start addition of 1085 ppm C_8H_{10} (xylene)

III: start addition of 1117 ppm $C_{10}H_8$ (naphthalene)

IV: stop addition C_8H_{10} (xylene)

V: stop addition of C_7H_8 (toluene)

VI: start addition of 1274 ppm C_7H_8 (toluene) and 1085 ppm C_8H_{10} (xylene)

VII: stop addition $C_{10}H_8$ (naphthalene)

Between I and II the conversion rate for C_7H_8 is similar to the one as obtained from tests before (compare with Figure 6.20). After starting the addition of C_8H_{10} (II) the outlet concentration increases. The total conversion rate of C_7H_8 and C_8H_{10} is approximately the sum of the two individual conversion rates. As soon as $C_{10}H_8$ is added (III) a significant increase of the outlet concentration is observed. Comparing the FID signal (≈ 144 ppm) with the sum of the individual signals (C_7H_8: ≈ 2 ppm, C_8H_{10}: ≈ 4 ppm, $C_{10}H_8$: ≈ 12 ppm) as obtained from the single tar experiments with similar inlet concentration leads to a lower total conversion rate for the hydrocarbon mix as can be expected from single tar tests. A similar transient response of the outlet concentration is achieved as in the tests described in Figure 6.19. This suggests that $C_{10}H_8$ inhibits part of the conversion of C_7H_8 and C_8H_{10}. The TRT for a test with 1113 ppm $C_{10}H_8$ takes around 30 min. Figure 6.21 shows that the TRT for the hydrocarbon mix including 1117 ppm $C_{10}H_8$ is approximately 60 min. However, it is difficult to determine exactly when the conversion rate is stabilised. During the period where the FID signal stays constant at 100 ppm the FID is temporarily out of measurement range. In point IV the addition of C_8H_{10} is stopped resulting in an outlet concentration of about 53 ppm still above the sum of the individual concentrations. After stopping the addition of C_7H_8 (V) the FID signal drops down to 9 ppm which is approximately the same as obtained from the single $C_{10}H_8$ tests shown in Figure 6.19. Between VI and VII C_7H_8 and C_8H_{10} is added simultaneously to verify whether the result is reproducible. The outlet concentration settles at around 150 ppm which is close to what is achieved between III and IV. At VII the addition of $C_{10}H_8$ is stopped. The FID signal drops very slowly, different to what is observed after stopping the supply of C_7H_8 or C_8H_{10}. The behaviour is rather similar to the effect obtained when $C_{10}H_8$ addition is started. Therefore slow desorption of $C_{10}H_8$ is assumed which causes the conversion of C_7H_8 or C_8H_{10} to increase at the same pace. Maximum conversion of these two hydrocarbons is achieved after 90 min suggesting a slower desorption compared to the adsorption characteristic at these operating conditions.

Likewise the OCV can be analysed. Steam reforming of hydrocarbons and the following shift reaction increase the H_2 and CO content which eventually leads to an increase of the theoretical Nernst voltage or in this case of the OCV. This phenomenon is described for $C_{10}H_8$ in Section 6.3. The voltage increase is clearly visible after each additional hydrocarbon that is added and occurs immediately after the addition, even for the case of $C_{10}H_8$. One could assume that the characteristic of the voltage in-
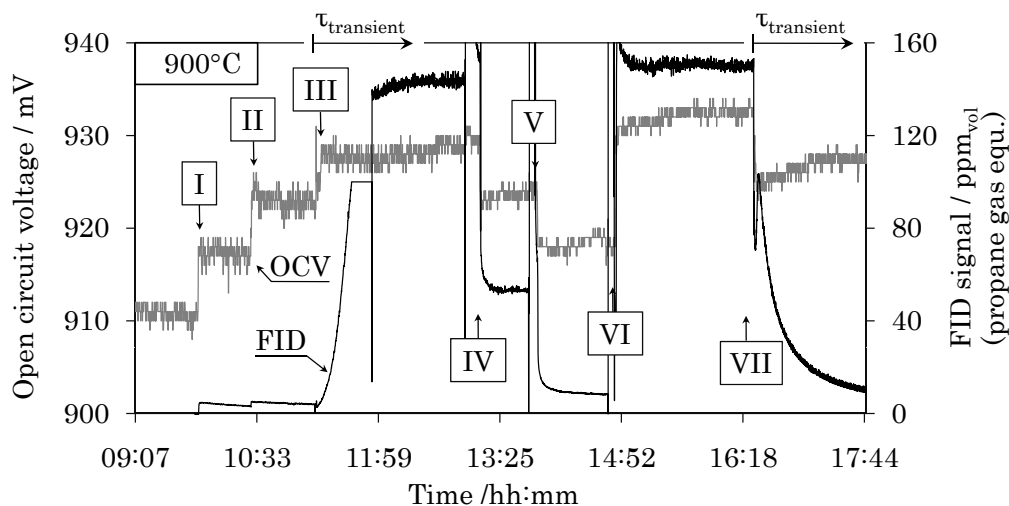
Figure 6.21: *OCV* and FID signal for the operation with diluted hydrogen (23.3 % H_2, 19.5 % H_2O, balance N_2), 1117 ppm $C_{10}H_8$, 1085 ppm C_8H_{10} and 1274 ppm C_7H_8 at 900 °C.

crease is coupled to the transient response of the conversion rate. However, a constant voltage signal is obtained during the period where the outlet concentration increases. According to this, the voltage signal is supposed to drop and stay constant in the same way when $C_{10}H_8$ addition is stopped (see Figure 6.21, VII). But as it can be seen the voltage first drops significantly followed by a slow increase until the voltage becomes constant. The time until a constant voltage signal is achieved approximately lasts as long as the TRT of the FID signal. This effect can be seen even better with $CH_4/C_{10}H_8$ mixtures as shown in Figure 6.22.

6.7.2 Transient response of the OCV for synthetic wood gas upon tar addition

Figure 6.22 shows the results for the *OCV* and the CH_4 outlet concentration from a test with "synGas" (see Table 6.6). The synthetic wood gas contains 606 ppm C_8H_{10} and 721 ppm C_7H_8 from the beginning while the $C_{10}H_8$ content is increased stepwise from 0 up to 1483 ppm. The parts highlighted with "inlet" and "no GA" indicate the period where either the inlet concentration is measured or no CH_4 measurement is carried out. During these periods the voltage signal is not suitable for comparison because the volume flow through the anode chamber may be different.

Before the addition of 547 ppm $C_{10}H_8$ (I) the CH_4 outlet concentration is approximately 0 %. The same way as the FID signal increases upon $C_{10}H_8$ addition, as
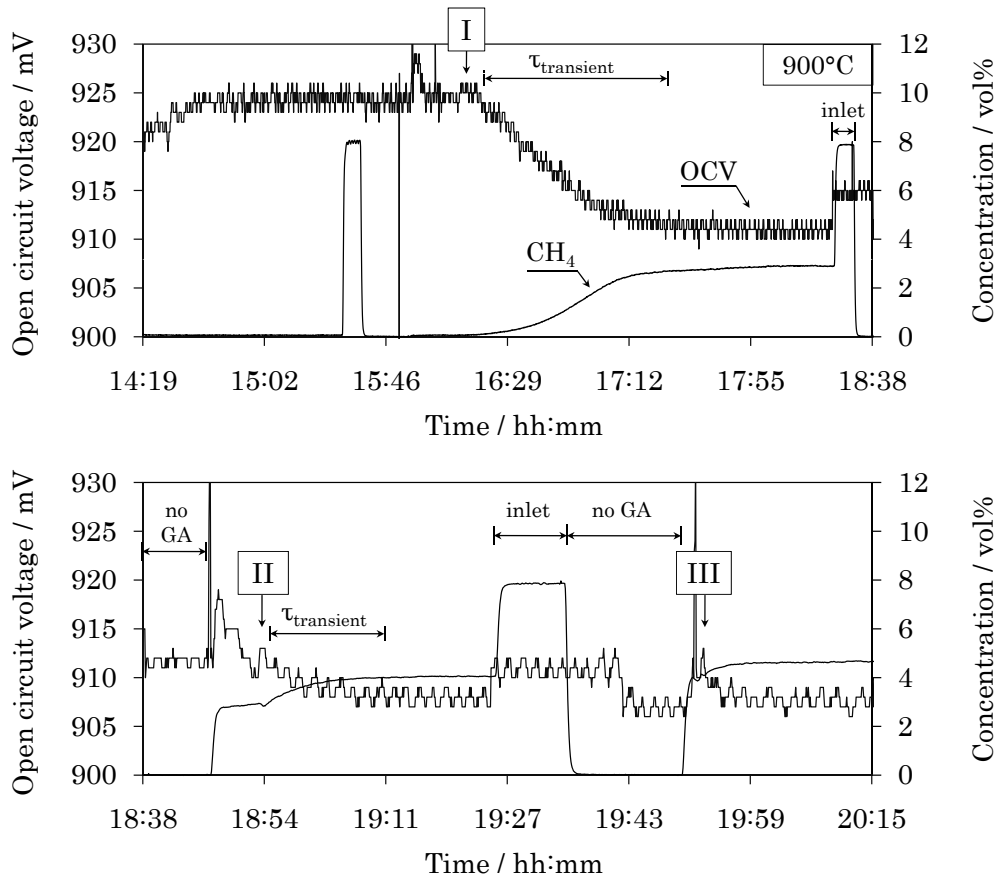
Figure 6.22: *OCV* and *CH_4* outlet concentration for the operation with "synGas" (20.8 % H_2, 13.3 % CO, 13.3 % CO_2, 6.3 % CH_4, 26.8 % H_2O, balance N_2), 606 ppm C_8H_{10}, 721 ppm C_7H_8 and a varying $C_{10}H_8$ concentration (0, 547, 974 and 1483 ppm) at 900 °C.

shown after point III in Figure 6.21, the CH_4 outlet concentration increases as soon as $C_{10}H_8$ is added. The TRT is close to that observed in tests before. In this case the voltage drops slowly in the same way as the CH_4 signal increases. One reason for the different behaviour as seen before with the $C_7H_8/C_8H_{10}/C_{10}H_8$ mix, where the voltage increases immediately after $C_{10}H_8$ addition, may be that the inhibition of the CH_4 conversion and the following reduced production of H_2 and CO influence the OCV more significantly. The reduction of the OCV, due to the inhibition of the CH_4 conversion, is higher as the increase caused by $C_{10}H_8$ conversion. This seems to be obvious as in this test the methane concentration is significantly higher compared to C_7H_8 and C_8H_{10} in Figure 6.21. The $C_{10}H_8$ concentration is further increased up

to 974 (II) and 1483 ppm (III) respectively. The OCV decreases each time, however, the drop is minor compared to the situation after $C_{10}H_8$ is added the first time (I). At least for II the TRT is still visible.

The desorption effect observed in Figure 6.21 (VII) is supported by the curve shown in Figure 6.13. Synthetic wood gas is tested with 2032 ppm $C_{10}H_8$. At point I the $C_{10}H_8$ addition is stopped leading to a sudden voltage drop. The anode surface is still assumed to be adsorbed with $C_{10}H_8$ which slowly desorbs from the active sites and enables a higher CH_4 conversion rate. Looking at the CH_4 outlet concentration supports this assumption. The curve shows another drop of the voltage where the current density is increased temporarily from 0 to 180 mA/cm². Interestingly this does not affect the methane outlet concentration. Apparently the desorption of $C_{10}H_8$ as well as the conversion of CH_4 is not influenced by the elevated current density.

Chapter 7

Development of tar measuring principle

7.1 Development of 2-cell-reformer concept

Based on the prior results the concept of a 2-cell-reformer tar sensor is developed and presented in this chapter. The scheme of the concept is shown in Figure 7.1. The idea is to direct the wood gas into the first measuring cell (cell:1). The cells require a gas cleaning of the wood gas prior entry. In cell:1 the hydrocarbons are converted as described in Chapter 6. Any present naphthalene will inhibit the conversion of methane and therefore the OCV will differ from what is thermodynamically expected. A conversion rate CR_{CH_4} similar to Equation 6.6 will be achieved. Hence, the anode off gas from cell:1 still contains methane and other hydrocarbons. This gas composition is still different from the equilibrium concentration. In the next step this anode off gas enters a reforming reactor filled with a Rh-catalyst that is designed for steam reforming of hydrocarbons. When the gas leaves the reforming reactor it is assumed to be in equilibrium. Consequently the OCV in cell:2 should match the theoretical Nernst voltage.

Both cells will be operated at open circuit conditions. An operation under electrical load may not be advantageous due to degradation effects. The operating temperature is set to 900 °C. As a constraint for this concept the theoretical OCV ($\equiv$Nernst voltage) based on gas analysis of the inlet gas composition including the H_2O content is said to be known. This is the OCV which would theoretically be achieved from the wood gas without any hydrocarbon species except methane - in other words a clean wood gas where the tar species are removed.

7.1.1 Reformer test

The reformer shown in Figure 7.1 enables complete conversion of hydrocarbons within the wood gas by steam reforming. A Rh-catalyst with good reforming properties is used at 900 °C to convert not only methane but also naphthalene, toluene and xylene into H_2 and CO. Substantial reforming tests with this catalyst material are carried out in [74]. In order to verify whether the reformer can manage the hydrocarbon load during operation the "synGas" mixture shown in Table 6.6 is tested in the reformer. The
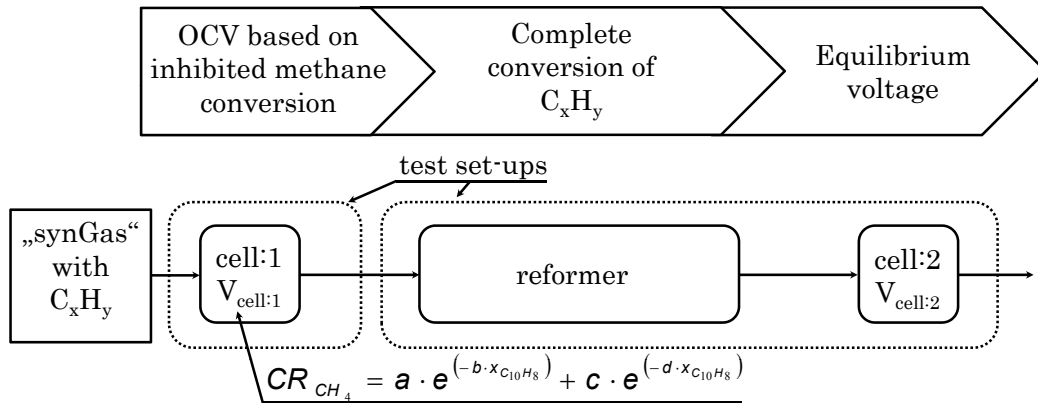
Figure 7.1: 2-cell-reformer concept of tar sensor.

individual tar concentration of naphthalene, toluene and xylene is ≈ 1000 ppm. The reformer outlet concentration is monitored with the FID. The volume flow through the reformer is ≈ 240 Nml/min. The FID measures nearly no hydrocarbons (≈ 10 ppm) at the reformer outlet suggesting complete reforming. During the one-day test no degradation of the catalyst material is observed. Since the volume flow through the reformer will be significantly lower ($\approx \frac{1}{10}$) this short-term test is sufficient to ensure stable conversion during the following sensor prototype tests.

7.1.2 Single sensor tests

First, the new design of the measuring cell as described in Section 5.1.2 is proven. Therefore the intention is to carry out a two-step test procedure (see test-setups in Figure 7.1). At the beginning only cell:1 without using the reformer and without cell:2 is simulated. This corresponds to position 1 ("reformer bypass mode") according to Figure 7.2. This step allows the determination of the conversion rate of methane depending on the volume flow. The volume flow is altered between ≈ 20 - 200 Nml/min. The three synthetic gas compositions from Table 6.6 without naphthalene, xylene and toluene are supplied to cell:1 at $900\,°C$. As in the tests with the $10\text{x}10\,\text{cm}^2$ planar cell the outlet concentration after cell:1 will be monitored by the GA. Afterwards the reformer/cell:2 arrangement (corresponds to position 2 in Figure 7.2) without cell:1 is used to examine whether the conversion of methane at the cell:2 outlet is complete. Then these two tests are compared regarding the OCV. Since the gas composition in cell:2 is close to equilibrium, unlike in cell:1, the OCV is expected to be significantly higher.

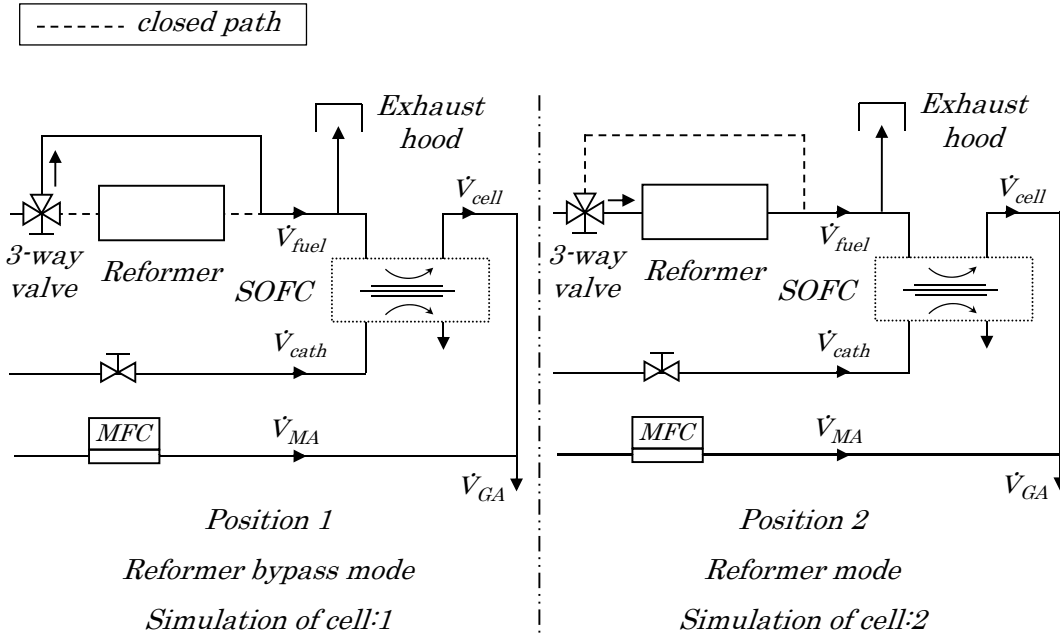Figure 7.3 shows the result of the conversion rate CR_{CH_4} depending on the volume

Figure 7.2: Scheme of prototype sensor test rig for the simulation of cell:1 (left) or cell:2 (right).

flow ratio $r_{\dot{V}}$. The volume flow ratio is defined as,

$$r_{\dot{V}} = \frac{\dot{V}_{cell}}{\dot{V}_{GA}} \tag{7.1}$$

where $\dot{V}_{cell}$ and $\dot{V}_{GA}$ are the volume flows through the cell and to the GA respectively (see Figure 5.3). $\dot{V}_{GA}$ is $\approx 200\,\mathrm{ml/min}$. The methane conversion significantly depends on the volume flow and reaches complete conversion only at a very low $r_{\dot{V}}$. This is a very important parameter in order to compare the results with those from the planar 10x10 cm^2 cell. For the planar 10x10 cm^2 cell it can be seen from Figure 6.15 that CR_{CH_4} is close to 100 % for operation without naphthalene. To achieve a similar conversion behaviour regarding the competing catalytic reactions between naphthalene and other hydrocarbons a volume flow is looked for where CR_{CH_4} for operation without naphthalene is close to 100 % as well. If this is achieved it is supposed that a similar dependency of CR_{CH_4} as for the tests for the planar 10x10 cm^2 cell can be anticipated.

The fit curve in Figure 7.3 demonstrates the volume flow dependency of CR_{CH_4} and includes all data points in the diagram except the two outliers from the tests with "smartsynGas".
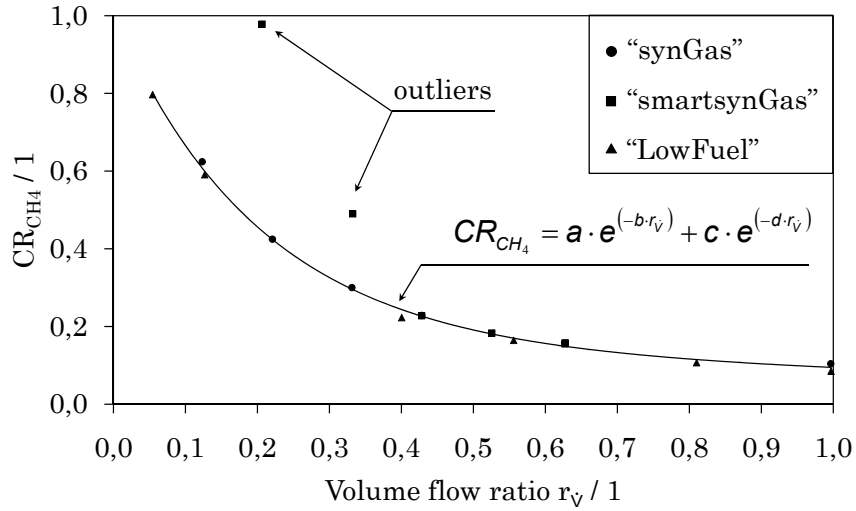
Figure 7.3: Methane conversion rate of cell:1 depending on the anode flow for three different synthetic wood gas compositions at 900 °C without additional hydrocarbons (fit curve parameters: $a = 0.8383$, $b = 4.9853$, $c = 0.1669$, $d = 0.6308$).

$$CR_{CH_4} = a \cdot e^{-b \cdot r_{\dot{V}}} + c \cdot e^{-d \cdot r_{\dot{V}}} \tag{7.2}$$

The parameters of the fit curve are: a=0.8383, b=4.9853, c=0.1669, d=0.6308.

The volume flow directly influences the open circuit voltage $V_{cell:1}$ of cell:1. The lower the volume flow, the more methane is converted and the higher is $V_{cell:1}$. By contrast, cell:2 does not show any volume flow dependency. $V_{cell:2}$ of cell:2 stays constant in the measured volume flow range.

In Figure 7.4 the voltage difference $V_{cell:1 \mapsto 2}$ between cell:1 and cell:2 is drawn over CR_{CH_4} of cell:1 and further compared with the equilibrium. For the equilibrium calculation the partly incomplete methane conversion on cell:1 is taken into account. The voltage difference $V_{cell:1 \mapsto 2}$ decreases with increasing conversion rate of methane in cell:1. While the $V_{cell:2}$ stays between 920 and 922 mV for the whole volume flow range, $V_{cell:1}$ increases from 893 up to 905 mV with decreasing volume flow in the case of "synGas". For "LowFuel" $V_{cell:2}$ even stays constant at 874 mV while $V_{cell:1}$ changes between 841 and 866 mV. The equilibrium curve of the voltage difference exhibits the same trend as the measured curve for both "synGas" and "LowFuel". The theoretical voltage difference is $\approx$ 4 mV lower as the measured difference. However, it has to be said that the measurement of the $V_{cell:1}$ and $V_{cell:2}$ takes place on two different days with two different test set-up arrangements. This means that also the cell itself
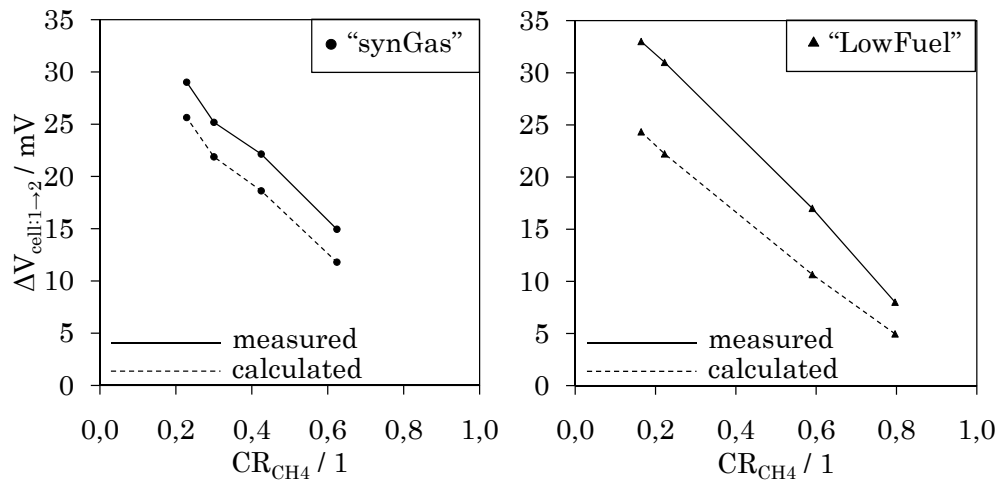
Figure 7.4: Voltage difference $\Delta V_{cell:1\mapsto 2}$ between cell:1 and cell:2 depending on the methane conversion rate at $900\,^{\circ}\mathrm{C}$ for synthetic wood gas without additional hydrocarbons (dashed: equilibrium, solid: measured).

changes between the tests. Therefore, it is conceivable that the measured difference includes a certain offset due to different testing conditions between the two tests which inevitably occur.

7.2 Tar measuring principle

For the following tests the test set-up as described in Figure 7.2 is used. As opposed to the tests explained in Section 7.1.2 it is possible to record the *OCV* for cell:1 ($V_{cell:1}$) and cell:2 ($V_{cell:2}$) including the reformer consecutively within the same measurement campaign without modifying the test set-up and changing the cell by using the 3-way-valve.

7.2.1 Measuring total tar load

In this section it is shown how the total tar load can be measured using only the reformer/cell:2 arrangement (according to measurements in position 2, see Figure 7.2). In this arrangement all hydrocarbons are converted in the reformer. Due to the reformer there is no transient behaviour as described in Section 6.7.2. Since an equilibrium gas composition is assumed, the open circuit voltage $V_{cell:2}$ can be compared with the Nernst voltage $V_{equ,C_x H_y,0}$, which is based on gas analysis (see upper graphs

in Figure 7.5). The left graph shows the measured values for the operation with tar and their fit curves whereas the right graph compares these fit curves (solid) with the theoretical equilibrium curves (dashed). Similar to Figure 6.4 the increase of the voltage due to the tar concentration is indicated in the bottom graphs of Figure 7.5. As can be seen an offset $\Delta V_{Offset} \approx 2.2$ mV between the theoretical and the measured value exists.

$$\Delta V_{Offset} = V_{equ,0} - V_{Base} \tag{7.3}$$

This offset can be considered by calibration of the sensor.

The base voltage V_{Base} is the voltage which would be achieved without any tar species. This voltage can not directly be measured by the sensor for a tar loaded sample gas because it is difficult to remove the tar species without changing the rest of the gas composition. For example, condensation of tar causes condensation of water as well. Therefore, it has to be calculated indirectly based on the gas inlet composition, temperature, pressure and voltage offset.

$$V_{Base} = f\left(x_{H_2},\, x_{CO},\, x_{CO_2},\, x_{CH_4},\, x_{N_2},\, x_{H_2O},\, T,\, p,\, \Delta V_{Offset}\right) \tag{7.4}$$

Then the difference ΔV_{tar} between the actual measured voltage $V_{cell:2}$ and the base voltage V_{Base} can be calculated.

$$\Delta V_{tar} = V_{cell:2} - V_{Base} \tag{7.5}$$
$$= V_{cell:2} - (V_{equ,0} - \Delta V_{Offset}) \tag{7.6}$$

The theoretical voltage difference ΔV_{equ} caused by the tar concentration can be calculated based on equilibrium considerations (see Figure 7.5, bottom left graph).

$$\Delta V_{equ} = V_{equ,C_xH_y,0} - V_{equ,0} \tag{7.7}$$

It can be seen that the measured ΔV_{tar} deviates slightly from the the theoretical ΔV_{equ}. This deviation is attributed to inaccuracies of the measurement. However, the trend of the curves proves that the correlation between the voltage increase and the tar concentration is feasible.

ΔV_{tar} and ΔV_{equ} can be drawn over the tar load in g/Nm³ on a wet basis as can be seen in Figure 7.6. In this figure the offset for the equilibrium curve is already considered. The volumetric concentration of the tar combinations (naphthalene, naphthalene/toluene/xylene) in *ppm* from Figure 7.5 are converted to g/Nm³ on a wet basis (see Table 7.1).
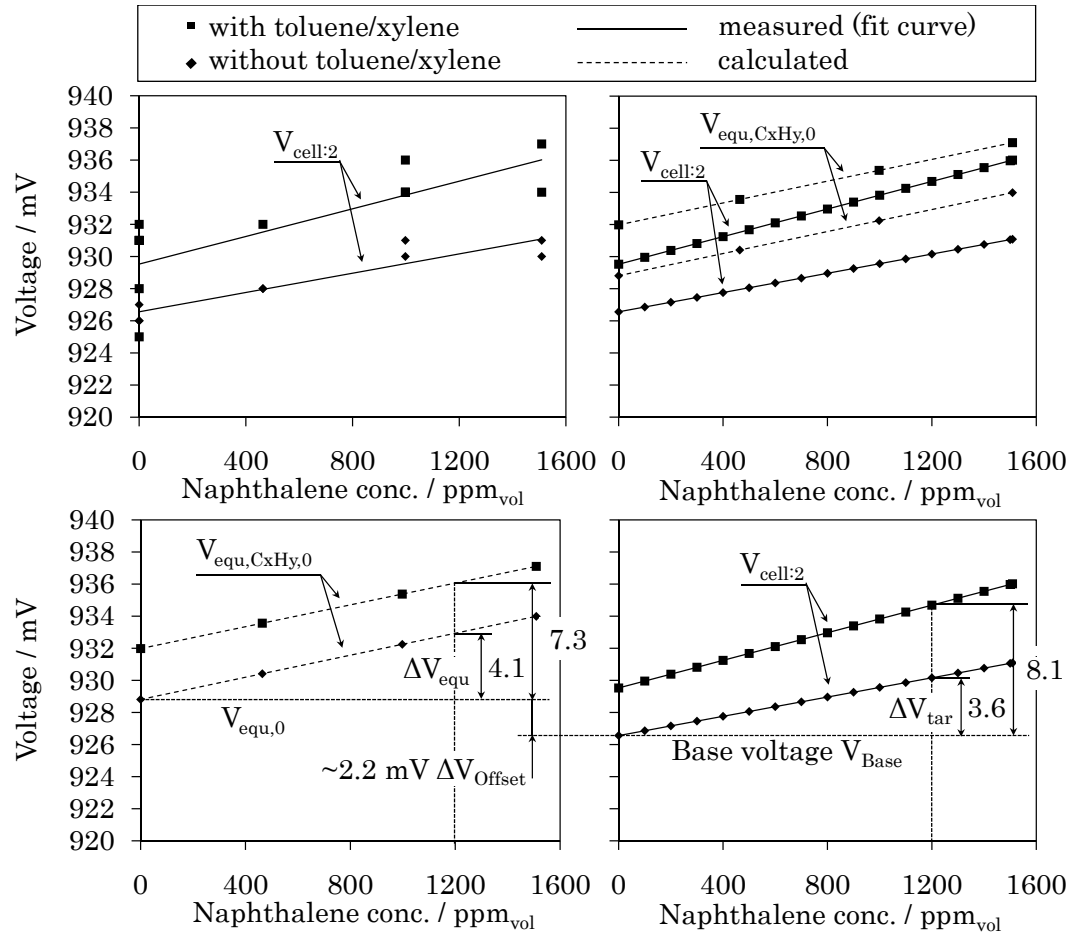
Figure 7.5: Upper graphs: Open circuit voltage (solid curves) and Nernst voltage (dashed curves) for the operation with "synGas" (compare with Table 6.6) and a varying tar concentration (naphthalene: 0/464/998/1509 ppm, toluene: 0/654 ppm, xylene: 0/523 ppm) at 900 °C. Bottom graphs: Comparison of ΔV_{tar} and ΔV_{equ} as an indication for the total tar concentration.

Table 7.1: Conversion of volumetric concentration in *ppm* to tar load in g/Nm³ on a wet basis

Tar species	x_i [*ppm*]	$w_{C_xH_y}$ [g/Nm³]
naphthalene	464	2.66
	998	5.71
	1509	8.63
toluene	654	2.69
xylene	523	2.48

125
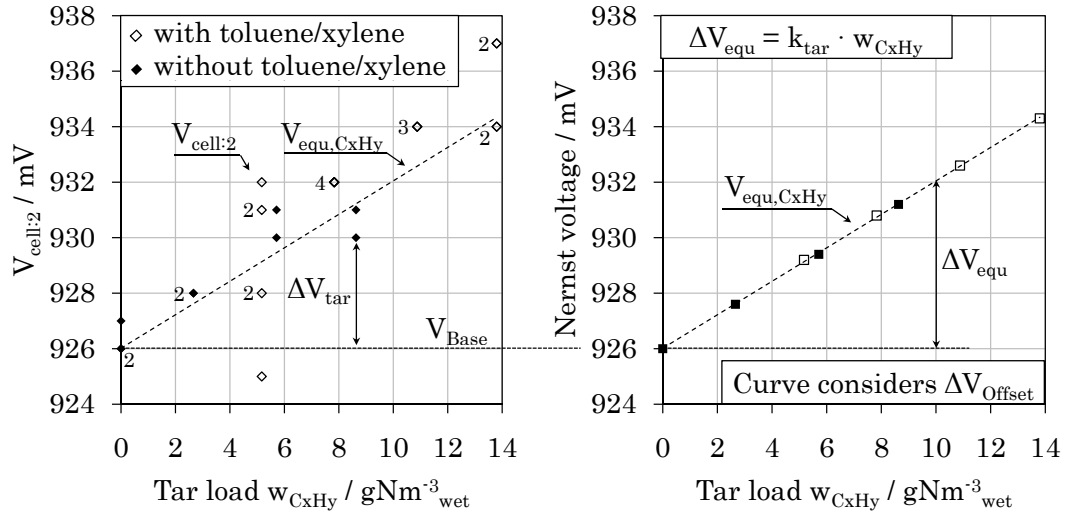
Figure 7.6: Voltage difference in mV due to the tar load in g/Nm³ on a wet basis. Left graph: Comparison of measured $V_{cell:2}$ and calculated V_{equ,C_xH_y}. Right graph: calculated Nernst voltages V_{equ,C_xH_y} (offset of 2.8 mV is considered).

As Figure 7.6 (right) shows, a linear correlation between V_{equ,C_xH_y} and the tar load can be found.

$$V_{equ,C_xH_y} = k_{tar} \cdot w_{C_xH_y} + V_{Base} \tag{7.8}$$

The tar load $w_{C_xH_y}$ is in g/Nm³ on a wet basis, V_{equ,C_xH_y} and V_{Base} in mV. The slope k_{tar} is given in (Nm³·mV)/g. By transformation an equation for $w_{C_xH_y}$ depending on $\Delta V_{equ,C_xH_y}$ is found.

$$w_{C_xH_y} = \frac{V_{equ,C_xH_y} - V_{Base}}{k_{tar}} \tag{7.9}$$

$$= \frac{\Delta V_{equ}}{k_{tar}} \tag{7.10}$$

As can be seen in the left graph of Figure 7.6 the measured values for $V_{cell:2}$ are located along the theoretical curve for V_{equ,C_xH_y}. The numbers next to the measured values of $V_{cell:2}$ indicate if more than one measured value exists for this point. The main challenge during the tests is to maintain a constant gas composition. A gas composition which is in reality different compared to what is assumed from gas analysis influences

V_{equ,C_xH_y} significantly. Furthermore, it has to be mentioned that some of the measured values are measured on different days. In such a case it is difficult to ensure similar testing conditions for all measured values in terms of gas and tar composition and volume flow.

It can be noticed that the measured values for the operation with naphthalene, toluene and xylene deviate more from the equilibrium curve than the values for the operation with naphthalene only. This might be an indication that maintaining a constant tar mix with three tar species is more difficult and sometimes might not have been achieved during the tests. In this case the real tar load would have been different to what is expected.

By contrast, it is not assumed that a kinetic inhibition of the conversion of tar may be the reason for the difference since the reformer is installed before cell:2.

Due to this measurement result it is feasible to obtain the tar load by using ΔV_{tar} for the linear correlation shown in Equation 7.9.

$$w_{C_xH_y} = \frac{V_{cell:2} - V_{Base}}{k_{tar}} \tag{7.11}$$

$$= \frac{\Delta V_{tar}}{k_{tar}} \tag{7.12}$$

The slope k_{tar} can be determined by equilibrium calculations based on actual gas analysis.

$$k_{tar} = \frac{V_{equ,C_xH_y,0} - V_{equ,0}}{w_{C_xH_y}} \tag{7.13}$$

The slope k_{tar} depends not only on the gas composition but also on the tar species. The dependency on the tar species has already been shown in Figure 6.6. In order to illustrate these dependencies k_{tar} is calculated and shown in Table 7.2 for several gas compositions and tar species. The slope k_{tar} is similar for all listed tar species except phenol. This is because phenol is the only hydrocarbon containing an OH molecule. The additional oxygen generally reduces the Nernst voltage. Therefore a rough estimation of the ratio between non-alcoholic and alcoholic tar species beforehand is helpful to determine k_{tar} exactly. Less problematic is the dependency on the permanent gas composition since it is said to be known by gas analysis.

7.2.2 Distinguishing between certain tar species

In order to enable the sensor to distinguish between certain tar species the test-setup as described in Figure 7.1 including both cells (cell:1 and cell:2) and the reformer is used.

Table 7.2: Determination of k_{tar} for each tar species for the operation with "synGas", "smart synGas" and "LowFuel" (compare with Table 6.6) at $900\,°C$ and $0.98\,\text{bar}$. The "Range" column indicates for which tar load range the values for k_{tar} are valid

Tar species	Range g/Nm^3	"synGas"	"smart synGas"	"LowFuel"
naphthalene	0.0-17.2	0.595	0.617	0.734
xylene	0.0-16.6	0.607	0.633	0.759
toluene	0.0-16.5	0.604	0.630	0.755
phenol	0.0-16.8	0.445	0.469	0.570
benzene	0.0-17.4	0.600	0.624	0.744

Volume flow dependency of conversion rate

Figure 7.7 shows once more the volume flow dependency of the methane conversion rate and further of the open circuit voltage $V_{cell:1}$. In this case three different volume flows for "synGas" (compare with Table 6.6) without tar are tested while the 3-way-valve is turned into the reformer bypass mode (position 1, see Figure 7.2). From this data it is not clearly visible whether the dependency is linear or exponential. Difficulties arise when properly maintaining a constant low volume flow. Furthermore, inaccuracies emerge at low volume flows since $\dot{V}_{cell}$ and CR_{CH_4} are based on gas analysis where the diluted mixing air $\dot{V}_{MA}$ (see Figure 7.2) needs to be subtracted out. At a low $\dot{V}_{cell}$ a high $\dot{V}_{MA}$ is used which leads to a low methane concentration measured by the GA. Therefore, the determination of the original methane concentration at the anode outlet is automatically more inaccurate at a low $\dot{V}_{cell}$.

However, the intention is to find a low volume flow where the conversion rate is close to $100\,\%$. Eventually a volume flow $\dot{V}_{cell} \approx 40\,\text{ml/min}$ is chosen for further tests. Therefore, a CR_{CH_4} above $90\,\%$ without tar can be expected.

Dependency of conversion rate on tar concentration

In order to obtain the tar-dependent conversion rate CR_{CH_4} for cell:1, the "synGas" is tested first with additions of naphthalene (0, 464, 998, 1509 ppm). In a second run a constant load of toluene (654 ppm) and xylene (523 ppm) are additionally added. In Figure 7.8 (left) the measured data is shown and a fit curve is calculated. The triangles represent tests with toluene/xylene while the dashes stand for tests without toluene/xylene. The fit curve comprises both tests. The characteristic of the curve is similar to what is shown in Figure 6.15. It can be seen that CR_{CH_4} for 0 ppm naphthalene/toluene/xylene is in the same range as shown in Figure 7.7 at $40\,\text{ml/min}$. However, the measured values vary slightly which may partly be attributed to the fluctuating volume flow through the cell.
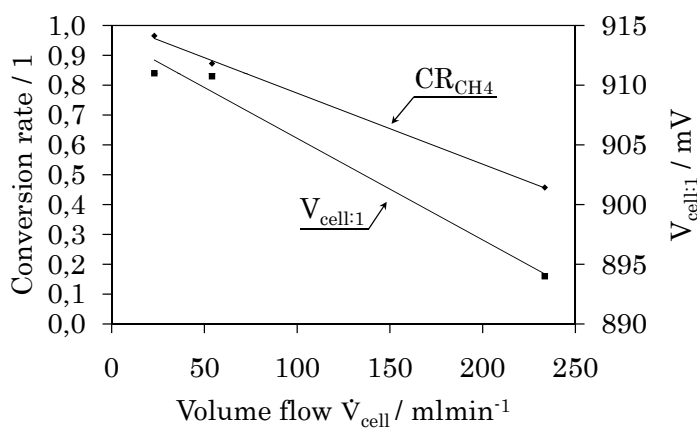
Figure 7.7: Conversion rate of methane and *OCV* depending on cell volume flow for "synGas" (20.3 % H_2, 13.0 % CO, 13.0 % CO_2, 6.2 % CH_4, 28.8 % H_2O, balance N_2) at 900 °C.
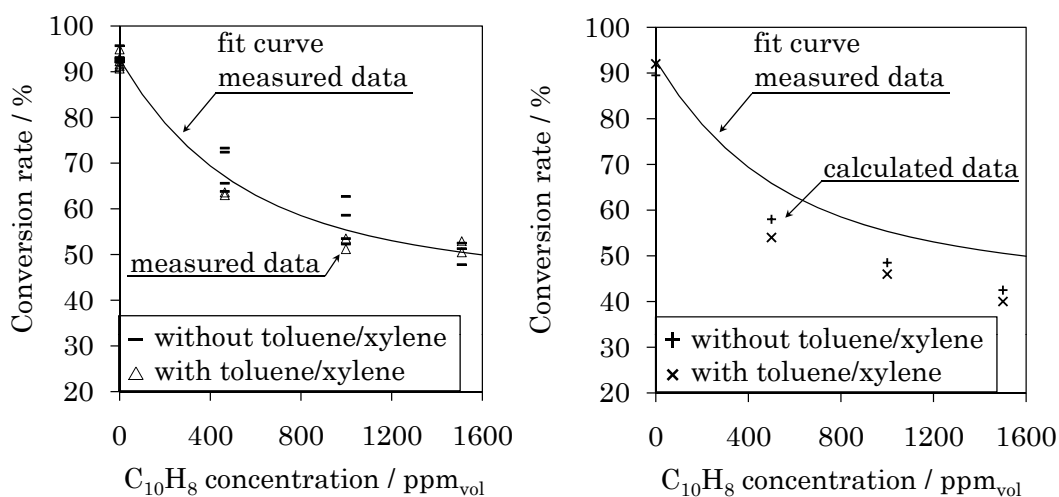

Figure 7.8: Left: Conversion rate of methane of cell:1 depending on naphthalene concentration for "synGas" (20.3 % H_2, 13.0 % CO, 13.0 % CO_2, 6.2 % CH_4, 28.8 % H_2O, balance N_2) and a varying concentration of $C_{10}H_8$ (0, 464, 998, 1509 ppm) at 900 °C and a volume flow $\dot{V}_{cell}$ of $\approx$ 40 ml/min. Triangles: 654 ppm toluene, 523 ppm xylene; dashes: no toluene/xylene. Right: Comparison of fit curve of measured data and calculated data.

129

Voltage difference between cell:1 and cell:2

Next, tests are performed where the 3-way-valve is switched back and forth from position 1 to position 2 (compare with Figure 7.2). Again, the "synGas" mixture is used while the naphthalene concentration is increased. Two sets of tests - with and without constant load of toluene/xylene - are carried out. The intention is to monitor the OCV of cell:1 ($V_{cell:1}$) and cell:2 ($V_{cell:2}$) consecutively for the same gas composition. This way the voltage difference $\Delta V_{cell:1 \mapsto 2}$ between cell:1 and cell:2 caused by the conversion of tar and the inhibition of methane conversion as described in Section 7.1 is measured.

$$\Delta V_{cell:1 \mapsto 2, naph} = V_{cell:2, naph} - V_{cell:1, naph} \tag{7.14}$$

$$\Delta V_{cell:1 \mapsto 2, naph+tol+xyl} = V_{cell:2, naph+tol+xyl} - V_{cell:1, naph+tol+xyl} \tag{7.15}$$

Figure 7.9 demonstrates the results of the two test series for cell:1 and cell:2. Both curves of $V_{cell:1}$ for the operation with ($V_{cell:1, naph+tol+xyl}$) and without toluene/xylene ($V_{cell:1, naph}$) show a similar trend. As expected $V_{cell:1}$ falls more the more naphthalene is added due to the inhibition of the methane conversion. Furthermore, the operation curve $V_{cell:1, naph+tol+xyl}$ with toluene/xylene is located 4-6 mV above $V_{cell:1, naph}$. This offset can clearly be attributed to toluene/xylene and is very similar to the voltage increase shown in Figure 6.4.

The hydrocarbons which still leave cell:1 will be converted completely in the reformer. Therefore, the equilibrium concentration is obtained in cell:2. The fit curves of the $V_{cell:2}$ confirm a linear increase with increasing naphthalene concentration. The same curves are described in more detail in Section 7.2.1 for the determination of the total tar load. For the case that toluene and xylene are added $V_{cell:2, naph+tol+xyl}$ is again located 4-6 mV above $V_{cell:2, naph}$ as for cell:1. This suggests that toluene and xylene are already completely converted in cell:1. Otherwise the difference $\Delta V_{cell:1, tol+xyl}$ would be expected to be higher than $\Delta V_{cell:2, tol+xyl}$.

$$\Delta V_{cell:1, tol+xyl} \approx \Delta V_{cell:2, tol+xyl} \tag{7.16}$$

In order to verify whether the assumptions made before to explain the trend of the measured curves are correct, a simulation of the Nernst voltage is carried out and compared with the fit curves for the measured values (see Figure 7.10). The calculation is based on the "synGas" composition. For the calculation of the two curves of cell:2 equilibrium is assumed which means that all hydrocarbons will be converted. The calculation of the two curves of cell:1 takes into account the conversion rate CR_{CH_4}. Naphthalene, toluene and xylene are assumed to be converted completely in cell:1.

In Figure 7.10 the fit curves of the measured values (solid curves) from Figure 7.9 and the calculated values (crosses, dashed curve) are put on top of each other. An offset
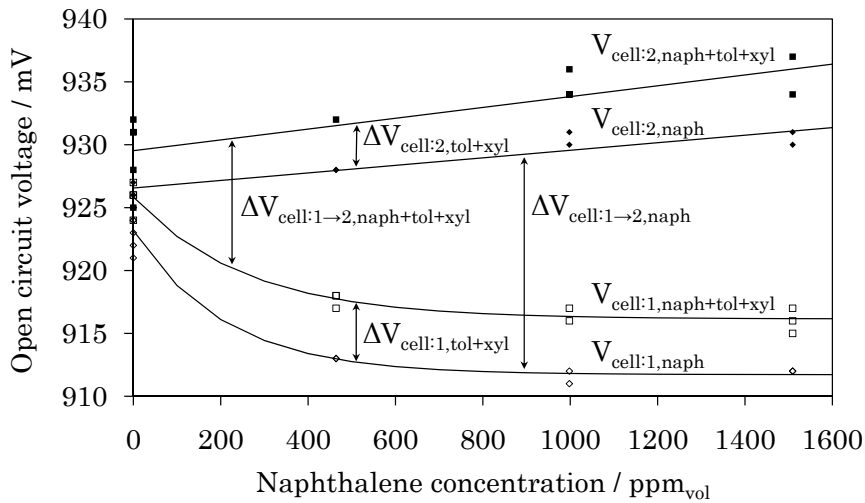
Figure 7.9: Measured $V_{cell:1}$ and $V_{cell:2}$ including fit curves of measuring principle for "synGas" at 900 °C. Squares: operation with 0/464/998/1509 ppm naphthalene, 654 ppm toluene and 523 ppm xylene. Diamonds: operation with 0/464/998/1509 ppm naphthalene.
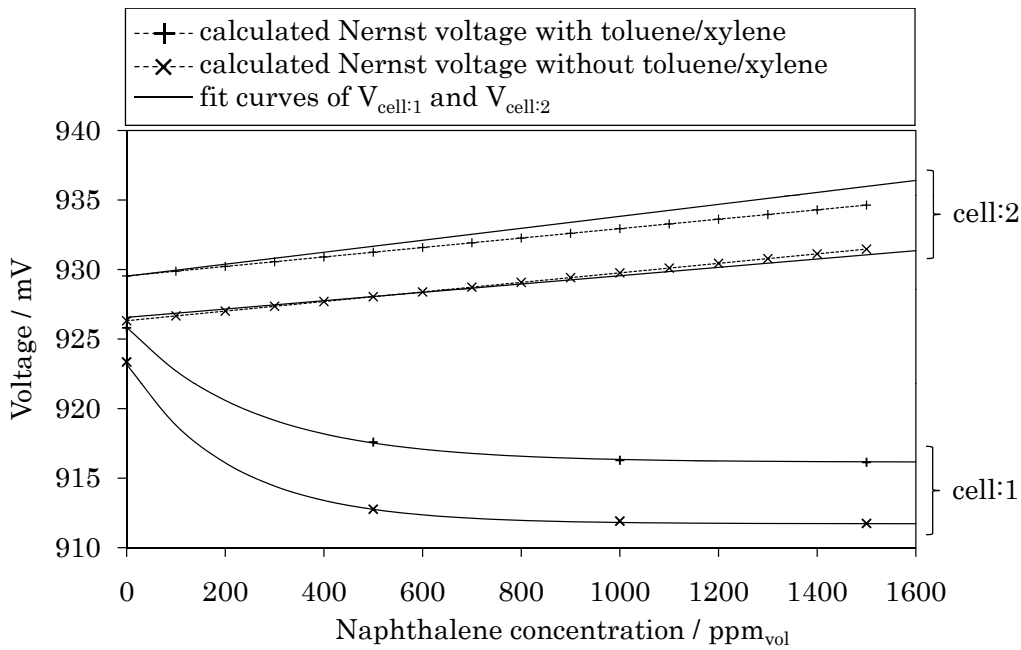

Figure 7.10: Comparison of Nernst voltage and fit curves for $V_{cell:1}$ and $V_{cell:2}$ of measuring principle for "synGas" at 900 °C.

of the calculated curves is compensated by subtracting ≈ 3 mV from the calculated Nernst voltages in order to eliminate the inaccuracy that occurs between the measured OCV and the Nernst voltage (compare with offset described in Section 7.2.1). In the calculation the methane conversion rate for cell:1 is adopted in order to match the measured values. This way it is verified whether the measured conversion rate is feasible. The adopted CR_{CH_4} is shown in Figure 7.8 (right, "calculated data"). It can be seen that the calculated and the measured CR_{CH_4} differ. The calculated CR_{CH_4} is $\approx 10\,\%$ points lower. One reason for this may be the inaccurate determination of the methane concentration at the anode outlet. If the methane concentration was higher in reality then the conversion rate would be lower and thus closer to the calculated points.

Figure 7.11 shows the voltage difference $\Delta V_{cell:1 \mapsto 2, naph}$ between cell:1 and cell:2 as obtained in Figure 7.9. The blank diamonds represent the fit curve for the operation without toluene/xylene while the filled squares stand for operation with toluene/xylene. $\Delta V_{cell:1 \mapsto 2, naph}$ is almost the same for both curves.

$$\Delta V_{cell:1 \mapsto 2, naph} \approx \Delta V_{cell:1 \mapsto 2, naph+tol+xyl} \tag{7.17}$$

The voltage difference between cell:1 and cell:2 correlates to the naphthalene concentration. Toluene and xylene do not seem to have a significant influence. The arrow indicates the concentration range of naphthalene where the measuring principle creates a voltage difference $\Delta V_{cell:1 \mapsto 2, naph}$ that increases significantly with increasing naphthalene concentration. This covers the concentration range of an allothermal steam gasifier as shown in Table 4.3.

Procedure to distinguish between certain tar species

In the end the sensor will provide two $OCVs$; one for cell:1 ($V_{cell:1}$) and one for cell:2 ($V_{cell:2}$). The following procedure explains how it can be distinguished between naphthalene and toluene/xylene.

Step 1: For this measuring principle the inlet composition of the permanent gases has to be known which means that a simultaneous gas analysis of these components is required (compare with Equation 7.4). From the permanent gas composition the theoretical curve of the voltage difference $\Delta V_{cell:1 \mapsto 2, equ}$ based on the methane conversion rate CR_{CH_4} can be calculated (see Figure 7.12). This requires a precise calibration of the sensor beforehand to obtain CR_{CH_4}.

Step 2: The measured voltage difference $\Delta V_{cell:1 \mapsto 2, naph}$ between cell:1 and cell:2 can be taken and compared with the curve calculated in step 1. As a result the naphthalene concentration is obtained (compare with Figure 7.12).

Step 3: From the permanent gas composition and the naphthalene concentration the Nernst voltage can be calculated for cell:1 and cell:2 and compared with the measured $V_{cell:1}$ and $V_{cell:2}$ (see Figure 7.13). The crosses exemplarily indicate possible measured values (upper cross = cell:2, bottom cross = cell:1). The distance between these two measured values corresponds to $\Delta V_{cell:1\mapsto2,naph}$ as obtained in step 2 and can be attributed to naphthalene. The dashed curves are calculated and based on gas analysis (upper curve = cell:2, bottom curve = cell:1).

In the case that toluene, xylene and naphthalene is present (Step 3a) the voltage difference $\Delta V_{cell:2,tol+xyl}$ between the Nernst voltage of cell:2 and the measured voltage $V_{cell:2}$ can be attributed to the sum of the toluene/xylene load. In the same way this voltage difference is observed between the Nernst voltage of cell:1 and the measured voltage $V_{cell:1}$. The voltage difference $\Delta V_{cell:2,naph}$ is the difference between the Nernst voltage of cell:2 without tar (complete methane conversion) and $V_{cell:2}$ with naphthalene. Therefore, this voltage difference can additionally be taken to determine the naphthalene concentration. The sum of $\Delta V_{cell:2,tol+xyl}$ and $\Delta V_{cell:2,naph}$ equal to ΔV_{tar} as introduced in Equation 7.5.

If only naphthalene is present (Step 3b) the Nernst voltage for cell:1/cell:2 and the measured values for $V_{cell:1}/V_{cell:2}$ match. $\Delta V_{cell:2,tol+xyl}$ is then zero.

In the case that only toluene and xylene are present (Step 3c) the voltage difference $\Delta V_{cell:1\mapsto2,naph}$ is lowest according to Figure 7.11. However, a difference between the Nernst voltage of cell:1/cell:2 and $V_{cell:1}/V_{cell:2}$ respectively will be observed which indicates the sum of the toluene and xylene concentration ($\Delta V_{cell:2,tol+xyl} = \Delta V_{cell:1,tol+xyl}$).

Results of measurement campaign

In Table 7.3 the mean values of the measurement campaign shown in Figure 7.9 are summarised.

It is possible to distinguish between naphthalene and toluene/xylene. A further distinction between toluene and xylene is not possible. According to Figure 7.12 following equation for the determination of $\Delta V_{cell:1\mapsto2,equ}$ can be found.

$$\Delta V_{cell:1\mapsto2,equ} = V_{cell:2,equ} - V_{cell:1,equ} \tag{7.18}$$

$V_{cell:1,equ}$ and $V_{cell:2,equ}$ can be calculated based on gas analysis and on the conversion rate CR_{CH_4} of cell:1 respectively.
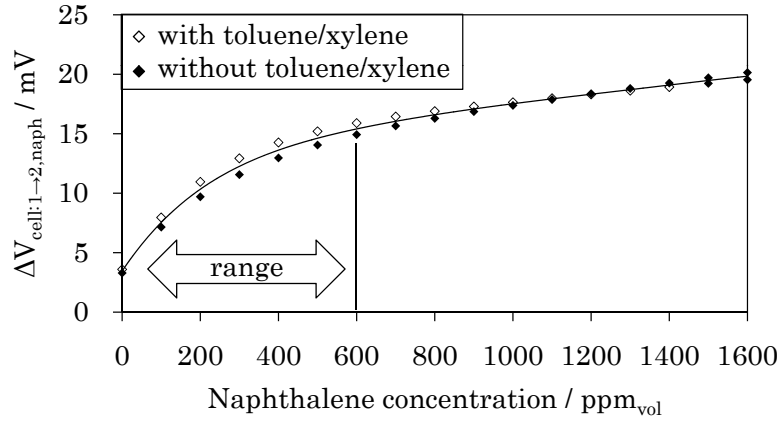
Figure 7.11: Voltage difference $\Delta V_{cell:1\mapsto2,naph}$ depending on naphthalene concentration at $900\,^{\circ}\text{C}$. The points are based on fit curves from the measured values for $V_{cell:1}$ and $V_{cell:2}$.

Table 7.3: Results of tar detection. $\Delta V_a = \Delta V_{cell:1\mapsto2,naph}$, $\Delta V_b = \Delta V_{cell:1,tol+xyl} = \Delta V_{cell:2,tol+xyl}$, $\Delta V_c = \Delta V_{cell:2,naph}$

			[ppm]	**[g/Nm³]**		**[ppm]**	**[g/Nm³]**
		C_7H_8	0	0.0	C_7H_8	654	2.7
		C_8H_{10}	0	0.0	C_8H_{10}	523	2.5
$C_{10}H_8$		ΔV_a	ΔV_b	ΔV_c	ΔV_a	ΔV_b	ΔV_c
[ppm]	**[g/Nm³]**	**[mV]**	**[mV]**	**[mV]**	**[mV]**	**[mV]**	**[mV]**
0	0.0	3.2	0.0	0.0	3.3	2.8	0.0
464	2.7	15.0	0.0	1.7	14.3	4.4	2.8
998	5.7	19.0	0.0	4.2	18.3	4.4	5.3
1509	8.6	18.5	0.0	4.2	19.3	4.6	6.3

$$V_{cell:1,equ} = f\left(x_i,\, x_{C_{10}H_8},\, T,\, p,\, \Delta V_{Offset},\, CR_{CH_4}\right) \tag{7.19}$$

$$V_{cell:2,equ} = f\left(x_i,\, x_{C_{10}H_8},\, T,\, p,\, \Delta V_{Offset}\right) \tag{7.20}$$

If $\Delta V_{cell:1\mapsto2,equ}$ over the naphthalene concentration is calculated by means of equilibrium calculations (as in Figure 7.12), an exponential fit curve can be generated.

$$\Delta V_{cell:1\mapsto2,equ} = v_{0,[ppm]} + a_{[ppm]} \cdot \left[1 - e^{\left(-b_{[ppm]}\cdot x_{C_{10}H_8}\right)}\right]$$
$$+ c_{[ppm]} \cdot \left[1 - e^{\left(-d_{[ppm]}\cdot x_{C_{10}H_8}\right)}\right] \tag{7.21}$$
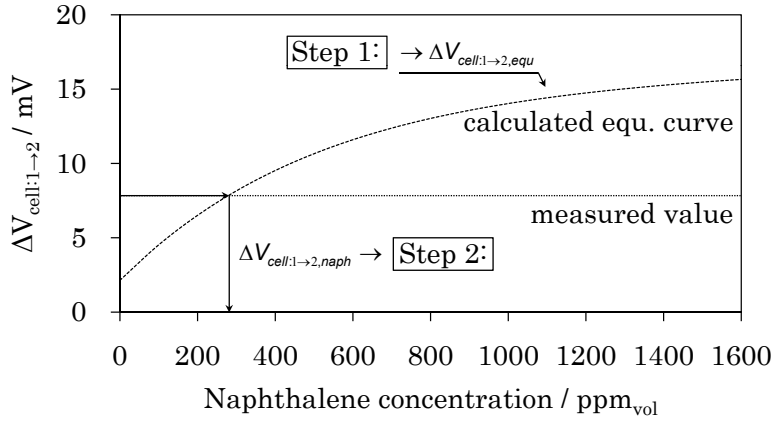
134

Figure 7.12: Step 1 and 2: Determination of naphthalene concentration (calculated equilibrium curve can be fitted according Equation 7.21).

The parameters $v_{0,[ppm]}$, $a_{[ppm]}$, $b_{[ppm]}$, $c_{[ppm]}$ and $d_{[ppm]}$ strongly depend on the conversion rate CR_{CH_4} as well as on the permanent gas composition. If $\Delta V_{cell:1\mapsto2,equ}$ is drawn over the naphthalene load in $\mathrm{g/Nm^3}$ on a wet basis then Equation 7.21 can be written as follows.

$$
\begin{aligned}
\Delta V_{cell:1\mapsto2,equ} =\;& v_{0,[\mathrm{g/Nm^3}]} + a_{[\mathrm{g/Nm^3}]} \cdot \left[1 - e^{\left(-b_{[\mathrm{g/Nm^3}]}\cdot w_{C_{10}H_8}\right)} \right] \\
& + c_{[\mathrm{g/Nm^3}]} \cdot \left[1 - e^{\left(-d_{[\mathrm{g/Nm^3}]}\cdot w_{C_{10}H_8}\right)} \right]
\end{aligned}
\tag{7.22}
$$

Then the fit curve parameters change to $v_{0,[\mathrm{g/Nm^3}]}$, $a_{[\mathrm{g/Nm^3}]}$, $b_{[\mathrm{g/Nm^3}]}$, $c_{[\mathrm{g/Nm^3}]}$ and $d_{[\mathrm{g/Nm^3}]}$. For a specific measured $\Delta V_{cell:1\mapsto2,naph}$ it can be said that,

$$
\Delta V_{cell:1\mapsto2,naph} = \Delta V_{cell:1\mapsto2,equ}
\tag{7.23}
$$

This way the naphthalene load in $\mathrm{g/Nm^3}$ on a wet basis can be calculated by transforming Equation 7.22.

$$
w_{C_{10}H_8} = w_0 + a_w \cdot e^{b_w \cdot \Delta V_{cell:1\mapsto2,naph}} + c_w \cdot e^{d_w \cdot \Delta V_{cell:1\mapsto2,naph}}
\tag{7.24}
$$

It is important to note that the fit curve parameters (w_0, a_w, b_w, c_w and d_w) are specific for a certain gas composition and are based on the methane conversion rate
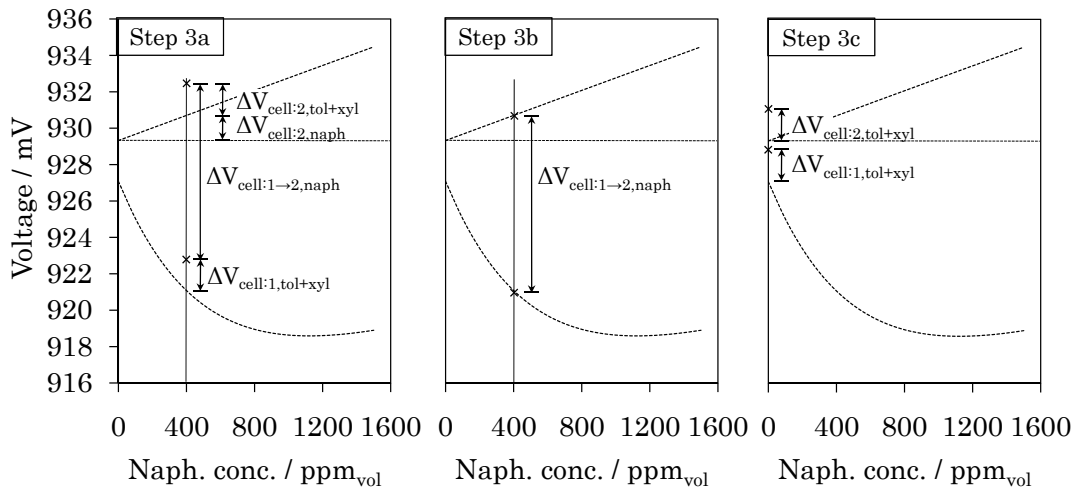
Figure 7.13: Step 3: Distinction of tar species.

CR_{CH_4} which itself depends on the naphthalene concentration and on the volume flow through the cell. Therefore, it is important to keep the volume flow constant in order to eliminate one dependency of the fit curve. However, for a changing permanent gas composition the fit curve parameters w_0 and a_w-d_w have to be determined continually based on online gas analysis.

Since the total tar load $w_{C_xH_y}$ can be determined according Equation 7.10 it is possible to find the rest of the tar load by subtraction.

$$w_{rest} = w_{C_xH_y} - w_{C_{10}H_8} \tag{7.25}$$

7.3 Further steps for real wood gas applications

Calibration

In order to allow a comparison of the absolute value of the Nernst voltage and the OCV a calibration of the sensor will be necessary in order to compensate the offset ΔV_{Offset} (see Figure 7.5). This offset origins mainly from leakages of the measuring cell and the inaccuracy of the gas analysis. Leakages change the gas composition at the anode, in particular the oxygen partial pressure and therefore influence the OCV. Inaccuracies of the gas analysis lead to a wrong input data for the calculation of the Nernst voltage.

Another problem is the fluctuating gas composition coming from a biomass gasifier. These fluctuations complicate an exact determination of the gas composition at the sensor inlet since the corresponding voltage measurement of the sensor occurs time-displaced. Therefore it is difficult to address the correct Nernst voltage to the measured OCV.

Measuring other tar species besides naphthalene, toluene and xylene

The experimental development of the measuring principle in this work is based on tests of naphthalene, toluene and xylene. However, the real wood gas will contain various other tar species as shown in Table 4.3. It can be assumed that not all of them are as critical as naphthalene. Frank [38] for example shows that the conversion of phenol is already complete at $650\,^\circ$C. Therefore, complete conversion without inhibiting the conversion of other hydrocarbons can be expected at $900\,^\circ$C. Nevertheless, tar species with multiple aromatic rings may exhibit a similar conversion behaviour as naphthalene. If this is the case it needs to be investigated to which extend the conversion of methane and other tar species will be inhibited. Most important is to examine if other tar species influence the methane conversion rate as well in order to determine the correct correlation for CR_{CH_4}.

Transient response of tar conversion

As described in Section 6.7 the voltage signal of cell:1 does not immediately appear upon tar addition in the case of naphthalene. This has to be considered for the fluctuating real wood gas composition. If the fluctuation of tar species behaving like naphthalene is low, the transient response may be acceptable. Further tests are necessary to investigate whether using a mean value over a certain time interval is acceptable in order to consider the transient response.

Amplify measuring signal

Eventually the voltage difference $\Delta V_{cell:1\mapsto 2,naph}$ between cell:1 and cell:2 is one main measuring signal to detect part of the tar load. To achieve a better measurability a higher range of the measuring signal may be favorable. The voltage difference $\Delta V_{cell:1\mapsto 2,naph}$ can be increased by increasing the volume flow $\dot{V}_{cell}$. This generally lowers the methane conversion rate as can be seen in Figure 7.7 and decreases $V_{cell:1}$. As long as the reformer is capable to convert all hydrocarbons the $V_{cell:2}$ stays constant. However, the volume flow must not be too high because the conversion of other tar species such as toluene/xylene on cell:1 may be reduced as well. This would cause a lower voltage difference $\Delta V_{cell:1,tol+xyl}$ between $V_{cell:1}$ and the corresponding Nernst voltage (compare with step 3a or 3b of Figure 7.13).

Chapter 8

Summary and outlook

This work investigates the development of a measuring principle for the detection of tar in wood gas from biomass gasification based on a $Ni\text{-}GDC/YSZ/LSM$ solid oxide fuel cell. Wood gas is simulated with bottled gas and additions of naphthalene, toluene and xylene in order to achieve a clean synthesis gas composition without the usual contaminants such as particle, alkali metals, chlorine or sulphur compounds. The conversion of hydrocarbons on the SOFC anode based on steam reforming and shift reaction leads to an increased cell potential. The increase of the cell potential is determined by comparing the open circuit voltage of tar loaded synthesis gas with that of tar free synthesis gas. A linear correlation between the tar concentration and the increase of the OCV in diluted hydrogen as a first result is demonstrated by experiments.

This correlation is something more complex in the case of synthesis gas with considerable amounts of methane and in the presence of other hydrocarbons respectively. Due to the different reactivities of the hydrocarbons a competing situation concerning the conversion exists. In particular naphthalene inhibits complete conversion of methane and other tar species such as toluene and xylene. Furthermore, the OCV is directly influenced by the conversion rate of each hydrocarbon. Due to the inhibition the OCV may decrease upon addition of naphthalene unlike in the case of diluted hydrogen. In fact the change of OCV caused by tar species is based on two main contributing parts. On the one hand, more reactive hydrocarbons are converted to a high degree and thus increase the OCV. On the other hand, the less reactive hydrocarbons such as methane are not converted as much when compared to the tar free gas composition which results in a decrease of the OCV. These two contributions can be added up and attributed to the total tar concentration.

In this work the measuring principle is tested with naphthalene, toluene and xylene. Eventually, the total concentration of tar as well as a differentiation between naphthalene and toluene/xylene can be obtained. Nevertheless, typical wood gas contains a large variety of tar species which would require an extensive testing procedure in order to determine their reactivities and their contributions to the change of OCV respectively. This is a reason why the measurement of the total concentration rather than the individual concentration of each tar species is possible. On the contrary the aim is to enable only a differentiation between tertiary tar such as naphthalene and

secondary such as toluene/xylene because of their specific problems in downstream processes (e.g. condensation of high molecular tar). Therefore, further tests with critical tar species depending on their occurrence are necessary. However, as shown in this work for an allothermal steam gasifier with a bubbling fluidised bed three tar species (phenol, naphthalene and cresols) account for more than $\frac{2}{3}$ of the total tar species. The rest of the tar species emerges in low concentrations and may not contribute severely to the change of OCV. Therefore the measuring principle could be specifically adapted to a certain gasifier type.

Apart from more intensive testing of tar, longterm testing will be necessary as well to identify potential degradation. Degradation may not be a problem as long as only a drop of the OCV is observed. If the conversion of hydrocarbons still follows the same behaviour as at the beginning the sensor could be calibrated every so often by adding an offset value to balance the drop of OCV.

This measuring principle offers an interesting opportunity to measure tar in wood gas from biomass gasification continuously and gives information about the total tar concentration as well as on the rough tar composition. The main advantage compared to state-of-the-art measuring principles is the ability of fast and continuous tar measurement. Furthermore, the incomplex sensor does not require specifically trained staff. Therefore, further research still continuing so as to pack this measuring principle into a suitable sensor design which enables tests on a real gasifier.

Bibliography

[1] Bestimmung des Cemischen Sauerstoffbedarfs (CSB) im Bereich über 15 mg/l. DIN 38409-H 41, 1980.

[2] Wasserbeschaffenheit - Bestimmung des Kohlenwasserstoff-Index. ÖNORM EN ISO 9377-2:2000, 2001.

[3] Biomass Gasification - Tar and Particles in Product Gases - Sampling and Analysis. CEN/BT/TF/ 143, 2004.

[4] Erdgas - Beziehung zwischen Wassergehalt und Taupunkt. ÖNORM EN ISO 18453:2004, January 2006.

[5] Natural gas - Vocabulary. ÖNORM EN ISO 14532:2001 including Corrigendum 1:2002, June 2006.

[6] Flame ionization detector. http://chemwiki.ucdavis.edu, August 2011.

[7] Producer gas. http://en.wikipedia.org, August 2011.

[8] Quadrupole mass spectrometer. http://www.uni-muenster.de, July 2011.

[9] Sensor-Vorrichtung für die Feststellung von toxischem Gas, DE 35 07 385 A1 (patent), 1985.

[10] ABB. Datenblatt: Kontinuierliche Gasanalysatoren, 2010.

[11] ADOS. Kohlenswasserstoff-Analysator, KM 2000 CnHm EM.

[12] ATKINS, P. W., AND DE PAULA, J. *Physikalische Chemie.* Wiley-VCH, 2006.

[13] AWEL GEWAESSERSCHTUZLABOR. Kohlenwasserstoff-Index (KW-Index).

[14] BACHEMA AG. KW-Analytik: Bestimmung der Kohlenwasserstoffe mit Gaschromatographie KW-Index.

[15] BARBIR, F. *PEM Fuel Cells: Theory and Practice.* Elsevier Academic Press, 2005.

[16] BARTEC BENKE. HYGROPHIL HCDT - Messsystem zur Bestimmung des Kohlenwasserstoff- und des Wassertaupunktes in Erdgas.

[17] BAUMHAKL, C. Untersuchungen zur Online-Analyse von Teer aus der Biomassevergasung auf dem Prinzip der Fluoreszenzspektroskopie. Master's thesis, Graz University of Technology, 2009.

[18] BAUMHAKL, C., AND KARELLAS, S. Tar analysis from biomass gasification by means of online fluorescence spectroscopy. *Optics and Lasers in Engineering 49*, 7 (2011), 885 – 891.

[19] BENTON, A. Determination of hydrocarbon dew point in natural gas. In *American School of Gas Measurement Technology* (2007).

[20] BERNATH ATOMIC. Operating manual Modell 3005, 1992.

[21] BIBER, M. *Messmethoden zur Untersuchung der Kohlenstoffablagerung an nickelhaltigen SOFC-Anoden beim Betrieb mit Methan.* PhD thesis, TU Munich, 2010.

[22] BRAGE, C., YU, Q., CHEN, G., AND SJÖSTRÖM, K. Use of amino phase adsorbent for biomass tar sampling and separation. *Fuel 76*, 2 (1997), 137 – 142.

[23] BRAGE, C., YU, Q., CHEN, G., AND SJÖSTRÖM, K. Tar evolution profiles obtained from gasification of biomass and coal. *Biomass and Bioenergy 18*, 1 (2000), 87 – 91.

[24] BROWN, A., MILTON, M., VARGHA, G., MOUNCE, R., COWPER, C., STOKES, A., BENTON, A., BANNISTER, M., RIDGE, A., LANDER, D., AND LAUGHTON, A. Comparison of methods for the measurement of hydrocarbon dew point of natural gas. Tech. rep., National Physical Laboratory, Hampton Road, Teddington, Middlesex, United Kingdom, May 2007.

[25] CHIARAMONTI, D., OASMAA, A., AND SOLANTAUSTA, Y. Power generation using fast pyrolysis liquids from biomass. *Renewable and Sustainable Energy Reviews 11*, 6 (2007), 1056 – 1086.

[26] CORMA, A., AND ORTEGA, F. Influence of adsorption parameters on catalytic cracking and catalyst decay. *Journal of Catalysis 233*, 2 (2005), 257 – 265.

[27] CORNILS, B., HERRMANN, W. A., SCHLÖGL, R., AND WONG, C.-H., Eds. *Catalysis from A to Z.* Wiley, 2000.

[28] DEPNER, H., AND JESS, A. Kinetics of nickel-catalyzed purification of tarry fuel gases from gasification and pyrolysis of solid fuels. *Fuel 78*, 12 (1999), 1369 – 1377.

[29] DRÄGER. Dräger-Röhrchen - das Labor hinter Glas, 2010.

[30] DUFOUR, A., GIRODS, P., MASSON, E., NORMAND, S., ROGAUME, Y., AND ZOULALIAN, A. Comparison of two methods of measuring wood pyrolysis tar. *Journal of Chromatography A 1164*, 1-2 (2007), 240 – 247.

[31] DUTTA, A., NISHIGUCHI, H., TAKITA, Y., AND ISHIHARA, T. Amperometric hydrocarbon sensor using $La(Sr)Ga(Fe)O_3$ solid electrolyte for monitoring in exhaust gas. *Sensors and Actuators B: Chemical 108*, 1-2 (2005), 368 – 373. Proceedings of the Tenth International Meeting on Chemical Sensors.

[32] EFFENBERGER, H. *Dampferzeugung.* Springer, 2000.

[33] EG&G TECHNICAL SERVICES, I. *Fuel Cell Handbook*, seventh ed. U.S. Department of Energy Office of Fossil Energy National Energy Technology Laboratory, 2004.

[34] ELUMALAI, P., PLASHNITSA, V. V., FUJIO, Y., AND MIURA, N. Highly sensitive and selective stabilized zirconia-based mixed-potential-type propene sensor using NiO/Au composite sensing-electrode. *Sensors and Actuators B: Chemical 144*, 1 (2010), 215 – 219.

[35] FAUTEUX-LEFEBVRE, C., ABATZOGLOU, N., BLANCHARD, J., AND GITZHOFER, F. Steam reforming of liquid hydrocarbons over a nickel-alumina spinel catalyst. *Journal of Power Sources 195*, 10 (2010), 3275 – 3283.

[36] FINNERTY, C. M., AND ORMEROD, R. M. Internal reforming over nickel/zirconia anodes in SOFCs operating on methane: influence of anode formulation, pretreatment and operating conditions. *Journal of Power Sources 86*, 1-2 (2000), 390 – 394.

[37] FITZ, A., JUCHEM, B., AND SPÖRL, D. CSB - Bestimmung, April 1998.

[38] FRANK, N. *Umsetzung von Kohlenwasserstoffen in SOFCs*. PhD thesis, TU Munich, 2009.

[39] FRECH, T. Abwasserüberwachung als vorbeugender Gewässerschutz. *Chemie Ingenieur Technik 60* (1988), 359–364.

[40] FUELCON. TrueDATA-Load, Modular Electronic Load, Operation Manual.

[41] GORTE, R. J., KIM, H., AND VOHS, J. M. Novel SOFC anodes for the direct electrochemical oxidation of hydrocarbon. *Journal of Power Sources 106*, 1-2 (2002), 10 – 15.

[42] GORTE, R. J., AND VOHS, J. M. Novel SOFC anodes for the direct electrochemical oxidation of hydrocarbons. *Journal of Catalysis 216*, 1-2 (2003), 477 – 486.

[43] GOTTFRIED, J. M., VESTERGAARD, E. K., BERA, P., AND CAMPBELL, C. T. Heat of adsorption of naphthalene on Pt(111) measured by adsorption calorimetry. *The Journal of Physical Chemistry B 110*, 35 (2006), 17539–17545.

[44] GOULA, G., KIOUSIS, V., NALBANDIAN, L., AND YENTEKAKIS, I. Catalytic and electrocatalytic behavior of Ni-based cermet anodes under internal dry reforming of $CH_4 + CO_2$ mixtures in SOFCs. *Solid State Ionics 177*, 19-25 (2006), 2119 – 2123. Solid State Ionics 15: Proceedings of the 15th International Conference on Solid State Ionics, Part I.

[45] GOULD, B. D., TADD, A. R., AND SCHWANK, J. W. Nickel-catalyzed autothermal reforming of jet fuel surrogates: n-dodecane, tetralin, and their mixture. *Journal of Power Sources 164*, 1 (2007), 344 – 350.

[46] GUPTA, K., REHMAN, A., AND SARVIYA, R. Bio-fuels for the gas turbine: A review. *Renewable and Sustainable Energy Reviews 14*, 9 (2010), 2946 – 2955.

[47] HAGEN, J. *Technische Katalyse.* VCH, 1996.

[48] HAUTH, M., FRANK, N., AND KARL, J. Influence of tars on the maximum hydrogen utilization in SOFCs with biogeneous gases. In *European Fuel Cell Forum 2009* (2009).

[49] HAUTH, M., KIENBERGER, T., AND KARL, J. Transient operation effects of SOFCs driven with tar loaded synthesis gas. In *219th ECS meeting: SOFC-XII Symposium* (2011).

[50] HAUTH, M., LERCH, W., KÖNIG, K., AND KARL, J. Impact of naphthalene on the performance of SOFCs during operation with synthetic wood gas. *Journal of Power Sources 196*, 17 (2011), 7144 – 7151. Proceedings of 2010 European Solid Oxide Fuel Cell Forum.

[51] HIEBLER, H. Ceramic cell housing. Personal drawing at the Institue of Thermal Engineering, April 2011.

[52] HUEMER, H., AND WALLEK, T. Chemische Thermodynamik I. Study-script, 2009.

[53] IHM, H., AJO, H. M., GOTTFRIED, J. M., BERA, P., AND CAMPBELL, C. T. Calorimetric measurement of the heat of adsorption of benzene on Pt(111). *The Journal of Physical Chemistry B 108*, 38 (2004), 14627–14633.

[54] JESS, A. Catalytic upgrading of tarry fuel gases: A kinetic study with model components. *Chemical Engineering and Processing 35*, 6 (1996), 487 – 494.

[55] JESS, A. Mechanisms and kinetics of thermal reactions of aromatic hydrocarbons from pyrolysis of solid fuels. *Fuel 75*, 12 (1996), 1441 – 1448.

[56] KARL, J. *Dezentrale Energiesysteme*, second ed. Oldenbourg Verlag München Wien, 2006.

[57] KEIL, F. *Diffusion und Chemische Reaktionen in der Gas/Feststoff-Katalyse.* Springer, 1999.

[58] KIENBERGER, T. *Methanierung biogener Synthesegase mit Hinblick auf die direkte Umsetzung von höheren Kohlenwasserstoffen.* PhD thesis, Graz Universtity of Technology, 2010.

[59] KIENBERGER, T., AND KARL, J. Tests on methanation with tar and sulphur loaded syngas. In *1st International Conference on Polygeneration Strategies* (2009).

[60] KIM, T., LIU, G., BOARO, M., LEE, S.-I., VOHS, J., GORTE, R., AL-MADHI, O., AND DABBOUSI, B. A study of carbon formation and prevention in hydrocarbon-fueled SOFC. *Journal of Power Sources 155*, 2 (2006), 231 – 238.
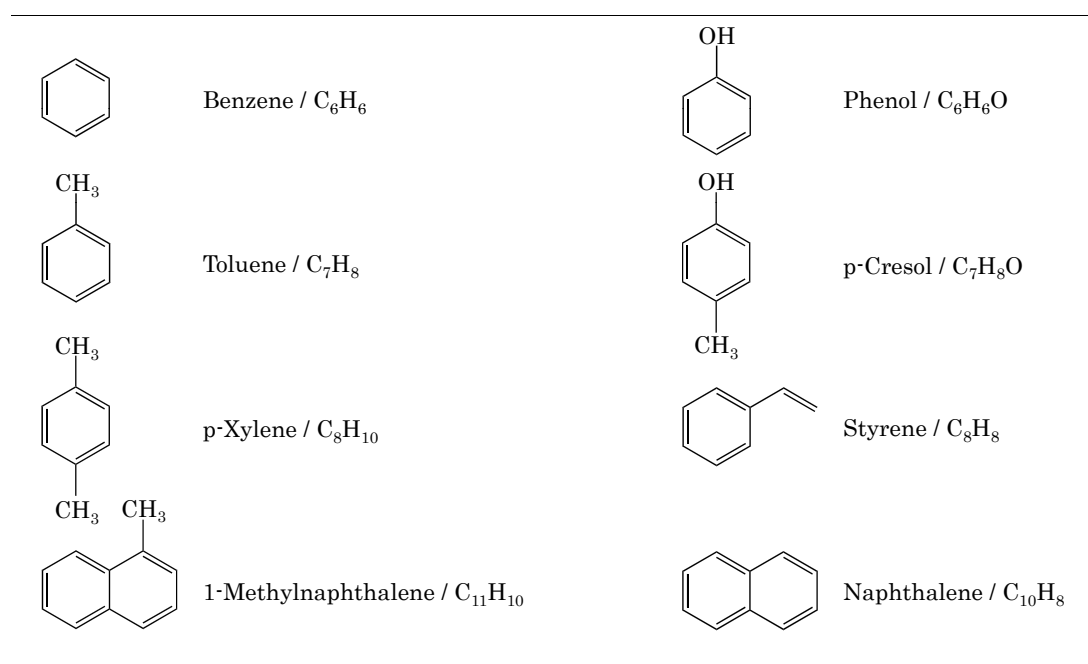
[61] KLEIN, J.-M., BULTEL, Y., GEORGES, S., AND PONS, M. Modeling of a SOFC fuelled by methane: From direct internal reforming to gradual internal reforming. *Chemical Engineering Science 62*, 6 (2007), 1636 – 1649.

[62] KÖNIG, K. Untersuchung der Fuel Utilization einer Solid Oxide Fuel Cell mit teerbeladenen Brenngasen. Master's thesis, Graz University of Technology, 2010.

[63] KOH, J.-H., YOO, Y.-S., PARK, J.-W., AND LIM, H. C. Carbon deposition and cell performance of Ni-YSZ anode support SOFC with methane fuel. *Solid State Ionics 149*, 3-4 (2002), 157 – 166.

[64] LABEAUX. Bestimmung des Kohlenwasserstoff-Index in Wasser (Extraktion mit Hexan) mittels GC/FID.

[65] LAOSIRIPOJANA, N., AND ASSABUMRUNGRAT, S. Catalytic steam reforming of methane, methanol, and ethanol over Ni/YSZ: The possible use of these fuels in internal reforming SOFC. *Journal of Power Sources 163*, 2 (2007), 943 – 951.

[66] LERCH, W. Betriebsverhalten einer SOFC mit teerbeladenen Brenngasen. Master's thesis, Graz University of Technology, 2009.

[67] MCINTOSH, S., AND GORTE, R. Direct hydrocarbon solid oxide fuel cells. *Chemical Reviews 104*, 10 (2004), 4845–4865.

[68] MERMELSTEIN, J., BRANDON, N., AND MILLAN, M. Experimental study assessment of mitigation of carbon formation on Ni/YSZ and Ni/CGO SOFC anodes operating on biomass gasification syngas and tars. In *European Fuel Cell Forum 2009* (2009).

[69] MERMELSTEIN, J., MILLAN, M., AND BRANDON, N. The impact of carbon formation on Ni-YSZ anodes from biomass gasification model tars operating in dry conditions. *Chemical Engineering Science 64* (2009), 492 – 500.

[70] MERMELSTEIN, J., MILLAN, M., AND BRANDON, N. The impact of steam and current density on carbon formation from biomass gasification tar on Ni/YSZ, and Ni/CGO solid oxide fuel cell anodes. *Journal of Power Sources 195*, 6 (2010), 1657 – 1666.

[71] MILNE, T. A., AND EVANS, R. J. Biomass gasifier "tars": Their nature, formation and conversion. Tech. rep., National Renewable Energy Laboratory, 1998.

[72] MORTIMER, C. E., AND MÜLLER, U. *Chemie - Das Basiswissen der Chemie.* Georg Thieme Verlag, 2003.

[73] NATIONAL INSTITUTE OF STANDARDS AND TECHNOLOGY. http://www.nist.gov, December 2008.

[74] ODERT, P. Reformierung von Kohlenwasserstoffen. Master's thesis, Graz University of Technology, 2005.

145

[75] OUWELTJES, J. P. Degradation mechanisms - influence of hydrocarbons. In *BioCellus Summer School* (2007).

[76] PARK, S., CRACIUN, R., VOHS, J. M., AND GORTE, R. J. Direct oxidation of hydrocarbons in a solid oxide fuel cell: I. methane oxidation. *Journal of The Electrochemical Society 146*, 10 (1999), 3603–3605.

[77] PARK, S., VOHS, J. M., AND GORTE, R. J. Direct oxidation of hydrocarbons in a solid-oxide fuel cell. *Nature 404*, 6775 (2000), 265–267.

[78] PHUPHUAKRAT, T., NAMIOKA, T., AND YOSHIKAWA, K. Tar removal from biomass pyrolysis gas in two-step function of decomposition and adsorption. *Applied Energy 87*, 7 (2010), 2203 – 2211.

[79] RABOU, L. P. L. M., GRIFT, J. M., CONRADIE, R. E., AND FRANSEN, S. Tar in biomass producer gas, the energy research centre of the netherlands (ECN) experience: An enduring challenge. *Energy and Fuels 23*, 12 (2009), 6189–6198.

[80] RAU, H., AND RAU, J. *Chemische Gleichgewichtsthermodynamik.* Vieweg, 1995.

[81] ROSTRUP-NIELSEN, J. R. *Catalysis.* Springer Berlin, 1983, ch. Catalytic Steam Reforming.

[82] SAUNDERS, G. J., AND KENDALL, K. Reactions of hydrocarbons in small tubular SOFCs. *Journal of Power Sources 106*, 1-2 (2002), 258 – 263.

[83] SCHWEIGER, A. *Reinigung von heißen Produktgasen aus Biomassevergasern für den Einsatz in oxidkeramischen Brennstoffzellen.* PhD thesis, Graz University of Technology, 2008.

[84] SCOTT, H. G. Phase relationships in the zirconia-yttria system. *Journal of Materials Science 10* (1975), 1527–1535.

[85] SEYDEL, J. *Nanokristallines Zirkondioxid für Hochtemperatur-Brennstoffzellen.* PhD thesis, TU Darmstadt, 2003.

[86] SHEKHAWAT, D., BERRY, D. A., HAYNES, D. J., AND SPIVEY, J. J. Fuel constituent effects on fuel reforming properties for fuel cell applications. *Fuel 88*, 5 (2009), 817 – 825.

[87] SICK MAIHAK. Liste der Stoffe zur Berechnung der Kalibriergrößen.

[88] SINGHAL, S. C., AND KENDALL, K. *High Temperature Solid Oxide Fuel Cells - Fundamentals, Design and Applications.* Elsevier Ltd., 2003.

[89] SUN, R., ZOBEL, N., NEUBAUER, Y., CHAVEZ, C. C., AND BEHRENDT, F. Analysis of gas-phase polycyclic aromatic hydrocarbon mixtures by laser-induced fluorescence. *Optics and Lasers in Engineering 48*, 12 (2010), 1231 – 1237.

[90] TU, H., AND STIMMING, U. Advances, aging mechanisms and lifetime in solid-oxide fuel cells. *Journal of Power Sources 127*, 1-2 (2004), 284–293.
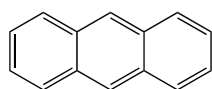
[91] WAHL, S. Auslegung einer Gasregelstrecke zur Konditionierung synthetischer Holzgase. Master's thesis, Graz University of Technology, 2009.

[92] XU, J., AND FROMENT, G. Methane steam reforming, methanisation and water-gas shift: I. intrinsinc kinetics. *AIChE Journal 35* (1989), 88–96.

[93] YENTEKAKIS, I. V. Open- and closed-circuit study of an intermediate temperature SOFC directly fueled with simulated biogas mixtures. *Journal of Power Sources 160*, 1 (2006), 422 – 425.
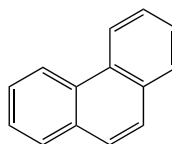
147

Appendix A

Molecule structures of hydrocarbons

Benzene / C_6H_6

Phenol / C_6H_6O

Toluene / C_7H_8

p-Cresol / C_7H_8O

p-Xylene / C_8H_{10}

Styrene / C_8H_8

1-Methylnaphthalene / $C_{11}H_{10}$

Naphthalene / $C_{10}H_8$

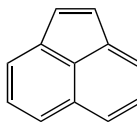Anthracene / $C_{14}H_{10}$

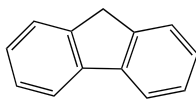Phenanthrene / $C_{14}H_{10}$
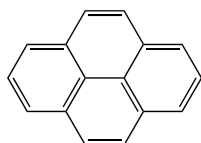
Pyrene / $C_{16}H_{10}$
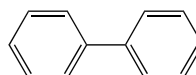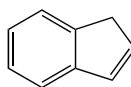
Biphenyl / $C_{12}H_{10}$
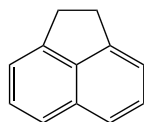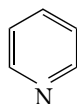
Acenaphthene / $C_{12}H_{10}$

Acenaphthylene / $C_{12}H_8$

Fluorene / $C_{13}H_{10}$

Indene / C_9H_8

Pyridine / C_5H_5N

Furan / C_4H_4O

Thiophene / C_4H_4S